Gaining Insight into the Design of Oxidation Catalysts by Comparing the Rate and Equilibrium Constants That Define the Technical Performance of a Suite of TAML Activators Including Design Related Studies for Environmental Performance.

Dissertation by
Matthew A. DeNardo

In Partial Fulfillment of the Requirements for the Degree of
Doctor of Philosophy

Terrence J. Collins,
Thesis Advisor

Carnegie Mellon University
Pittsburgh PA

Submitted March 26, 2016

Acknowledgements

I am deeply indebted to a great many people who have contributed to my development including my parents who have been tremendously supportive and deserve a massive amount of respect. I have not always shown this to them or told them how much I love them. I would also like to thank my entire family including Carmine DeNardo who came to America by ship in search of a better life.

Similarly, but to a significantly lesser extent I am indebted to the many chemists who have developed the art over the centuries.

Next I would like to thank the many chemists who personally contributed to my development throughout the years including, but without limitation to, the following: Drs. Thomas Vargo, Thomas Painter, and Peter Bell who contributed heavily to my early understanding of chemistry. Dr. George Bandik who supported me throughout my undergraduate years and helped me to secure an undergraduate research position with Dr. Dennis Curran to whom I attribute nearly all of my knowledge of organic chemistry. Dr. Eveline Kumli who taught me many of the synthetic techniques I currently rely upon with the patience of a true saint as well as Drs. David Guthrie, Fa Zhang, Qianli Chu, Jared Moretti, and Jesse Sabatini who further enriched my education in the Curran Group.

In addition to these, other chemists have also contributed heavily to my development. These include my advisor Dr. Terrence Collins without whom this work would not have been possible and with I have had many great discussions of coordination chemistry from which I have learned a tremendous deal. Dr. Collins has also spent much time attempting to teach me to write with greater clarity, a massively useful general skill. I am thankful for the similar efforts of Dr. Alexander Ryabov to whom I attribute nearly all of my current understanding of chemical kinetics and who initiated the early studies with mathematicians Dr. Maria Emelianenko and Diego Torrejon that comprise the bulk of thesis. These three deserve most of the credit for the development of the kinetic tool without which much of this work would not have been possible. I am also indebted to all Collins Group members past and present the combined efforts of which led to TAML catalysts, the subject of this work.

Thanks are also owed to the many friends that have supported me throughout the years and continue to. This is not exclusive of anyone named explicitly. It's done. Now buy me a beer or make me a curry. No, you don't have to call me Dr. though I'd really like it if you did in jest before admonishing an act of mine. It will greatly help your cause.

I would also like to thank Mrs. Rea Freeland and the Department of Chemistry at Carnegie Mellon University as well as CMU in general. This is a very special place. I used to visit the campus when I was a Pitt student and never thought I'd get the chance to go to school here. I still can't believe I was allowed to.

Finally, I'd like to thank Dr. Stefan Bernhard, Dr. Tara Meyer, Dr. Krysztof Matyjaszewski, and Dr. Kevin Noonan for graciously donating their time as members of the committee that evaluated some or all of the requirements for this degree including this thesis. I hope they have found it well-spent.

Table of Contents

Index of Figures

Index of Tables

Abstract

Iron tetraamido macrocylic ligand complexes (TAMLs) have been found to catalyze the oxidation of micropollutants by H_2O_2 under mild conditions. TAML development has long been focused on the design of environmentally benign catalysts. Concerns about the potential toxicity of catalysts containing phenylenediamine nitro groups including the most reactive TAML catalyst to date known as $Fe(NO_2)_2D^{*-}$ (**1**) led to the design and synthesis of one containing phenylenediamine nitrile groups, $Fe(CN)_2D^{*-}$ (**2**) for comparative studies. The main features of TAML catalysis of peroxide oxidations are rationalized by the two-step mechanism: $Fe^{III} + H_2O_2 \rightarrow$ Active catalyst (Ac) (k_I), Ac + Substrate (S) $\rightarrow Fe^{III}$ + Product (k_{II}). Studies of **2** catalyzed bleaching of the azo dye Orange II by H_2O_2 at pH 9 in 25 °C, 0.01 M phosphate buffer indicate that under these conditions, the **2** k_I and k_{II} are 18,000 ± 3000 and 240,000 ± 40,000 $M^{-1}s^{-1}$, respectively. These are comparable to 16,000 ± 2000 and 1,000,000 ± 100,000 $M^{-1}s^{-1}$ the literature **1** k_I and k_{II} values under identical conditions, respectively. At pH 7, a desirable pH for water treatment, the performances of **1** and **2** are also similar with k_I values of 1850 ± 90 and 1,900 ± 100 $M^{-1}s^{-1}$ and k_{II} values of 260,000 ± 40,000 and 520,000 ± 70,000 $M^{-1}s^{-1}$, respectively. Since k_I is usually rate determining, **1** and **2** can be expected to perform most pH 7 and 9 oxidations with similar rates.

In water, TAML catalysts are thought to possess two axial water molecules. The pK_a of at least one of these water molecules can be determined by spectrophotometric titration. Previous studies have observed an inverse relationship between pK_{a1} and k_I at pH 7 across a series of TAMLs. However, the **2** pK_{a1} is found to be 8.8±0.1, 0.4 units greater than the known **1** pK_{a1} of 8.43±0.15, which is the lowest observed to date. This

difference is not reflected in the relative pH 7 and 9 k_I values. The only TAML pK_{a2} value has been observed for **1**. This remains so as attempts to determine the **2** pK_{a2} reveal the **2** Rc to be unstable above pH 10. This instability is attributed to hydrolysis of at least one nitrile group. Correlations of k_I and k_{II} with the first and second redox potentials and Hammett parameters of **1**, **2**, $Fe(Cl)_4D^{*-}$ containing four phenylenediamine chlorines, and FeD^{*-} containing no phenylenediamine electron withdrawing groups reveal concave downward k_I dependences and linear k_{II} dependences. The former indicates that the k_I process of this set of TAMLs may be the sum of at least two steps rather than one as it is currently modeled. Analysis of TAML ecotoxicity by the zebrafish model for detection of developmental disruption reveals all tested activators to be relatively benign with greater toxicity associated with possession of phenylenediamine electron withdrawing groups following the order Cl > CN > NO_2. Due to the observed high pH instability and increased toxicity of **2** over that of **1**, further pursuit of nitrile containing activators is not recommended. The pH 7 reactivity of $FeDF_2^-$, an activator similar to FeD^{*-} containing fluorine atoms appended to the methylene carbon of a malonamide residue is assessed. The distinct k_I values of 250 ± 60 and 900 ± 100 $M^{-1}s^{-1}$ and matching k_{II} values of 840 ± 30 and 900 ± 100 $M^{-1}s^{-1}$ for the latter and former, respectively, indicate that the Ac of both may have significant radical cation character.

Since useful catalysis relies upon minimization of catalyst inactivation processes, TAML development has also long been focused on studies of catalyst inactivation mechanisms of such processes. Detailed studies of TAML Ac inactivation (k_i) which apply a newly developed kinetic tool to catalysis of the oxidation of Orange II by H_2O_2 in pH 7, 25 °C, 0.01 M phosphate buffer by 15 TAML activators at water treatment relevant

catalyst concentrations yield k_I, k_{II}, and k_i values for all studied activators. Linear free energy relationships (LFERs) show k_i to increase proportionally (slope~1) with k_I and k_{II} indicating that all three processes derive from the same electronic origin, likely Lewis acidity at iron. These and a k_I/k_{II} LFER show k_I to be sensitive to the steric environment of the iron center indicating that diffusion of H_2O_2 to the iron atom plays a role in the k_I pathway and may be contribute to the aforementioned concave downward Hammett dependence. The 15 catalyst data set from which the k_i/k_{II} LFER is constructed is structurally diverse indicating that the iron atom, N—Fe bond, or amides themselves are the primary site of the observed catalyst inactivation processes under these conditions. Detailed studies of the dependence of k_i on H_2O_2 and OH^- for 9 of the 15 catalysts reveal two major inactivation pathways. One involves nucleophilic attack of H_2O_2 via a general base mechanism. The remaining inactivation steps likely follow a Dakin oxidation or hydrolysis pathway with the amido nitrogen or C—C bond serving as a leaving group. The other pathway is likely general base catalyzed amide hydrolysis with the amido nitrogen or C—C bond serving as a leaving group. Finally, a k_i/k_{II} LFER for the reactivity at one catalyst over the pH range of 7–12.7 reveals a linear relationship having a slope of ~1 indicating that similar mechanisms of inactivation may operate over the majority of the studied pH range. However, outliers are observed at pH 10–11.5. Here, the k_i values are ca one order of magnitude lower than expected from the trend. This enhanced stability may derive from a unique solvation of the Ac form which predominates over the pH range 10–11.5. The result may indicate that the OH^- which participates as a general base in the pH 7, H_2O_2 dependent inactivation pathway resides within the Ac solvation sphere.

Chapter 1

Introduction and Thesis Statement

Introduction

From the generation of glass by early chemical craftsmen through 'Anthropocene era' research at the dawn of the 20th century 'Chemical Age' to the present, chemists have strived to produce substances and materials having novel and adventitious properties that enable societal progress.[1,2] Products and processes displaying enhanced performance, greater durability, and more favorable economic properties than their naturally occurring predecessors have been and are zealously sought and realized.[2] These accomplishments continue to enrich the human experience. Examples include aniline dyes that have been optimized for improved aesthetics and superior durability, synthetic aspirin and paracetamol that offer relief from pain, and novel materials having heretofore unseen properties such as the pyroxylin products that have ushered in culturally transformative advances in photography.[2] Other synthetic products of chemistry include pharmaceuticals, personal care products, and pesticides all of which have been optimized for maximum efficacy and resistance to oxidative decomposition. Unfortunately, these often become aqueous micropollutants (MPs). For example, pharmaceuticals are excreted in both parent and metabolized forms into wastewater and also are disposed of by flushing in toilets leading to wastewater contamination.[3] Some MPs are very difficult to remove and pose challenges to the system of water management on which we depend. This thesis concerns the development of a technology, iron tetraamido macrocyclic ligand catalysts (TAMLs) intended to remove MPs from water under ambient conditions. Consequently, we begin with a discussion of the wastewater water treatment technologies currently in wide use with a focus on their MP removal efficiencies, the impact this has

on surface and source waters, and the drinking water treatment technologies currently employed as well as their MP removal efficiencies.

Wastewater Treatment

Raw wastewater flows to municipal water treatment plants. Here it undergoes treatment which consists of primary, secondary, and less commonly employed tertiary processes.[4] Primary processes include coagulation, flocculation, sedimentation, and filtration procedures designed to remove insoluble materials such as suspended solids.[4] Coagulants such as aluminum sulfate, polyaluminum chloride (PACl), ferric salts, and other cationic chemicals, are added to water. These form larger particles with negatively charged dirt and dissolved organic carbon (DOC) and precipitate as metal hydroxides or carbonates that are removed by filtration.[5,6] Softening agents such as lime and soda ash may be added to cause $CaCO_3$ and $MgOH_2$ to encourage precipitation.[7]

Removal of micropollutants during primary processes occurs through adsorption to suspended soil solids and precipitates containing DOC.[4,5] Some negatively charged micropollutants also undergo electrical aggregation with coagulant cations.[5] These contaminated solids are then removed by filtration during which MPs can also adsorb to sand filters. During primary treatment MPs can be transformed by sunlight photodegradation and hydrolysis or desorb resulting in rerelease and temporary negative removal efficiencies.[4,5] A weak correlation between the percent removals of compounds not in anionic form at the pH of the influent tested and the logarithm of the octanol-water partition coefficient (K_{OW}) has been observed.[7] While these processes remove some of the initial concentration of hydrophobic compounds, especially those having log K_{OW} >

5, they do not efficiently remediate most micropollutants (<50%), especially those that are more polar.[4-7] Consequently, flocculation and sand filtration alone are not likely to remove most pharmaceutical residues.[3] For example, one study found flocculation with $FeCl_3$ did not significantly alter raw water concentrations of the pharmaceuticals bezafibrate, carbamazepine, clofibric acid and diclofenac in either laboratory tests or two waterworks.[3] In addition, neither sorption to nor biodegradation of the polar pharmaceuticals benzafibrate, clofibric acid, diclofenac, and carbamazepine by sand or gravel samples occurred to any measurable extent.[3] While the test conditions used may not represent all natural conditions, the researchers concluded that neither process will have a large effect on concentrations of these pharmaceuticals.[3] Another bench scale study found removals of less than 15% for 34 of 36 compounds studied though the better removals of 31% of DDT and 70% of benzo[*a*]pyrene were observed .[7] The higher removal efficiencies of the latter have been attributed to their lower polarity (log K_{OW} > 6).[7]

Secondary treatment processes include dispersion, dilution, sorption, partitioning, biotransformation, and abiotic transformation.[4] Chief among these are sorption and biotransformation both of which occur during treatment with activated sludge.[8] As in primary wastewater sludge treatment, MPs such as acetyl salicylic acid, estradiol, ibuprofen, paracetamol and pyrene can be adsorbed and transformed in secondary activated sludge treatment. MP removal can be enhanced by addition of powdered activated carbon (PAC) to the biological treatment tank resulting removal efficiencies of >80% for most micropollutants.[4]

However, some micropollutants resist adsorption and biotransformation. For example, the concentrations of the active pharmaceuticals carbamazepine, crotamiton, diazepam, and diclofenac are not altered by activated sludge treatment.[8] Others, including pharmaceuticals, antibiotics, steroid hormones, plasticizers, detergents, and pesticides, are not completely degraded.[4] For some MPs the extent of transformation varies with sludge retention time such that longer times result in greater degradation. These time frames range from days to weeks.[8] The resultant transformation byproducts are often released as they are more polar than the parent compound. In addition, activated sludge treatment can result in greater concentrations of micropollutants in discharge than in influent.[4] For example, pharmaceuticals that have been bioconjugated for excretion during metabolism within an organism can be deconjugated during treatment with secondary processes to give the initial active compound.[4,9]

Tertiary treatment processes include adsorption to activated carbon (AC). This is performed at the end of the treatment process as natural organic matter and other contaminants can saturate the pores of activated charcoal drastically diminishing the effectiveness of the treatment.[4,10] AC treatments effectively remove non-polar micropollutants ($K_{ow} > 2$) that are able to fit within the pore sizes and shapes of the carbon employed.[4] Consequently, the technology is likely to be poorly suited to the removal of polar micropollutants including transformation products.[4] Passage of treated water through a granular activated carbon (GAC) column during tertiary treatment has been observed to remove 50-90% of micropollutants with the exception of some pharmaceuticals for which removal efficiencies are only ~20%.[4]

Due to the diversity of structures and properties of micropollutants, no one wastewater treatment technique effectively eliminates all micropollutants, and small polar compounds can elude wastewater treatment leading to their discharge to surface and ground waters.[3,4] Wastewater discharge is a major contributor to source water contamination with endocrine disruptors (EDCs), pharmaceuticals and personal care products (PPCPs), disinfection byproduct precursors, and pathogens.[4,7,11]

The Presence of Anthropogenic Chemicals in Environmental Waters

Micropollutants from municipal wastewater treatment effluent join the solvents, additives, lubricants, flame retardants, detergents, pharmaceuticals, hormones, personal-care products, pesticides, nonagricultural biocides, and transformation products prevalent in both remote and urban ground and surface waters from a variety of sources including agricultural and urban runoff, leaching from soils, landfill leaks, and accidental spillage.[3,10] Pharmaceuticals, personal care products, steroid hormones, surfactants, and industrial chemicals have been detected in surface waters at levels greater than their potential no effect concentration (PNEC), the level at which their presence in the environment is estimated to cause no deleterious effects.[4]

A recent survey of US streams found at least one pesticide in nearly every fish and water sample taken.[12] Compounds found include diazinon, carbaryl, chlorpyrifos, malathion, atrazine, simazine, prometon, p,p'-DDT, chlordane, aldrin and dieldrin. In addition to pesticides, other anthropogenic agents. Concentrations of insecticides in excess of those recommended by USEPA, Canadian, or International Joint Commission water-quality guidelines have been found in almost every urban stream assayed. A recent

report indicates that the insect repellant and solvent DEET was found in 100% of source waters.[7] This report also found the pharmaceuticals carbamazepine, dilantin, sulfamethoxazole, and meprobamate in greater than 80% of drinking water source waters. Assessing the extent of the dissemination of anthropogenic chemicals in the environment is very difficult. Our knowledge of which manmade chemicals are present is limited to those for which we choose to look and where we choose to look for them. The environmental concentrations of only a small fraction of the anthropogenic chemicals produced are regularly monitored.[13] The reasons for this are often financial. In some cases, a compound of interest is quantifiable by existing methodology. However efforts to do so are limited by a lack of funding.[13] In others, detection and quantification of a compound in the environment lies outside of existing analytical methodology and the financial means to develop new methodologies and employ them is nonexistent.[13]

Data gaps further complicate efforts to detect anthropogenic chemicals in the environment. Fortunately, the identities of the chemicals produced in the largest volume are known. If more than 4.5 tonnes of a chemical are manufactured or imported in a given year, the TSCA Inventory Update Rule requires that it be reported.[13] Unfortunately, the past and current end uses of these chemicals are often unknown. This obscures efforts to determine which chemicals to look for, as it is difficult to discern between those generated and consumed as intermediates and those distributed in final products and commodities.[4,13] In addition, the constants which describe their physical and chemical properties are often unavailable.[7,13] This complicates determinations of which are capable of accumulating in the environment as well as where they will be found. Furthermore, 530 new chemicals are introduced to the market annually for which little data is available

at all.[14] These include compounds whose structures and properties have been deemed too confidential to be disclosed including replacements for existing agents which have been determined to be environmentally hazardous like polybrominated diphenyl ethers (PBDEs).[13]

In source waters, MPs are attenuated by dilution and sorption to suspended solids and sediments and can be altered by photolysis and aerobic biodegradation.[4] Anthropogenic chemicals undergo abiotic transformations such as reactions with airborne hydroxyl radicals, hydrolysis, oxidation, photooxidation, and direct photolysis.[15] In most cases little is known of the identities of the products formed. As a result assessments of the physical properties that determine the environmental compartments into which they will partition, their detection, and quantification are not possible.[9,16] Biotic processes including microbial transformations in water and soil as well as oxidative degradation and bioconjugation in animals and humans prior to excretion also generate transformation products.[9] These are even more difficult to account for due to geographic variability.[10] Biotransformation products often retain the activity of the parent compound, may be more persistent than it, and are usually more polar than the initial toxicant rendering them more likely to be mobile within water, a distributive medium.

The quantification of transformation products of known structure is often a complex task though progress has been and continues to be made as better analytical techniques are developed and more analytical standards become widely available.[16] Transformation products of known structure have been observed in the environment in greater quantities than their parent compounds.[16] Given these limitations, it is reasonable to conclude that estimates of the extent to which anthropogenic chemicals and their degradates are present

in the environment likely undershoot the true amount.

Though we choose not to monitor their release and environmental levels, the organisms exposed to them do. There is the growing body of literature on the chronic ecotoxicity of anthropogenic chemicals. The bulk of the ecotoxicological data that has been collected concerns acute toxicity to aquatic organisms.[16] Acute toxicity is the disruption of the homeostasis of an organism that results from one or many repeated exposures to a toxicant over a short time period thought to result from narcosis, a perturbation of cell membrane permeability that occurs without ligand-receptor binding, and/or through chemical reactions in which the toxicant participates.[10,14] Chronic toxicity results from repeated exposures to a toxicant over a longer time period and as a result is more difficult to observe.[14] Adverse health effects associated with chronic toxicity can result from slowly developing conditions caused by narcosis or interference with cellular processes.[14] This more subtle form of toxicity includes reactive mechanisms and/or receptor binding.[14]

The widely reported feminizations of male fish in US rivers represent cases of chronic toxicity. While some of the MPs accountable have been identified, the burden of others can be difficult to estimate as environmental exposures often occur to mixtures of compounds. For example, degradates often exist with their parent compounds.[16] This complicates toxicity assessments as agents may have synergistic effects that result in disruption though all components while being within levels of exposure which have been deemed safe in isolation.[10] This has been observed both for compounds acting via a similar mechanistic pathway, such as estrogens, as well as those acting through distinct ones.[10] Controlled laboratory studies involving exposure to only one agent may miss

these as the agent to which the organism is exposed in the lab likely represents less than the full complement to which an organism is exposed in the wild. Nevertheless, the results are informative. One such study followed the effects of fathead minnow exposure to environmentally relevant concentrations of 17α-ethynylestradiol (EE2), the synthetic estrogen employed in birth control pills known to resist complete degradation by municipal water treatment processes.[17] In one test-lake, deviations were significant enough to cause population collapse due to reproductive failure.[17] Environmental incidence of this MP has been linked to exposure from municipal wastewater treatment effluent containing estrogenic compounds.

Drinking Water Treatment

The presence of these agents in treated wastewater is of particular interest to individuals who reside in watersheds where drinking water treatment sources are impacted by municipal waste treatment effluent. In most cases drinking water treatment plants were not designed to treat influent composed of municipal waste effluent. This practice, known as de facto potable water reuse, impacts 82% of the US population, >70% of which is connected to a municipal sewer system.[11] The extent of the municipal waste effluent contribution to the total source water volume varies geographically and seasonally due to fluctuations in source volume with greater contributions from waste treatment being observed during dry periods.[11] For example, when stream flow levels are low, treated effluent comprises >90% of approximately half of south central state streams.[11] Under low flow conditions, municipal waste effluent has been estimated to comprise 100% of drinking water treatment intake at 23 of 80 intakes studied.[11] For

reference, to eliminate chemical hazards the California Department of Health recommends that wastewater treatment plant effluent should comprise <10% of drinking water intake volume.[11]

While de facto water reuse mainly concerns watersheds subject to low flow conditions, combined sewer overflows (CSOs) negatively impact those receiving large amounts of precipitation. More than 700 US cities rely upon a sewage distribution system that combines storm flows and municipal waste, both are released to receiving waters when municipal water treatment plants are overwhelmed during heavy precipitation events.[18] Since CSOs are released without wastewater treatment, they are a significant source of contaminants that are typically well removed (>90%) by sewage treatment including polycyclic aromatic hydrocarbons; organochlorine compounds; drugs including caffeine, ibuprofen and propranolol; sterols and stanols including β-coprostanol, β-sitosterol, and cholesterol; estrogens including 17*β*-estradiol and estriol; androgens including 11-keto testosterone, androstenedione, *cis*-androsterone, dihydrotestosterone, epitestosterone, and testosterone; bacteria; and nutrients. For example, CSOs and can account for 40-90% of annual hormone release to receiving waters in areas where wastewater removal efficiencies of these are >90%.[18] These overflows are a less significant source of contaminants which are not well removed (<90%) such as benzophenone, bisphenol A, estrone, galaxolide, tris(2-butoxyethyl)phosphate, and triclosan.[18] CSOs obviate the sewage treatment / drinking water treatment redundancy in place to help ensure the provision of high quality drinking water.[19] In addition to CSOs, high flow periods during which residence times and efficiencies of filtration are lower lead to higher concentrations of contaminants in treated plant effluent. This results from

diminished removal efficiencies andinfrastructure deficiencies such as leaks also result in release of untreated wastewater, landfill leachate, and agricultural runoff to further compromise source waters.[8,18]

Drinking water treatment relies on adsorptive processes much like those used in municipal waste treatment followed by oxidative treatment. Water is drawn from a ground or surface water source. Dirt and suspended particles are removed by coagulation in which Alum and other cationic chemicals are added to water form larger particles called floc with negatively charged dirt and other particles.[5] The water is then sent to sedimentation tanks where heavy particles are allowed to precipitate. This is then filtered. Like sewage treatment, this process fails to completely remove many MPs including EDCs and PPCPs.[6]

Disinfection is then employed to kill bacteria and microorganisms. Major disinfection processes are oxidative and include chlorination, chloramination, ozonation, and advanced oxidation by UV/H_2O_2.[9] Among these, chlorination is often preferred as it has long been in use and is capable of continuing to disinfect during transportation in pipelines and storage in water towers. This activity is thought to reduce incidences of public disease, but recent work has noted a considerable lack of direct evidence for this conclusion and highlights other methods of ensuring water quality which may not produce disinfection byproducts including the use of multiple barriers of protection such as the wastewater treatment / drinking water treatment redundancy.[19] While chlorination eliminates microbial activity by oxidation of molecules as well as substitution with or addition of chlorine to them, it does not effectively remove MPs nor it is usually intended to.[5-7] During chlorination, the polar MPs that often bypass coagulation, sedimentation,

filtration, and absorption including PPCPs, estrogens, pesticides, dyes, alkylphenol surfactants, UV filters, and diesel fuel are subject to chemical transformations which can be encouraged through the use of high chlorine doses of 3.5-3.8 mg L^{-1} at acidic pHs for long contact times of >24 h.[20] Transformations include bromination, chlorination, iodination, oxidation, ring cleavage of phenols including most natural and synthetic estrogenic steroid hormones and combinations thereof. [5-7,20,21] As with biotic and abiotic environmental transformation products, the identities, persistence, and biological activity of DBPs are often unknown. The most common DBP found in drinking water is trichloromethane, also known as chloroform though brominated and iodinated trihalomethanes have also been detected and may be more toxic.[10,20,22] While the health effects of environmental doses of DBPs are unknown, trichloromethane and bromodichloromethane have been classified as possible human carcinogens.[22] Though elimination of these DBPs from the blood stream is rapid (the elimination half life is < 4 hours), exposures are so common that concentrations are usually found in the blood stream of most of the population.

These disinfection byproducts (DBPs) and their parent compounds persist in final treated water. Drinking water has been found to contain the parent compounds of PPCPs, steroid hormones, surfactants, industrial chemicals, and pesticides in concentrations ranging from 0.001 to 1 μg/L.[4] A recent report indicates that DEET was found in 90% of finished drinking waters.[7] Meprobamate, dilantin, ibuprofen and iopromide have been found in greater than 65% of finished drinking water.[7] Exposure to all of these occurs via ingestion of contaminated water, inhalation of air contaminated by the evaporation of them from contaminated water, and dermal absorption which occurs during bathing and

swimming.[20,22] Unfortunately, the human health effects of exposure to many MPs at environmentally relevant concentrations are often unknown though this is an area of active research.[7,8,11,22] Experiments that would permit the systematic, controlled gathering of whole organism human exposure data are unethical. In its stead, determination of toxicity to organisms, including observations of ecological toxicity, are often regarded as one indicator of the potential of an agent to harm human health.

Alternative disinfection processes such as chloramination have been associated with greater formation of iodinated trihalomethanes as well as formation of iodinated haloamides which have been observed to be very cytotoxic and genotoxic to mammalian cells.[20] Chloramination has also been found to generate greater quantities of nitrosamines, which are probable human carcinogens, than hypochlorite, chlorine dioxide, ozone, UV, and other advanced oxidation processes.[20] Ozone is also a potent disinfectant that forms fewer disinfection byproducts than chlorine but has a short half-life in water.[7] Consequently it cannot continue to disinfect in the distribution pipelines to prevent biological contamination as well as chlorine and thus is not an ideal replacement. Like chlorination, it has been observed to generate N-nitrosodimethyl amine (NDMA).[20] UV disinfection with a 40 mJ cm^{-2} dose has been employed, however it does not effectively remove EDCs and PPCPs with the exception of sulfamethoxazole, triclosan, and diclofenac having removals greater than 50%. Like Ozone, UV_{254} does not continue to work in the distribution pipelines to prevent biological contamination.

The most common water treatment technologies fail to completely remove all micropollutants, especially those that are small and polar. This results in their discharge to surface and ground waters resulting in contamination of receiving bodies,

transformation by disinfection processes, and the presence of these and the transformation products in finished drinking water.[5,7,23] High performing, low cost technologies that are capable of remediating aqueous MPs for both wastewater and municipal drinking water applications are needed, especially in areas where wastewater effluent contributes heavily to drinking source water.[8,10] Ozonation, advanced oxidative processes, activated carbon treatment, or membrane filtration are necessary to remove polar pharmaceuticals with certainty and even so, emoval efficiencies vary depending on many factors.[3] The application of such technologies to wastewater treatment would bring ecological and human health benefits by enabling us to remediate micropollutants before their release to the environment.[4] Such an advance would also enhance the quality of drinking water as less contaminated source waters are less difficult to purify.[10] Analogous advances in drinking water treatment would further safeguard consumers from exposure. Adsorption to activated charcoal and oxidative processes such as treatment with ozone have been advanced to meet this need.[8]

Adsorption based methods have been advanced as one such technology. However, its greatest strength, that it does not transform MPs and thus does not produce transformation products, is also a drawback of the technology.[8] Disposal of contaminated adsorbents can pose a threat to ecological and human health. For example, existing activated sludge disposal is complex. While other methods are available, one prominent method is the application of it to land. This practice facilitates the recycling the nutrients contained within sludge and enhances the sustainability of societies. However, sludge contamination with MPs presents a challenge to this venerable practice and has resulted in soil contamination. In central South Carolina agricultural land application of sludge to

agricultural lands was forced to a halt when polychlorinated biphenyl (PCB) contamination of sludge was discovered.[24] The disposal of other adsorbents is similarly challenging. For example, spent activated carbon usually must be incinerated.[8] The development of better regeneration strategies to avoid decreasing adsorbent performance and the rerelease of MPs to the environment has been advanced as one solution to this challenge.[10]

To avoid generating contaminated adsorbents, in situ remediation strategies including O_3 and AOPs including UV_{254}/H_2O_2, O_3/H_2O_2, O_3/H_2O_2 followed by UV_{254}, and UV_{254}/TiO_2 which rely upon the reactivity of the hydroxyl radical, aim to chemically transform micropollutants in water. Here the challenges lie in selecting active species capable of decomposing recalcitrant micropollutants, ensuring the safety of treated effluent which usually includes MP transformation products as well as the resultant disinfection byproducts upon potable water treatment with chlorine, minimizing the associated costs including energy consumption, dealing with interference from non-MP water components such as carbonate and dissolved organic carbon, and ensuring high material efficiencies.[8,9,25]

In order to advance real world water treatment, the Collins group has been developing the small molecule peroxidase enzyme mimics known as (TAML Activators— TAML® is a registered trademark of Carnegie Mellon University, covering tetra-organic-amido-N macrocyclic ligand complexes as claimed in a 2002 patent.[2627] TAML catalysts have and are being developed for application in wood pulp bleaching, household laundering, industrial and institutional cleaning, desulfurization of fuels, decontamination of chemical and biological weapons, industrial effluent treatment, as well as disinfection

and removal of micropollutants from water.[28-36]

This thesis documents work on (i) the evaluation of the technical and environmental performances of a novel subset of TAML activators, (ii) the collaborative development of an approach for measuring the rate of catalyst inactivation at the environmentally significant pH of 7, (iii) the systematic application of this approach to several TAML catalysts which elucidates novel structure activity relationships, and (iv) work towards the elucidation of entirely unanticipated mechanisms of the peroxide dependent and independent catalyst inactivation processes which are not initially oxidative in nature. The work contained herein comprises the foundation for a new and large class of compositions of matter, which we are calling TsAML, the early embodiments of which already display a better balance of technical, cost and environmental performances than TAML. We begin with an examination of the work that led to TAML technology in order to highlight the various ligand design elements necessary to attain catalysts that support high valent active catalyst intermediates that are resistant enough to degradation to perform useful catalysis as well as the process of discovering which metal center would yield high valent intermediates reactive enough to accomplish the oxidation of challenging substrates.

TAML Catalyst Development

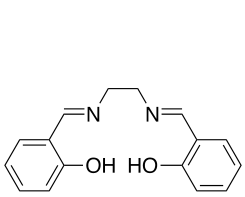

Salen

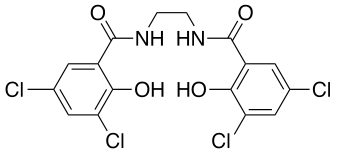

H_4**1**

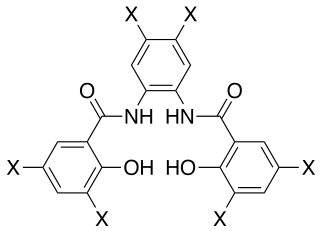

H_4**2**: X= Cl
H_4**3**: X=H

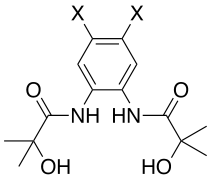

H_4**4**: X=H
H_4**5**: X=Cl

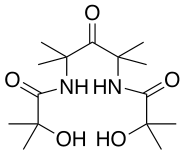

H_4**6**

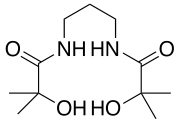

H_4**7**

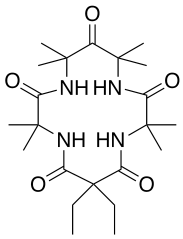

H_4**8**

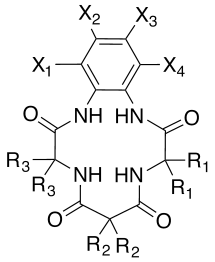

H_4**9**: X_1=X_4=H, X_2=X_3=Cl,
R_1=R_3=Me, R_2=Et
H_4**10**: X_1=X_2=X_3=X_4=H,
R_1=R_3=Me, R_2=Et
H_4**11**: X_1=X_4=H, X_2=X_3=OCH_3,
R_1=R_3=Me, R_2=Et
H_4**12**: X_1=X_4=H, X_2=X_3=CH_3,
R_1=R_3=Me, R_2=Et
H_4**14**: X_1=X_4=H, X_2=X_3=Cl
R_1=R_2=R_3=Me
H_4**15**: X_1=X_4=H, X_2=X_3=Cl
R_1=R_3=Me, R_2=F
H_4**16**: X_1=X_2=X_3=X_4=H,
R_1=R_2=R_3=Me

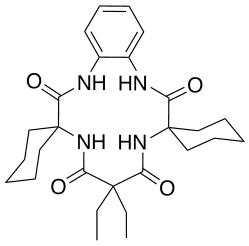

H_4**13**

Figure 1. Ligand structures referred to in Chapter 1.

TAML chemistry was born from a combination of amide and phenolic coordination chemistry, the first ligand was a salen-like complex with amides replacing the imines as shown in Figure 1.[37-46] The initial goal of the research program which became TAML development was to develop easy to synthesize and derivatize oxidation, hydrolysis, and displacement reaction resistant ligands that form five and six membered chelate rings to metal centers through multiple innocent anionic binding sites to enable the metal center to undergo oxidation and reduction cleanly with the goal of using the high-valent forms of these complexes to execute selective oxidations.[39,47,48] Tetradentate systems were selected in order to leave coordination sites open for ligand exchange processes.[27] The earliest published embodiment of this polyanionic chelating ligand (PAC) design protocol leading to TAML, H_4**1** is structurally similar to salen, the pyridine ligated cobalt complex of which was known to reversibly bind oxygen. However, amides were chosen for their known ability to stabilize high-valent metal centers when N-coordinated.[39] The electron-withdrawing chlorine groups were chosen for their ability to render the aromatic rings oxidation resistant. The crystal structure of $[Cr(\eta^3\text{-}H\mathbf{1})(Py)_2]_2\bullet 2py$, a dimer, is the earliest example of coordination of an amido nitrogen atom to Cr^{III}. This structure also displays coordination through the amido oxygen atom. Metallation of H_4**1** with $K_2[OsO_2(OH)_4]$ gave the potassium salt of the *trans*-dioxo **1** Osmium(VI) complex, $K_2[OsO_2(\eta^4\text{-}\mathbf{1})]$, the X-ray crystal structure of which shows it to be a monomeric species equatorially ligated by $[(\eta^4\text{-}\mathbf{1})]^{4-}$.[48] Reduction with PPh_3 gave a μ-oxo bridged dimeric Os^{IV} species which was structurally characterized.[48]

The trans ligated pyridine and tert-butyl pyridine (L) $[(\eta^4\text{-}\mathbf{1})]^{4-}$ Os complexes, *trans*-Os $(\eta^4\text{-}\mathbf{1})(L)_2$ were the next to be studied.[39] The ligand, $[(\eta^4\text{-}\mathbf{1})]^{4-}$, was observed to be

capable of supporting Os^{II}, Os^{III}, and Os^{IV} complexes. Since these were not observed to undergo deleterious hydrolysis or displacement they were deemed to be stable enough to investigate oxidation processes. When a dichloromethane (DCM) solution of *trans*-$Os(\eta^4$-**1**$)(L)_2$ and 500 equivalents of a simple alcohol ROH was oxidized electrochemically, irreversible redox potentials were observed indicating that the complex is unstable to oxidation. Careful analysis revealed that on silica gel the ethylene bridge of *trans*-$Os(\eta^4$-**1**$)(L)_2$ undergoes autooxidative dehydrogenation to give an ethene unit. Cyclic voltammograms of tetrabutylammonium perchlorate (TBAP) containing DCM solutions of this ethene bridged complex show three reversible processes and a fourth irreversible process. In the presence of alcohol or water, the third reversible process became irreversible. Chemical oxidation of a DCM solution of the ethene bridged complex by 2,3-dichloro-5,6-dicyano-1,4-benzoquinone (DDQ) in the presence of alcohol gave a 1,2 diether. In the presence of both alcohol and water, this same reaction gave unsymmetrically *trans*-substituted alkoxide and hydroxide bearing products as well as the two symmetrically *trans*-substituted products. Electrochemical oxidation of TBAP and alcohol or water containing DCM solutions of these gave new osmium complexes resulting from cleavage of the bridge C—C bond and formation of two formyl units from its carbon atoms. X-ray structures of these complexes show them to consist of Os coordinated by two bidentate ligands each of which is bound to the metal through a phenolate oxygen and an imide nitrogen atom.[39] The proposed mechanism of the process is shown in Figure 2.

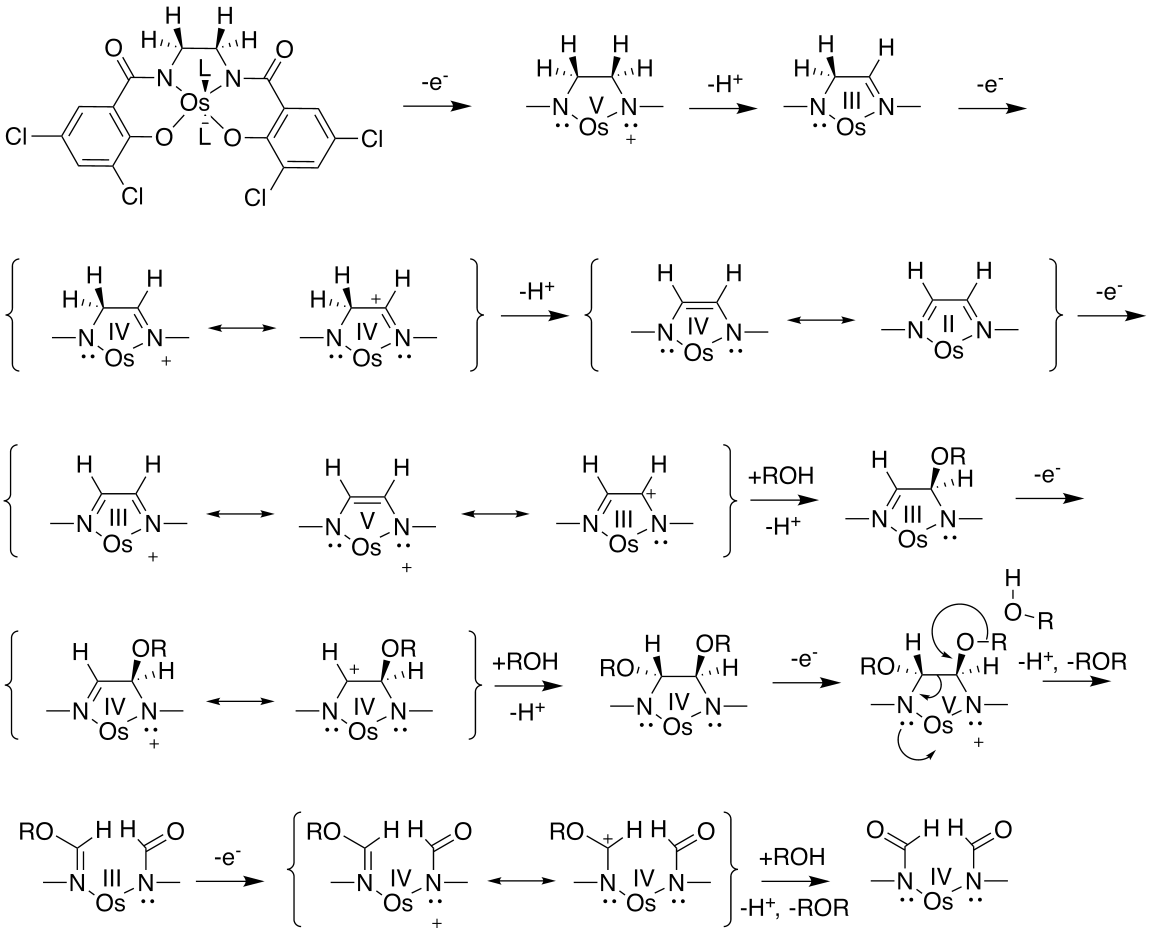

Figure 2. Proposed *trans*-Os(η^4-**1**)(L)$_2$ degradation pathway.

The remaining two coordination sites are occupied by substituted pyridine molecules the spatial relationship of which (cis or trans) is sensitive to the identity of the pyridine substituent. Later work more fully explored this sequence of events further establishing the ethane bridge as the site of ligand degradation.[49] Further evidence of solvent participation was later established through oxidation of *trans*-Os(η^4-**1**)(py)$_2$ in liquid SO_2 at -60 °C, under these H_2O and alcohol free conditions this third redox event is observed to be reversible.[50]

Since the ethane bridge was observed to be a site of instability under highly oxidizing conditions, a chlorine substituted phenylenediamine residue was incorporated in its place

to give H_4**2**. Cyclic voltammograms of a TBAP containing DCM solution of *trans*-Os(η^4-**1**)(*t*-Bupy)$_2$ show 4 reversible couples with the first only 0.06 V greater than that of *trans*-Os(η^4-**1**)(L)$_2$ and the fourth analogous to the irreversible process observed for *trans*-Os(η^4-**1**)(L)$_2$. The smallness of the perturbation of the first redox potential was later interpreted as an indication that the oxidation equivalent resides on the metal center.[48] The reversibility of the fourth *trans*-Os(η^4-**2**)(L)$_2$ redox potential demonstrates the resistance of **2** to the **1** degradation pathway. Electrolysis of a *trans*-Os(η^4-**2**)(L)$_2$ solution at 1.0 V gave a mixture of rare Os^V complexes. The redox potential of the $Os^{V/IV}$ couple of was shown to be sensitive to the identity of the axial ligands chosen. Later experiments in liquid SO_2 where decomposition of the H_4**1** ethane bridge is not observed showed the monocation/Os^{IV} redox potential of *trans*-Os(η^4-**1**)(py)$_2$ to be 40 mV larger than that of *trans*-Os(η^4-**2**)(py)$_2$ indicating that resonance contributions which effectively store oxidation equivalents on the 4,5-dichloro-benzene-1,2-diamine bridge do not contribute heavily to the structure of the monocation.[50]

Metallation of **2** with Co(O_2CCH_3)$_2$ gave Na[*trans*-Co(η^4-**2**)(*t*-Bupy)$_2$] which was chemically oxidized with 1.0 equivalents of ceric ammonium nitrate (CAN) to give *trans*-Co(η^4-**2**)(*t*-Bupy)$_2$, the strucrural characterization of which showed no evidence of distortions of ligand structure that would indicate oxidation of the ligand lending support for formulation as a true Co^{IV} complex.[51] Cyclic voltammograms of Na[*trans*-Co(η^4-**2**)(*t*-Bupy)$_2$] show two reversible couples at +0.39 and +0.84 V vs Fc^+/Fc. The ligand alone showed an irreversible redox couple at +0.60 V. This was interpreted as evidence that the first redox event is metal centered. The UV and EPR spectra of the first electrochemical oxidation product match those of *trans*-Co(η^4-**2**)(*t*-Bupy)$_2$ generated by CAN treatment.

The first redox potential was observed to be sensitive to PAC structure with that of Na[*trans*-Co(η^4-**3**)(*t*-Bupy)$_2$] 0.16 V less than that of Na[*trans*-Co(η^4-**2**)(*t*-Bupy)$_2$] as well as to the identity of the axial ligands with the 4-dimethylaminopyridine (DMAP) analog, Na[*trans*-Co(η^4-**2**)(DMAP)$_2$], 0.06 V less. This example of the first isolable Co^{IV} complex was regarded as further evidence of the ability of PACs to support metal centers in high-valent oxidation states.

A structural characterization of a crystal of the Na salt of the green Cobalt complex of the more electron donating **3**, Na[Co(η^4-**3**)]•$(CH_3)_2O$ grown from acetone showed it to be a rare square planar Co^{III} complex.[52] Magnetic studies of the solid states of both this complex and the Ph_4P^+ salt revealed that both obey the Curie-Weiss law from 50–300 K with μ_{eff} of 3.26 and 3.41 μ_b, respectively, at 300 K and limiting μ_{eff} values of 1.41 and 1.54 μ_b, respectively, at 6 K which are characteristic of zero-field splitting. These are as expected for complexes having spin triplet (S = 1) ground states. From the similarity of the Ph_4P^+ salt magnetic moments of 3.1–3.3 μ_b measured in DCM and tetrahydrofuran (THF) solutions and lack of observable visible spectra changes on addition of pyridine to these solutions, it was concluded that the complex likely remains four coordinate in aprotic solvents—however addition of excess $NaClO_4$ to acetone solutions afforded a deep green color. Aqueous green solutions of the Na^+ salt were observed to have a magnetic moment of 5.1 μ_b indicating a high spin quintet S = 2 state. On coordination of two pyridines, similar aqueous solutions were observed to fade to pale yellow concluded to result from formation of the six coordinate complex. The similarity of this behavior to that of Fe^{II} porphyrins was noted indicating that these highly donating

ligands may alter the coordination chemistry of metal centers endowing them with reactivities like that of the isoelectronic forms of their larger neighboring element.

The reaction of *trans*-Os(η^4-**3**)(Ph_3P)$_2$ with trimethylsilyl and methyl azides yielded nitrido products.[53] However, the reaction of *trans*-Os(η^4-**3**)(Ph_3P)$_2$ with phenyl azide was observed to give a complex in which Os is chelated by the PAC ligand in a *cis*-β-geometry and a bidentate phenylenediamine analogue as shown in Figure 3 below.

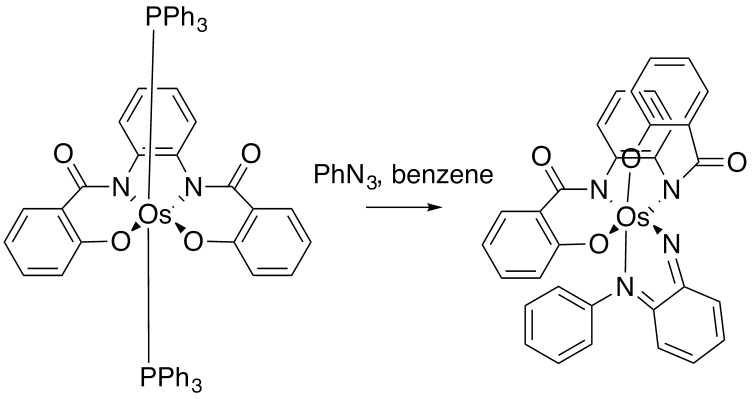

Figure 3. Bidentate phenylenediamine analog product formation.

The proposed reaction mechanism involves C—H bond activation by an Os^{VIII} bis(imido) intermediate providing another indication of the ability of PAC ligands to stabilize metals in high-valent states and provides an example of isomerization to give nonplanar amides.[53] The reactions of *trans*-Os(η^4-**2**)(Ph_3P)$_2$ and *trans*-Os(η^4-**3**)(Ph_3P)$_2$ with the π electron acceptors carbon monoxide and *tert*-butyl isocyanide also yielded products in which the PAC ligand isomerized to a *cis*-α form as shown in Figure 4.[54]

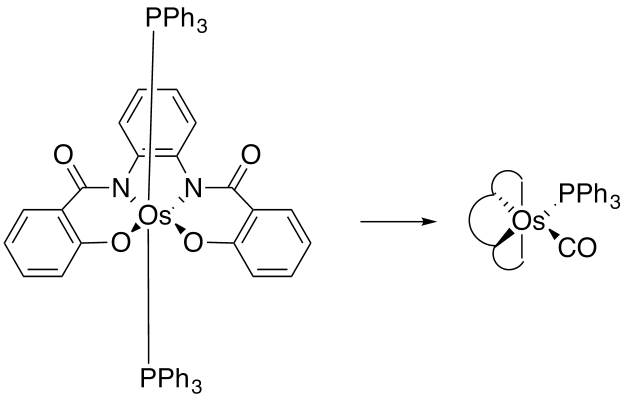

Figure 4. Reaction of *trans*-Os(η^4-**3**)(Ph_3P)$_2$ with CO.

It was concluded that the binding of these π acid ligands alone indicates that the PAC ligands are potent enough electron donors to render Osmium(IV) basic. Crystal structures of *cis*-α-Os(η^4-**2**)(*t*-BuNC)(Ph_3P) and *cis*-α-Os(η^4-**3**)(CO)(Ph_3P) revealed each to possess nonplanar amides. Analysis of all RC(O)NR'M and RC(OM')NR'M amide structures where R and R' ≠ H in the Cambridge database revealed the twist angles about the amido C—N bonds of *cis*-α-Os(η^4-**3**)(CO)(Ph_3P) and *cis*-α-Os(η^4-**2**)(*t*-BuNC)(Ph_3P) to be the largest observed to date. Studies of the properties of these complexes revealed that rotation about the amido C—N bond decreases delocalization of the N lone pair to the carbonyl carbon resulting in a stronger bond between the carbonyl carbon and oxygen indicated by an increase in the frequencies of the CO_{amide} IR bands versus those of the parent complexes. These ν_{CO}(amide) values were found to vary with the C—N twist angle. In metal complexes where the amide nitrogen atoms are aligned trans to the π acceptor ligand, the former were not observed to undergo as much pyrimidalization as observed for complexes placing the amide nitrogen atoms trans to phosphine ligands. This was interpreted as evidence of increased π donation. The observed deformations of the amides indicates that donation of amido-N electron density to the metal centers of

Os(η^4-**2**)(*t*-BuNC)(Ph_3P) and Os(η^4-**3**)(CO)(Ph_3P) is thermodynamically preferred over donation to the carbonyl carbon. This was further indicated by a lack of isomerization upon heating the complexes. The sum of the result was concluded to be that amides may adopt nonplanar conformations in order to better satisfy the demands of electrophilic metal centers.

Later work showed that amides of coordination complexes can also adopt nonplanar conformations which are enforced by steric interactions.[55] Studies of the treatment of square planar Na[Co(η^4-**6**)] with two equivalents of KCN resulted in the formation of Co(η^4-**6**)$(CN)_2^{3-}$ the structural characterization of which revealed it to be octahedral with the two CN ligands *cis* and the PAC amido C—N bonds twisting to give nonplanar amides.[56] It was noted that this twisting is less favorable than nonplanar amide formation by pyramidalization of the planar amido nitrogen, a less energetically demanding process. The retention of planarity of the amido N atoms was interpreted as evidence that binding to the metal dπ orbitals requires a nitrogen p orbital. It was noted that π backbonding to the CN ligands may encourage this N planarity.

The better ability of nonplanar amides to satisfy high valent metal centers was further observed in electrochemical studies of *trans*-Os(η^4-**2**)(*t*-Bupy)$_2$, the cyclic voltammogram of which shows three reversible couples. Controlled potential electrooxidation of *trans*-Os(η^4-**2**)(*t*-Bupy)$_2$ by 1 Faraday mol^{-1} resulted in a solution the cyclic voltammogram of which shows two sets of three reversible couples, the couples of the first set were up to 510 mV less than those of the second which matched those of *trans*-Os(η^4-**2**)(*t*-Bupy)$_2$ indicating its presence along with a more electron rich and easily oxidized complex which was determined to be *cis*-α-Os(η^4-**2**)(*t*-Bupy)$_2$. The two

complexes were separated by column chromatography following reduction by addition of excess ferrocene at -78 °C. At -78 °C, cyclic voltammograms of solutions of each after electrooxidation by 1 Faraday mol^{-1} at -78 °C show the couples for only one complex however cyclic voltammograms recorded after warming each solution to room temperature show the six reversible couples of the mixture indicating that the two forms have equilibrated. The equilibrium constants K^{2-}, K^{-}, K^{0}, and K^{+}, with superscripts corresponding to the total charge on the complex, for isomerization from *cis*-α to *trans* were calculated for each of the four oxidation states represented by the three couples. The equilibrium constants decrease by orders of magnitude as overall charge of the complex increases indicating that the population shifts further towards the *cis*-α isomer as the oxidation state of the complex increases. A series of complexes with pyridine ligands having different para substituents was prepared and studied by electrochemistry in order to determine if the equilibrium constants correlate with the Hammett parameters of each. The formal potentials of these complexes were found to increase with the Fischer parameter of the pyridine substituent. Hammett plots revealed linear correlation between σ_p and log K^0 with a negative ρ value. This was interpreted as evidence that the *cis*-α population of isomers at equilibrium increases as donation of electron density to the metal center by the pyridine ligands decreases. By analogy to the π acceptor containing *cis*-α-Os(η^4-**2**)(*t*-BuNC)(Ph_3P) and *cis*-α-Os(η^4-**3**)(CO)(Ph_3P) and by the synthesis and IR characterization of *cis*-α-Os(η^4-**2**)(*t*-BuNC)$_2$ and *cis*-α-Os(η^4-**3**)(*t*-BuNC)(Ph_3P). It was concluded that the *cis*-α isomers contain nonplanar amides. This work is further proof that these complexes isomerize to forms containing nonplanar amides to stabilize high valent metal centers through increased donation of electron density. From this work

it was concluded that PAC ligands intended to produce potent oxidants should not be able to isomerize to incorporate nonplanar amides as doing so reduces the redox potential of the high valent states. Employment of macrocyclic (MAC) ligands such as **8-16** was proposed to achieve this.

Later studies provide evidence that the conformational change proceeds via an isomerization twist mechanism.[57] The equilibrium isomerization of *trans*-Os(η^4-**2**)$(OPPh_3)_2^+$ to the *cis*-α conformation in solutions containing OP(p-Tol)$_3$ did not result in complexes containing this ligand. In addition, the composite rate constants for the isomerization, $k_{obs} = k_f + k_r$, did not show great sensitivity to solvent polarity or the addition of excess $OPPh_3$, and the process was observed to be impacted little by the addition of *p*-toluenesulfonic acid. Studies of the isomerization of *cis*-α to *trans*-Os(η^4-**2**)$(OPPh_3)_2$ in solutions containing OP(*p*-Tol)$_3$ did not result in complexes containing this ligand. The rate of the process showed little sensitivity to changes in solvent polarity or the addition of excess $OPPh_3$, and showed no evidence of products formed from interaction with a radical intermediate when conducted in 2-mercaptoethanol as well as solutions containing excess hydroquinone. A positive reaction enthalpy 12 ± 3 kcal mol^{-1} and a positive reaction entropy of 42 ± 2 eu determined by construction of a van't Hoff plot of K^+, the equilibrium constant for isomerization of Os(η^4-**2**)$(OPPh_3)_2^+$, measured over the temperature range 2.2-30.2 °C were observed and rationalized as resulting from the stronger N—Os bonds of the *cis*-α isomer nonplanar amides and either ion-pairing or solvation differences, respectively. The *cis*-α to *trans* isomerization of the cationic forms was observed to proceed with a small positive enthalpy of activation of 24 ± 6 kcal mol^{-1} and an entropy of activation of 17 ± 2 eu. The *cis*-α to *trans* isomerization of the neutral

forms was observed to proceed at a rate 2 orders of magnitude less than those of the cations with the similar enthalpy of activation of 22 ± 2 kcal mol^{-1} and no measurable reaction entropy. The small positive reaction enthalpies are not consistent with bond breaking contributions to the transition state as would be expected for a dissociative mechanism. The difference in the reaction rates was hypothesized to result from decreases in the activation energy due to a more stable cation transition state deriving from decreased repulsion between the dπ electrons and those of the chelating anion, though the enthalpy of activation values overlap when error is considered. Alternatively this could be considered to result from a destabilization of the *trans* form of the cation which could result from a decrease in the ligand-metal bonding interactions due to inability of the planar form of the ligand to compensate for a reduction in the atomic radius of the oxidized Os. Consequently, it was concluded that the conformational changes of both the neutral and cationic forms likely proceed via a similar isomerization twist mechanism rather than one involving ligand dissociation with or without formation of a radical intermediate having a long enough lifetime to undergo intermolecular trapping, a process that could not be overcome by altering the identity of the axial ligands.

Metallation of PAC ligands **1**, **2**, **4**, **5,** and **6** with $Cu(OAc)_2$ and subsequent oxidation gave the series of rare Cu^{III} complexes $[Cu(\eta^4\text{-}\mathbf{1})]^-$, $[Cu(\eta^4\text{-}\mathbf{2})]^-$, $[Cu(\eta^4\text{-}\mathbf{4})]^-$, $[Cu(\eta^4\text{-}\mathbf{5})]^-$, and $[Cu(\eta^4\text{-}\mathbf{6})]^-$.[58] Structural characterization of $[Ph_4P][Cu(\eta^4\text{-}\mathbf{4})]\bullet 2H_2O$ found the molecular geometry about the copper atom to be square planar with Cu—N_{amido} bond lengths similar to those found for Cu^{III} complexes. Cyclic voltammetry of $[Cu(\eta^4\text{-}\mathbf{1})]^-$, $[Cu(\eta^4\text{-}\mathbf{2})]^-$, $[Cu(\eta^4\text{-}\mathbf{4})]^-$, $[Cu(\eta^4\text{-}\mathbf{5})]^-$, and $[Cu(\eta^4\text{-}\mathbf{6})]^-$ revealed these to have very low

$Cu^{III/II}$ redox potentials again indicating that PAC complexes are very strong donors. Observation of a $[Cu(\eta^4\text{-}\mathbf{6})]^-$ $Cu^{III/II}$ redox couple was regarded as evidence that the oxidation is metal centered since PAC **6** cannot donate electrons to the metal center by resonance. A 135 mV increase in the $Cu^{III/II}$ redox potential was observed on going from the innocent PAC complex $[Cu(\eta^4\text{-}\mathbf{6})]^-$ to the noninnocent PAC complex $[Cu(\eta^4\text{-}\mathbf{4})]^-$ indicating that the oxidation of the latter was not likely to be attributable to that of the phenelyenediamine residue. The 25 mV increase in the $Cu^{III/II}$ redox potential observed upon aromatic substitution of the PAC complex $[Cu(\eta^4\text{-}\mathbf{4})]^-$ with chlorine atoms to give $[Cu(\eta^4\text{-}\mathbf{5})]^-$ was attributed to a decrease in ligand donation to the metal center on appendage of electron-withdrawing groups. PAC ligands $H_4\mathbf{2}$ and $H_4\mathbf{4}$ were not observed to undergo oxidation below 0.600 V and 0.750 V, respectively, 0.525 V and 0.725 V above the highest observed redox potential for the metallated complexes, respectively. Redox potentials were found to increase as aliphatic groups were replaced with aromatic groups across the series indicating that the position of the redox couple is dependent upon the capacity of the ligand bound atoms to donate electron density to the metal center. The opposite trend would be expected if the aromatic rings contribute to the stabilization of the Cu^{III} form by resonance. While the site of oxidation was not assigned definitively, taken together these observations are best rationalized by metal centered oxidations in all cases indicating these complexes are best described as Cu^{III} complexes. It was noted that in octahedral complexes, a plane of strong σ donating ligands destabilizes orbitals that are orthogonal to this plane due to their possession of lobes it which can in turn weaken bonds to axial ligands. This can result in higher exchange rates at these locations and can even render these sites unoccupied in a given solvent as evidenced by the research on

anionic Co^{III} PAC complexes.[59] This effect could be very useful for generating catalysts as turnovers require labile metal sites. Unfortunately, Cu^{IV} was not observed.

The Ph_4P^+ and Na^+ salts of a similar square planar Co^{III} PAC ligand system, Na and Ph_4P[Co(η^4-**4**)], was observed to slowly catalyze the oxidation of styrene by iodosylbenzene, iodosylmesitylene, and pentafluorophenyliodosylbenzene in CH_3CN at 0 °C to give styrene oxide and phenylacetaldehyde in a 4.75:1 ratio.[59] Additional complexes, Na[Co(η^4-**5**)], Na[Co(η^4-**6**)], and Na[Co(η^4-**7**)], were also observed to catalyze this oxidation by iodosylbenzene under identical conditions. In these cases, catalysis was limited by the quantity of added oxidant and not instability of the catalyst itself. The activity of Na[Co(η^4-**2**)]•H_2O, which contains a bound axial ligand, was also examined however a turnover number of 1.0 was observed indicating that the process does not represent true catalysis. The best performance was observed for Na[Co(η^4-**6**)], an innocent ligand complex. The contrast between the stoichiometric performance of Na[Co(η^4-**2**)] versus the catalytic performance of Na[Co(η^4-**6**)], which has a more strongly donating ligand due to its possession of alkoxides rather than phenolates, was interpreted as a further indication that strongly donating ligand systems are required in order to labilize the axial ligands, a necessary property for catalysis.

From this work it was concluded that if catalysis proceeds via a mechanism like that proposed for cytochrome-P450 oxygen atom transfer, it may do so through a Co^V-oxo complex. Similar chloro(tetraphenylporphyinato)cobalt^{III} catalysis of alkene oxidation by cumyl hydroperoxide had been proposed to occur via a radical mechanism in which a Co^V complex was been implicated as the active species suggesting that peroxides may also function as a sacrificial oxidant in catalysis by PAC coordination complexes. Future

work was dedicated to finding a stable form of this intermediate. Attempts were also made to generate chiral forms of H_4**4**, H_4**6**, and related ligand systems and their Co^{III} complexes having varied alkyl substituents at the alkoxide bearing carbons to give chiral centers with the goal of carrying out asymmetric epoxidations returned fair to good yields of epoxide of 25–86% with very low enantiomeric excesses of 0–17%.[60] Further research on alkylation of the amido nitrogen of Co^{III} PAC complexes, the first neutral square planar Co^{III} complexes, provides additional evidence for the ability of strongly donating ligands to labilize sites on metal centers.[59,61]

The proposal of a Co^{V} PAC-oxo intermediate in the oxidation of styrene, the similarity of this complex to the cobalt porphyrin catalysis of oxidation by cumyl hydroperoxide, and work in the porphyrin field indicating that Manganese(V) porphyrin-oxo complexes are the reactive intermediates in catalytic oxygen atom transfers led to the investigation of the reaction between Na[Mn(η^4-**4**)] and *tert*-butyl hydroperoxide at room temperature which gave a stable Mn^{V}-oxo complex that was characterized, the first authenticated Mn^{V}-mono-oxo complex.[62] The complex was observed by ^{1}H NMR in CD_3CN to be diamagnetic as expected for a square pyramidal Mn^{V} complex. The crystal structure revealed it to be square pyramidal with the shortest manganese-oxo bond ever observed consistent with its formulation as a triple bond. The position of the metal center above the plane of the ligand chelating atoms was postulated to be a consequence of this strong bonding to oxygen. Bond lengths of the aromatic ring and those between the ring and the nitrogen atoms were consistent with those expected for an aromatic system and a single sp^2 carbon to sp^2 nitrogen bond, respectively, indicating that no oxidation of the ligand system had occurred. The latter were observed to be 0.01-0.02 Å longer than

those of than those of $Et_4N[Mn(\eta^4\text{-}\mathbf{4})]$, a further indication of this. Consequently, it was concluded that the complex is best considered a true Mn^V complex and that the oxidation which generates it is metal centered. The absence of isomerization to a *cis*-α form in order to better stabilize this high valent state was noted. Unfortunately, $[Mn(\eta^4\text{-}\mathbf{4})]$ was found to be unstable in water.[63]

Consequently, macrocyclic anionic chelating ligand (MAC) $H_4\mathbf{8}$ was generated.[64] At this time the observations of Dale Margerum in studies of Cu^{III} tripeptide complexes that undergo intramolecular hydrogen abstraction by an amido N atom from the carbon atom β were noted.[41] This degradation was prevented by altering the ligand structure to incorporate sp^2 or quaternary sp^3 carbons. For this reason, $H_4\mathbf{8}$ and $H_4\mathbf{9}$ contain no β hydrogen atoms.[65] Metallation with cobalt gave $Li[Co(\eta^4\text{-}\mathbf{8})]$, the ^1H NMR spectrum of which showed paramagnetically shifted ^1H NMR signals as anticipated for a square planar Co^{III} complex. Structural determination of $Et_4N[Co(\eta^4\text{-}\mathbf{8})]$ revealed it to adopt a distorted form of square planar shape which is rare for Co^{III} complexes. The structure contains a nonplanar amide which was postulated to result from a mismatch in the size of the alternating chelating ring system (6,5,6,5) with the structural preferences of the Co^{III} center. Consequently, the 5'5'5'6 chelate forming ligands $H_4\mathbf{9}$-$\mathbf{16}$ were studied.

The $Mn^V{\equiv}O$ complex $[Mn\text{-}O(\eta^4\text{-}\mathbf{9})]^-$ was generated and found to be stable in aqueous solutions.[63] X-ray crystallography of the Et_4N^+ salt showed the complex to be square pyramidal with a Mn≡O bond length of 1.555±4 Å and the Mn atom to be nearly centered in the pocket of the 5,5,5,6 chelate ring system 0.60 Å above the N atom plane. The Mn—N bonds to the aromatic amido N were observed to be ca 0.01 Å shorter than those to the aliphatic amido N. Bond distances in the aromatic ring and to the aromatic N

atoms were observed to be consistent with those of an aromatic system and that between sp^2 C and N indicating that resonance forms resulting from oxidation of the ring do not contribute to the structure significantly. ^{1}H NMR revealed it to be diamagnetic as expected for a low-spin d^2 square-pyramidal complex. Exchange of the oxo oxygen with that of $H_2{}^{18}O$ led to IR assignment of the first $\nu_{Mn\equiv O}$ as 979 cm^{-1} and 942 cm^{-1} for the ^{16}O and ^{18}O complexes, respectively. These complexes were found to be unreactive (Dr. Collins, private communication). It was proposed that the chelates were too electron rich and as a result were quenching the reactivity. Consequently, similar complexes were designed to incorporate a cation binding site on the ligand structure in electronic coordination with the metal center.[66] These were found to be reactive when employed in the presence of cations however, the approach was considered to be too complex to be commercially useful.

To examine the relationship between the structures of MAC ligands and that of their high valent metal-oxo complexes, particularly the role of the ligand as an electron donor to the metal center, the Cr^V-oxo complexes of innocent **8** and potentially noninnocent **9** were generated and characterized by IR, X-ray crystallography, and EPR.[65] The Me_4N^+ salts of each were stable in water. Unlike [Mn-O(η^4-**9**)]$^-$ both only underwent very slow exchange of the oxo oxygen atom with $H_2{}^{18}O$. Consequently, $(CH_3)_2(H^{18}O^{18}O)CCH_2CH_2C(^{18}O^{18}OH)(CH_3)_2$ was synthesized and employed to generate [Cr-^{18}O(η^4-**8**)]$^-$ and [Cr-^{18}O(η^4-**9**)]$^-$ from the respective Cr^{III} complexes which were observed to have IR $\nu_{Cr\equiv{}^{18}O}$ stretches of 941 and 944 cm^{-1}, in contrast to IR $\nu_{Cr\equiv{}^{16}O}$ stretches of 982 cm^{-1} observed for both of the analagous ^{16}O complexes. Structural analysis revealed Cr bond lengths of 1.569 ± 0.002 and 1.580 ± 0.006 Å, respectively.

The Cr atom of [Cr-O(η^4-**8**)]$^-$ is centered in and 0.58 Å above the mean plane of the chelating N atoms which alternate between 0.12 Å above and below this plane. The Cr atom of [Cr-O(η^4-**9**)]$^-$ is centered in and 0.60 Å above the planar chelating N atoms. Nonplanar amides were observed for both though all of four of those of [Cr-O(η^4-**8**)]$^-$ were observed to be nonplanar with three more distorted than any of the nonplanar amides of [Cr-O(η^4-**9**)]$^-$. Evidence for the assignment of the Cr^V oxidation state for both complexes was found by comparing the EPR spectra of the innocent ligand chelated [Cr-O(η^4-**8**)]$^-$ and the potentially noninnocent ligand chelated [Cr-O(η^4-**9**)]$^-$. The EPR spectra of both complexes show signals consistent with those expected for Cr^V centered radicals with nine-line first derivative signals at g = 2.006 G, respectively, indicating superhyperfine interactions with four spectroscopically equivalent ^{14}N donor atoms (I = 1) with a_0 = 2.6 and 2.7 G, respectively, observed for the I = 0 Cr nuclei which comprised 90.45% of the sample and less strong four-line features for the I = 3/2 ^{53}Cr nuclei comprising 9.54% of the sample with A_0 = 17.8 and 17.9 G with g = 1.999. Unfortunately, these chromium-oxo complexes were observed to be stable and did not transfer oxygen atoms to olefins.[67,68]

Since high valent iron complexes are known to be intermediates in biological oxidation processes and attempts at isolating iron PAC complexes yielded aggregates, there was much interest in studying iron MAC complexes. Presumably, the ethyl groups of H_4**8** and H_4**9** were appended in because diethyl substituted malonic acid was cheaper than dimethyl and there was no reason to suspect the former would perform any worse than the latter.[69] The first reported iron MAC complex, $[Et_4N]_2$[FeCl(η^4-**8**)], was generated by metallation of H_4**8** and oxidation to Fe^{III} by oxygen.[70] X-ray crystals of the

compound revealed it to be square pyramidal with the Fe atom 0.32 Å above the plane of the amido N atoms.[71] Cyclic voltammetry revealed $[Et_4N]_2[FeCl(\eta^4\text{-}\mathbf{8})]$ to have a very low $Fe^{IV/III}$ redox couple in CH_2Cl_2 of -65 mV vs Fc^+/Fc. Oxidation of $[Et_4N]_2[FeCl(\eta^4\text{-}\mathbf{8})]$ by $(NH_4)_2Ce(NO_3)_6$ gave $[Et_4N][FeCl(\eta^4\text{-}\mathbf{8})]$, the X-ray crystal structure of which revealed it to be a distorted square pyramid with the Fe atom 0.42 Å above the plane of the amido N atoms, 0.1 Å greater than that of $[FeCl(\eta^4\text{-}\mathbf{8})]^{2-}$. The Fe—N and Fe—Cl bonds of $[FeCl(\eta^4\text{-}\mathbf{8})]^-$ were observed to be 0.025 and 0.1 Å shorter than those of $[FeCl(\eta^4\text{-}\mathbf{8})]^{2-}$ form, respectively. Zero field Mössbauer spectra of $[Et_4N][FeCl(\eta^4\text{-}\mathbf{8})]$ collected at 150 K showed a doublet at δ_{Fe} = -0.03 mm s^{-1} with a nearly temperature independent $|\Delta E_Q|$ of 0.87 mm s^{-1}. Mössbauer spectra of $[FeCl(\eta^4\text{-}\mathbf{8})]^-$ collected at 4.2 K in fields > 0.5 T showed magnetic hyperfine interactions indicating that this compound has ground state electronic spin $S > 0$ consistent with that expected for a high spin d^4 iron atom in a square pyramidal crystal field, the first such Fe^{IV} complex. The 4.2 K isomer shift value of δ_{Fe} = 0.01 mm s^{-1} is similar to 0.03-0.11 mm s^{-1}, the range of values found for Fe^{IV}, $S = 1$ heme complexes at 4.2 K supporting assignment of the Fe^{IV} oxidation state. Unfortunately, $[Fe(\eta^4\text{-}\mathbf{8})]^-$ was observed to be prone to hydrolysis of the N—Fe bonds.

The Ni^{III} complex, $[Et_4N][Ni(\eta^4\text{-}\mathbf{8})]$ was synthesized, structurally characterized, and examined by cyclic voltammetry and EPR.[72] Like other MAC complexes, it was found a low $Ni^{III/II}$ redox potential of -0.58 V vs Fc^+/Fc in CH_2Cl_2 with 0.01 M $[Bu_4N][ClO_4]$ supporting electrolyte. X-ray analysis of crystals revealed $[Et_4N][Ni(\eta^4\text{-}\mathbf{8})]$ to be distorted square planar with chelating amido N atoms 0.25 Å above and below the mean plane in alternating fashion and Ni 0.09 Å above it. Like other **8** complexes, one of the

amides of the structure is very nonplanar. Solutions of [Ni(η^4-**8**)]$^-$ were observed to be purple regardless of whether the solvent was 20 °C CH_3CN, C_6H_5N, $(CH_3)_2CO$, 2,5-Me_2THF, THF, CH_2Cl_2, H_2O, or CH_3CH_2OH; 77 K H_2O, CH_3CN, $(CH_3)_2CO$, 2,5-Me_2THF, THF, CH_2Cl_2; or 77 K CH_2Cl_2 solutions with Cl^-, Br^- Ph_3P, or Et_3N. This was interpreted as evidence that the four coordinate complex is purple and like other MAC and PAC complexes does not have high affinity for axial ligands. However, CN^- addition to [Ni(η^4-**8**)]$^-$ in any of the 20 °C solvents listed changes the purple solutions to yellow. Addition of CH_3CH_2OH, C_6H_5N, 2,6-lutidine, or $(CH_3)_3P$ to purple 2,5-Me_2THF solutions and cooling the mixture to 77 K gives green or yellow glass. The CN^- adduct was determined to have a mole ratio of 1:1. These data were taken as an indication that [Ni(η^4-**8**)]$^-$ adducts with coordination numbers higher than four are pale green or yellow. EPR spectra (9.46 GHz) of frozen yellow samples of [Et_4N][Ni(η^4-**8**)] in CH_2Cl_2 with excess CN^- at 4 K, and that of [Ni(η^4-**8**)]$^-$ in a yellow, 2:1, 2,5-Me_2THF/ C_6H_5N glass at 5 K were rhombic with $g_1 = 2.234$, $g_2 = 2.159$, $g_3 = 2.019$; and $g_1 = 2.380$, $g_2 = 2.269$, $g_3 = 1.994$; respectively, as expected for coordination of one CN^- and one C_6H_5N, respectively. EPR spectra of a purple, anhydrous, 2:1 Toluene/CH_2Cl_2 [Ni(η^4-**8**)]$^-$ glass gave $g_1 = 2.366$, $g_2 = 2.303$, $g_3 = 1.994$ at 5 K with $g_\perp > g_\parallel$, the opposite of the EPR signature of $g_\parallel > g_\perp$ accepted for square-planar Ni^{III} complexes at the time. The EPR spectrum of an identical sample did not change when the solvent system was saturated with $H_2{}^{16}O$ and 45% enriched $H_2{}^{17}O$ indicating that no binding of trace water or solvent molecules occurs and that the purple glass samples are largely composed of the four coordinate complex. Later work on the synthesis and characterization of [Ni(η^4-**9**)]$^-$ found it to be best considered as a Ni^{III} complex as well.[67] This is further evidence of the

strongly donating properties of this tetraamido macrocyclic ligand system (TAML). An evaluation of the properties of $[(\eta^4\text{-}\mathbf{8})]^{4-}$ Co, Ni, and Cu complexes led to the conclusion that the strongly donating MAC ligand system destabilizes an antibonding metal d-orbital leading to a redistribution of d electrons amongst the remaining four d orbitals.

The sum of these observations led to the first publication on the design of ligands capable of yielding stable high valent transition metal complexes.[73] This work includes the previous design rule that β hydrogens should be avoided as well as other observations. It was hypothesized that ligand systems intended for use in stabilizing high valent transition metal complexes should not incorporate hydrogen atoms in positions where the lone pairs of their heteroatoms can overlap the σ* orbital of the C—C bonds. This derives from the mechanism of decomposition of 1,2-diether, -diol, or 1-ether-2-ol which were formed from ethene bridged intermediates in the previously discussed electrolysis of *trans*-Os(η^4-**1**)$(L)_2$ complexes that led to the design of H_4**2** and H_4**3**. It was also proposed that such ligands should lack chelating atoms having lone pairs that can access the σ* orbital of ligand backbone C—C bonds, this was proposed as a reason for the shift to amido nitrogen atoms of H_4**8** and H_4**9** in place of the alkoxide oxygens of H_4**1-7**. It was proposed that the ligands should be macrocyclic as this provides extra stability to the chelates via the macrocycle effect and should minimize homolysis of bonds between the metal and chelating atom, a process not found to contribute to ligand degradation in previous studies of the isomerization of *cis*-α to *trans*-Os(η^4-**2**)$(OPPh_3)_2$. Innocent ligands such as H_4**8** were proposed to be preferred over noninnocent ligands such as H_4**9** as the former cannot donate electron density to the metal center by resonance making assignment of the metal oxidation state in high valent complexes unambiguous.

This work highlighted the properties of $[(\eta^4\text{-}\mathbf{8})]^{4-}$ metal complexes including their low redox potentials due to the strongly donating nature of the ligand and at least one nonplanar amide caused by a mismatch between the 6,5,6,5 chelate ring system cavity and the preferred bonding angles of the metal center.

Since this mismatch of cavity size and metal demands was observed to lead to hydrolytically unstable M^{III} complexes, the metal complexes of $H_4\mathbf{9}$, $H_4\mathbf{10}$, and $H_4\mathbf{11}$ which form 5,5,5,6 chelate ring systems were further explored. Deprotonation of $H_4\mathbf{9}$, $H_4\mathbf{10}$, and $H_4\mathbf{11}$ followed by metallation with $CoCl_2$ and air oxidation gave $Li[Co(\eta^4\text{-}\mathbf{9})]$, $Li[Co(\eta^4\text{-}\mathbf{10})]$, and $Li[Co(\eta^4\text{-}\mathbf{11})]$, respectively, which were found to be stable in water as were the $Cr^V{\equiv}O$ and $Mn^V{\equiv}O$ complexes.[74] Metathesis gave access Ph_4P^+, Et_4N^+, and/or Bu_4N^+ salts as well. Their UV spectra were not found to vary in coordinating and noncoordinating aprotic solvents, and their ^1H NMR spectra showed paramegnetically shifted signals which were minimally sensitive to the donor capacity of the solvent used. Both of these observations are consistent with formulation of these as square planar Co^{III} complexes in all aprotic solvents tested. Cyclic voltammetry shows that these can be oxidized to their neutral forms $[Co(\eta^4\text{-}\mathbf{9})]$, $[Co(\eta^4\text{-}\mathbf{10})]$, and $[Co(\eta^4\text{-}\mathbf{11})]$ with $Co(\eta^4\text{-}\#)/[Co(\eta^4\text{-}\#)]^-$ redox couples at 0.550, 0.385, and -0.010 V versus Fc^+/Fc, respectively. As expected, these decrease as the nature of the peripheral groups shifts from electron-withdrawing chloro- to electron donating methoxy- groups. The neutral forms were prepared by bulk electrolysis or chemical oxidation and isolated. X-ray crystallography of $[Ph_4P][Co(\eta^4\text{-}\mathbf{9})]$ and $[Co(\eta^4\text{-}\mathbf{9})]$ revealed both to be square planar complexes with the chelating N atoms deviating 0.02 and 0.05 Å from the mean plane, respectively, the Co atom is centered in the mean plane, and average Co—N bond lengths of 1.814 ± 4 and

1.825 ± 2 Å, respectively. In the neutral complex, the Co—N bonds to the phenylenediamine amido N atoms were ca 0.008 Å shorter than those to the diethylmalonamide amido N atoms. The bonds between the chlorine bearing and secondary aromatic carbons as well as those between the aromatic ring carbon and amido nitrogen atoms were observed to decrease in bond length by 0.037 and ~0.058 Å, respectively, upon oxidation of $[Co(\eta^4\text{-}\mathbf{9})]^-$ to give $Co(\eta^4\text{-}\mathbf{9})$. This was interpreted as evidence of greater contributions to the overall structure of the latter from resonance forms which place two electrons onto the metal center reducing its formal oxidation state. Consequently, the oxidation state of Co in the neutral forms was not assigned. EPR spectra of glasses of $Co(\eta^4\text{-}\mathbf{9})$, $Co(\eta^4\text{-}\mathbf{10})$, and $Co(\eta^4\text{-}\mathbf{11})$ prepared in anhydrous toluene were rhombic with g_1 = 2.558-2.571, g_2 = 2.168-2.187 (A_2 15-19 G), and g_3 at 2.017-2.024, indicating that the unpaired electron resides heavily at the metal center. Spin quantitation for $Co(\eta^4\text{-}\mathbf{9})$ against $Cu(ClO_4)_2$ indicated that the number of unpaired electrons per Co atom was 1 ± 0.1. Glasses of $Co(\eta^4\text{-}\mathbf{9})$, $Co(\eta^4\text{-}\mathbf{10})$, and $Co(\eta^4\text{-}\mathbf{11})$ prepared from H_2O saturated toluene were a visually identical deep blue to those prepared from anhydrous solvents and the EPR spectrum of a $Co(\eta^4\text{-}\mathbf{11})$ glass prepared from 45% enriched $H_2{}^{17}O$ saturated toluene was found to be identical to that prepared from anhydrous toluene indicating that trace water does not coordinate to the metal center of the complexes. $[Co(\eta^4\text{-}\mathbf{9})]$, was found to slowly oxidize water to give $H[Co(\eta^4\text{-}\mathbf{9})]$. This work further proves that $(\eta^4\text{-}\mathbf{9})^{4-}$, $(\eta^4\text{-}\mathbf{10})^{4-}$, and $(\eta^4\text{-}\mathbf{11})^{4-}$ are very resistant to oxidation as they are form stable complexes with high valent cobalt centers. Though the structural data provide evidence for some contribution of ligand reduction of the high valent metal center, the EPR spectra indicate that the oxidation equivalent resides

predominantly on metal center. Later work established that these complexes are best described as Co^{III} complexes with the oxidation equivalent residing on the phenylene diamine unit, are soluble in nonpolar solvents, can function as an oxidant, and have open coordination sites available for ligand binding.[67] Consequently, H_4**13** was developed to gain access to $[Co(\eta^4\text{-}\mathbf{13})]^-$ as it was anticipated to have greater solubility in hydrocarbon solvents.

A subsequent study found metallation of H_4**9**, H_4**10**, H_4**11**, and H_4**12** by deprotonation with *t*-BuLi followed by addition of $MnCl_2$, subsequent oxidation by air, oxidation by *t*-BuOOH, and cation metathesis with Et_4NCl afforded the $Mn^V{\equiv}O$ complexes $[Et_4N][Mn(O)(\eta^4\text{-}\mathbf{9})]$, $[Et_4N][Mn(O)(\eta^4\text{-}\mathbf{10})]$, $[Et_4N][Mn(O)(\eta^4\text{-}\mathbf{11})]$, and $[Et_4N][Mn(O)(\eta^4\text{-}\mathbf{12})]$. [75] These complexes were observed to be stable to hydrolysis. The oxo oxygen atoms of both the lithium salts (without metathesis) and Et_4N^+ salts of these were found to exchange with $H_2{}^{18}O$ upon dissolution in $H_2{}^{18}O$ or 1:10 $CH_3CN/H_2{}^{18}O$, respectively, facilitating assignment of the $Mn^V{\equiv}{}^{16}O$ and $Mn^V{\equiv}{}^{18}O$ IR stretching frequencies and Resonance Raman signatures upon excitation at 406.7 nM ($[Mn(O)(\eta^4\text{-}\mathbf{9})]^-$) or 488.0 nM ($[Mn(O)(\eta^4\text{-}\mathbf{10})]^-$, $[Mn(O)(\eta^4\text{-}\mathbf{11})]^-$, and $[Mn(O)(\eta^4\text{-}\mathbf{12})]^-$) with selective excitation studies confirming resonance enhancement of the assigned Mn-O intensity peaks. The resonance enhancement was attributed to the visible absorption arising from a $\pi \rightarrow \pi^*$ ($O_p \rightarrow Mn_d$) transition which was tentatively assigned as such due to its large ε value. The redox potentials of the first oxidation couple for $[Et_4N][Mn(O)(\eta^4\text{-}\mathbf{9})]$, $[Et_4N][Mn(O)(\eta^4\text{-}\mathbf{11})]$, and $[Et_4N][Mn(O)(\eta^4\text{-}\mathbf{12})]$ were found to be reversible. Hammett plots of these and the respective Hammett substituent σ^+ reference values generated from studies of the solvolysis of 2-chloro-2-phenylpropane

were found to be linear with $R = 0.99$ and $\rho/2 = -13.7$ indicating that this redox potential of these complexes correlates with the electronic properties of the substituents of the ligand aromatic ring. This was interpreted as evidence for contributions from the ligand oxidation to the one electron oxidized compounds as a result they it was recommended that these forms not be considered Mn^{VI} complexes. Unfortunately, these anionic Mn-oxo complexes were not observed to rapidly transfer oxygen atoms to substrates.[66-68] This low reactivity was again attributed to the strong donor capacity of the tetraanionic ligand system and the overall negative charge of the complexes which would result in very electron rich complexes. This was overcome by design of ligands incorporating an additional bidentate cation binding site as previously discussed. Observation of these stable high valent Mn complexes led to curiosity about the potential of the MAC ligand system to stabilize similar Fe complexes.[68]

Addition of tert-butyl isocyanide to $Li_2[FeCl(\eta^4\text{-}\mathbf{8})]$ in H_2O and subsequent oxidation with $(NH_4)_2Ce(NO_3)_6$ afforded $Fe(\eta^4\text{-}\mathbf{8})(CN^tBu)_2$ as a black solid.[76] X-ray crystallography showed the complex to be an axially distorted octahedron with Fe—N bond lengths of 1.910 Å and Fe—C bond lengths of 1.969 Å. The isocyanide C—N—C unit was observed to be linear and the C—N bond length of 1.14 Å was comparable to those of lower valent iron-isocyanide complexes in the literature formulated as C≡N so this formulation was deemed appropriate indicating that back bonding does not occur to a great extent. The zero-field Mössbauer spectrum displayed a doublet with a $|\Delta E_Q|$ of 3.38 mm s^{-1} that was observed to be temperature independent below 298 K and δ_{Fe} of -0.04 mm s^{-1} which lacked magnetic hyperfine interactions. The latter was interpreted as evidence for a complex with electronic spin either having an integer or zero

value. Assignment of a nonzero spin was made on evidence of a lack of significant back bonding to stabilize spin pairing. Since this is consistent with a d^4 iron atom in an octahedral crystal field and the value of δ_{Fe} was very low, Fe(η^4-**8**)(CN^tBu)$_2$ was proposed to be an $S = 1$ Fe^{IV} complex. A reversible $Fe^{IV/III}$ couple was observed at 450 mV vs Fc^+/Fc by cyclic voltammetry indicating that Fe(η^4-**8**)(CN^tBu)$_2$ is a potent oxidant that undergoes reduction and oxidation without decomposition, properties very useful for catalysis.

Studies of [FeCl(η^4-**8**)]$^{2-}$ and [FeCl(η^4-**8**)]$^-$ revealed the former to be a rare intermediate spin Fe^{III} complex while the latter was determined to be the only isolated high-spin Fe^{IV} coordination complex at the time. X-ray crystallography of [FeCl(η^4-**8**)]$^{2-}$ and [FeCl(η^4-**8**)]$^-$ showed both to be square pyramidal. X band EPR spectra in CH_3CN showed [FeCl(η^4-**8**)]$^{2-}$ to be a $S = 3/2$ system consistent with an intermediate spin d^5 metal ion in a square pyramidal crystal field. Mössbauer spectra of polycrystalline [Et_4N]$_2$[FeCl(η^4-**8**)] dispersed in adamantane in a 50-mT magnetic field at 4.2 K showed a signal at δ_{Fe} of 0.25 ± 3 mm s^{-1} with a $|\Delta E_Q|$ of -3.60 ± 0.05 mm s^{-1}. Mössbauer spectra at 50-mT of the polycrystalline compound and samples resulting from dissolution of [Et_4N]$_2$[FeCl(η^4-**8**)] in CH_3CN were identical indicating that the axial chloride ligand is retained in CH_3CN. The large $|\Delta E_Q|$ was observed to be temperature independent further supporting assignment of a very pure $S = 3/2$ spin state. Cyclic voltammograms of [FeCl(η^4-**8**)]$^{2-}$ in CH_2Cl_2 under N_2 showed a redox couple at -0.65 mV vs Fc/Fc^+.[71] Electrochemical oxidation of [Et_4N]$_2$[FeCl(η^4-**8**)] at a potential much lower than that of the ligand system gave [Et_4N][FeCl(η^4-**8**)]. A doublet at δ_{Fe} of -0.04 ± 0.02 mm s^{-1} with a

$|\Delta E_Q|$ of 0.89 ± 0.02 mm s^{-1} and was observed in the zero field Mössbauer spectra of both a frozen CH_3CN solution of $[Et_4N][FeCl(\eta^4\text{-}\mathbf{8})]$ at 4.2 K and polycrystalline $[Et_4N][FeCl(\eta^4\text{-}\mathbf{8})]$. The δ_{Fe} value is typical of **8** complexes that have been assigned the Fe^{IV} oxidation state. The isomer shift of -0.22 mm s^{-1} on oxidation of $[Et_4N]_2[FeCl(\eta^4\text{-}\mathbf{8})]$ to $[Et_4N][FeCl(\eta^4\text{-}\mathbf{8})]$ is consistent with an increase in Fe s electron density as a result of a decrease in d electron density for the latter. Six absorption lines characteristic were observed in the 0.1-1.0 T Mössbauer spectra of frozen CH_3CN and polycrystalline samples of $[Ph_4P][FeCl(\eta^4\text{-}\mathbf{8})]$ at 4.2 K indicative of a large $\langle S \rangle$ that has a value of nearly zero in a perpendicular plane to it and an electronic spin relaxation rate much less than the nuclear procession rate. From these observations and the absence of these lines in the zero-field spectrum it was determined that the complex has integer electronic spin. From the X-band EPR spectra it was determined that the complex was either $S = 1$ or $S = 2$. This is consistent with a high spin d^4 metal ion in a square pyramidal crystal field. However it was noted that estimations of the electronic structure of both the Fe^{III} and Fe^{IV} complexes based on simple ligand field models may not be appropriate. Analysis of quantitative EPR spectra and the magnetic field dependence of the Mössbauer spectra eliminated the possibility of $S = 1$ leaving $S = 2$ as the remaining assignment.

Unfortunately like other M^{III} 5,6,5,6 chelate ring system complexes, $[Fe(\eta^4\text{-}\mathbf{8})(Cl)]^{2-}$ was observed to be prone to slow hydrolysis of the N—M bonds in aqueous solvents.[71] Consequently, efforts were focused on the development of the iron complexes of ligand systems forming 5,5,5,6 chelate ring systems. Insertion of iron into H_4**11** gave $[FeH_2O(\eta^4\text{-}\mathbf{11})]^-$ the Mössbauer and EPR spectra of which were observed to be comparable to those of $[FeH_2O(\eta^4\text{-}\mathbf{9})]^-$. One electron oxidation of $[FeH_2O(\eta^4\text{-}\mathbf{11})]^-$ with

Ag^{I} salts or $Ce(NH_2)_4(NO_3)_6$ gave [$FeH_2O(\eta^4$-**11**)], the one electron reduction of which by $[Ru^{II}(NH_3)_6]Cl_2$ to return [$FeH_2O(\eta^4$-**11**)]$^-$ was monitored by UV/Vis spectroscopy. Cyclic voltammetry in H_2O revealed [$FeH_2O(\eta^4$-**11**)]$^-$ to have a redox couple at 0.46 V vs SSCE. Structural characterization of [$FeH_2O(\eta^4$-**11**)]$^-$ crystals grown from a *t*BuOH and Et_2O mixed solvent system indicated that the complex is square pyramidal with four almost planar N atoms that deviate 0.025 Å from the mean plane 0.362 Å above which the Fe atom resides with a 2.068 ± 0.003 Å bond to the H_2O oxygen atom. The H_2O H—O bond lengths were observed be unequal with that positioned the malonamide chelate ring having a length of 0.92 ± 0.06 Å and the other centered above the phenylenediamine ring chelate ring having a length of 0.72 ± 0.06 Å. The increased length of the former over the average Fe coordinated O—H bond length observed for other complexes of less than 0.8 Å was attributed to intermolecular hydrogen bonding with the amide oxygen of an adjacent [$FeH_2O(\eta^4$-**11**)]$^-$. Zero field Mössbauer spectra of [$FeH_2O(\eta^4$-**11**)]$^-$ crystals recorded at 4.2 K showed a doublet with δ_{Fe} and $|\Delta E_Q|$ values of 0.14 ± 0.02 and 4.19 ± 0.04 mm s^{-1}, respectively, which were noted to be comparable to 0.12 and 4.01 mm s^{-1}, those of [$FeH_2O(\eta^4$-**9**)]$^-$, a $S = 3/2$ complex. Zero field Mössbauer spectra of polycrystalline [$FeH_2O(\eta^4$-**11**)] recorded at 4.2 K showed a doublet with δ_{Fe} and $|\Delta E_Q|$ values of 0.14 ± 0.01 and 3.97 ± 0.02 mm s^{-1}, respectively. The similarity of the [$FeH_2O(\eta^4$-**11**)]$^-$ and [$FeH_2O(\eta^4$-**11**)] δ_{Fe} values were regarded as evidence that the additional oxidation equivalent of the latter resides on the ligand rather than the iron atom.

More extensive Mössbauer and magnetic studies as well as deeper analysis of the [$FeH_2O(\eta^4$-**11**)] crystal structure were conducted to confirm this. Fitting of a $S = 3/2$ spin

Hamiltonian equation to 4.2 K and 5.2 K 2.0, 4.0, 6.0, and 8.0 T Mössbauer spectra of crystalline $[FeH_2O(\eta^4\text{-}\mathbf{11})]^-$ gave parameters from which simulations matching these spectra could be generated lending further support to formulation of the anion as a $S = 3/2$ complex. Mössbauer spectra of $[FeH_2O(\eta^4\text{-}\mathbf{11})]$ crystals grown from *t*BuOH/Et_2O were observed to be similar to integer electronic spin complexes as were those of frozen aqueous solution samples of these crystals. Fitting of a $S = 1$ spin Hamiltonian equation to a set of frozen aqueous solution $[FeH_2O(\eta^4\text{-}\mathbf{11})]$ Mössbauer spectra resulted in a set of parameters from which simulations that fit to the experimental data well could be generated supporting formulation of the neutral form as a $S = 1$ complex. Analysis of 2-300 K magnetization data for $[FeH_2O(\eta^4\text{-}\mathbf{11})]$ crystals grown from CH_3CN/H_2O having slightly different crystal structure than those grown from *t*BuOH/Et_2O in fields up to 5.0 T revealed a nearly temperature independent μ_{eff} above 50 K and saturates at ≈3.0 μ_B which was interpreted as further evidence for a $S = 1$ system which should have a comparable spin only value of 2.83.[77] The $[FeH_2O(\eta^4\text{-}\mathbf{11})]^-$ and $[FeH_2O(\eta^4\text{-}\mathbf{11})]$ parameter sets obtained by fitting the data to the respective Hamiltonian equations were observed to be very similar. This was interpreted as further evidence for assignment of the Fe^{III} oxidation state for both and suggested that a ligand based radical couples with the $S = 1$ state of the latter antiferromagnetically. Careful inspection of the $[FeH_2O(\eta^4\text{-}\mathbf{11})]$ *t*BuOH/Et_2O crystal structure including the observation of C—N bonds of the phenylenediamine unit shorter than the typical 1.4 A suggestive of contributions from C=N bonding, uneven bond C—C bond distances between carbons of the phenylenediamine unit with those bonds between the carbons ortho and meta to those bearing the amines shorter, and the coplanar alignment of the carbon atoms of the

methoxy units with the aromatic ring. These all suggest that a semiquinone like resonance structure with donation from the lone pairs of the methoxy oxygen atoms heavily contributes to the overall structure of [$FeH_2O(\eta^4$-**11**)] indicating that the oxidation equivalent resides in a ligand based molecular orbital. Analysis of the crystal structure of [$FeCl(\eta^4$-**9**)]$^-$ revealed similar short C—N aromatic bond distances and unusual bond structure in the aromatic ring. Consequently, it was concluded that the [$FeCl(\eta^4$-**9**)]$^-$ iron atom is best considered to be intermediate between IV and III on the basis of this structural comparison as well as those of the Fe^{III} and Fe^{IV} complexes of [(η^4-**8**)]$^-$ and [(η^4-**9**)]$^-$ (exposure of [$Fe^{III}Cl(\eta^4$-**9**)]$^-$ to cyanide results in the generation of [$Fe^{IV}CN(\eta^4$-**9**)]$^-$, this work will be reviewed later in this text).[67,68,71] The potential for the chemistry of [$FeH_2O(\eta^4$-**11**)] to be altered by deprotonation to form the hydroxo or oxo complexes was noted as an area for future exploration.

Later DFT calculations of the anion and ligand radical cation forms [$Fe^{III}H_2O(\eta^4$-**11**)]$^-$ and [$Fe^{III}H_2O(\eta^4$-**11**$^{+\bullet}$)] support the assignment of a ligand based oxidation.[71] The spin density at the phenylenediamine carbon and nitrogen atoms of the former was calculated to be approximately zero while that at iron was calculated to be 2.84. The spin densities of the radical cation were found to be -0.14 for the amines of the phenylenediamine , -0.16 for the amine bonding carbons, +0.09 for the carbons ortho to that bearing the amine, and -0.15 for those meta to the amine. The spin density at iron was found to be 2.79. A 0.04 Å shortening of the phenelyenediamine N—C bonds was observed for the latter structure. Together these observations indicate that in this structure the radical is largely centered on the phenylenediamine unit. Theoretical Mössbauer parameters for this structure matched those experimentally observed for [$FeH_2O(\eta^4$-**11**)].

This ligand based oxidation is observed for complexes having weak axial donors and electron donating groups on the benzene ring. For these complexes, the highest occupied molecular orbital (HOMO) from which an electron is removed during oxidation has substantial ligand character.

Guidelines to aid the design of ligand systems capable of supporting metal centers in high valent states without undergoing oxidative degradation were formalized and disseminated.[67] These were generated from observations by other investigators and the work summarized above.[41,46,67] The body of literature drawn from includes studies by Margerum of Cu^{III} and Ni^{III} peptide complexes which were among the first to establish the N of deprotonated amides as strong σ donating atoms capable of stabilizing high valent metal ions, established that hydrogen atoms β to the metal center are a source of instability of complexes containing an oxidized metal chelated by deprotonated amido N atoms, and established that the process can be retarded by substituting β hydrogens with methyl groups.[41,42,46,78] Also included is insight gained from work on halogenated porphyrins showing that perfluorination leads to longer lived and more potent oxidation catalysts.[54]

The first work establishing ligand design guidelines also outlines an iterative design cycle for developing oxidation resistant ligand systems in which a complex is oxidized chemically or electrochemically until decomposition, the products of this decomposition are analyzed, and the ligand complement accountable for the decomposition is replaced by one that should resist it. Oxidation resistant complexes are defined as those that do not decompose on exposure to chemical and electrochemical oxidants such as > 2 V (SCE) in

oxidation resistant media of very low water content such as liquid SO_2. The following is a modified restatement of these

1) The ligand structure should not have hydrogen atoms on an atom β to the metal center if the α atom can form additional bonds to the β atom.
2) In five membered chelate rings, atoms γ to the metal center should not contain lone pairs capable of forming additional bonds to the β atom without requiring significant structural reorganization of the chelate ring (sp^2 to sp rehybridization rather than sp^3 to sp^2, for example) of the ligand system.
3) In five membered chelate rings, the α atom should not contain a pair of electrons capable of forming additional bonds to a cationic form of the β atom arising from heterolysis of the bond between the β and γ atoms.
4) If amido nitrogen atoms are to be employed as donors, the system should not be capable of isomerizing to give forms containing nonplanar amides.

The first three rules concern methods through which the ligand can be oxidized in a manner that allows the charge to reduce the metal center. The fourth recommends employment of the macrocyclic ligands to constrain ligand isomerization. Though other methods of preventing isomerization may exist, macrocyclic ligands also endow the final complex with additional stability due to the macrocycle effect. It is worthy of note that the design cycle proposed involves oxidation in solvents of very low water content. Thus the process does not assay for potential hydrolytic degradation pathways of the oxidized

complex. However, most of the high-valent forms of the complexes generated were observed to be hydrolytically stable.

Later work expands the scope of this process by removing limitations on the water content of the solvent.[68,79] Since the M^{III} complexes of 5,5,5,6 chelate ring system complexes were observed to be much more stable in aqueous solutions than 5,6,5,6 chelate ring system complexes, these studies implemented $[Fe(\eta^4\text{-}\mathbf{9})(H_2O)]^-$, the crystal structure of the Et_4N^+ salt of which showed it to be square pyramidal with an additional H_2O molecule in the lattice. Since the locations of the aqua ligand protons could not be established, they were inferred by analogy to the structure of $[Fe(\eta^4\text{-}\mathbf{11})(H_2O)]$ which was deemed appropriate since the Fe^{III} atoms of each are very similarly coordinated. X-band EPR spectra of $Et_4N[Fe(\eta^4\text{-}\mathbf{9})(H_2O)]$ in EtOH showed signals known to be indicative of a $S = 3/2$ system. Mössbauer spectra of both solid and ethanolic solutions of $[Fe(\eta^4\text{-}\mathbf{9})(H_2O)]^-$ at 4.2 K showed $\delta = 0.12$ mm s^{-1}, noted to be lower than but near the known $S = 3/2$ complex range of 0.14-0.35 mm s^{-1}. The $|\Delta E_Q|$ of the solid sample was observed to be 4.30 mm s^{-1} while that in EtOH was 4.00 mm s^{-1}, a difference which may arise due to exchange of the aqua ligand for EtOH in the latter.

Addition of *t*-butyl hydroperoxide (TBHP) to solutions of $Et_4N[Fe(\eta^4\text{-}\mathbf{9})(H_2O)]$ or $[Et_4N]_2[Fe(\eta^4\text{-}\mathbf{9})(Cl)]$ in nitrile solvents with C—H bonds on the carbon atom α to that of the nitrile unit was observed to result in a color change to deep blue while additions performed in $(CH_3)_3CCN$ did not. If base was added to the solution prior to or after addition of TBHP, the blue color persisted. In the absence of added base, the color faded to yellow-brown. Mössbauer spectra of the blue CH_3CN solutions showed a signal at $\delta = -0.15$ mm s^{-1} with a $|\Delta E_Q|$ of 4.4 mm s^{-1}. Evaporation of the solvent from the blue

solutions, dissolution in H_2O, and addition of Ph_4PCl gave a blue precipitate which gave an ESI mass spectrum having m/z and isotope ratio consistent with that expected to result from $Ph_4P[Fe(\eta^4\text{-}\mathbf{9})(CN)]$ and another product.

The identity of the $Ph_4P[Fe(\eta^4\text{-}\mathbf{9})(CN)]$ product was further verified by synthesis of it. Chemical oxidation of $[Fe(\eta^4\text{-}\mathbf{9})(Cl)]^{2-}$ with $(NH_4)_2Ce(NO_3)_6$ in CH_2Cl_2 to give $[Fe(\eta^4\text{-}\mathbf{9})(Cl)]^-$ followed by ligand exchange with CN^- in H_2O gave $[Fe(\eta^4\text{-}\mathbf{9})(CN)]^-$ which could also be precipitated by addition of Ph_4PCl. IR and ESI-MS analysis of isotopically labeled samples via both the synthetic and TBHP routes supported the assignment of the structure of both as $[Fe(\eta^4\text{-}\mathbf{9})(CN)]^-$. UV spectra of the synthetically prepared samples closely matched those of the blue precipitate from the TBHP reactions however the latter displayed lower extinction coefficients. The zero field Mössbauer spectra of synthetically prepared $[Fe(\eta^4\text{-}\mathbf{9})(CN)]^-$ at 4.2 K showed a doublet centered at $\delta = -0.18 \pm 0.02$ mm s^{-1} with $|\Delta E_Q|$ of 4.35 ± 0.02 mm s^{-1} consistent with a $S = 1$ Fe^{IV} complex. The Fe^{IV} oxidation state of this complex compared to the III/IV mixed valent state of $[Fe(\eta^4\text{-}\mathbf{9})(Cl)]^-$ was attributed to the strong σ donating ligand of the former indicating that strongly donating axial ligands localize the oxidation equivalent on the metal center by increasing the energy of the metal z^2 orbital above that of a molecular orbital of predominantly ligand character rendering the former the highest occupied molecular orbital from which oxidation occurs.[71] Deeper analysis of $[Fe(\eta^4\text{-}\mathbf{9})(CN)]^-$ Mössbauer spectra provided evidence that the Fe—C—N bond axis is orthogonal to the plane of the ligating N atoms. Analysis of these spectra using a spin Hamiltonian gave Mössbauer parameters which matched those calculated for a DFT geometry optimized structure of this complex.[71] This theoretical structure indicated a spin population of 2 on iron

consistent with that expected for an $S = 1$ Fe^{IV} complex. The $S = 2$ nature of $[FeCl(\eta^4\text{-}\mathbf{9})]^-$ versus the $S = 1$ nature of $[Fe(\eta^4\text{-}\mathbf{9})(CN)]^-$ was attributed to the effects of the donor capacity of the axial ligand on the spin state of the complex with stronger axial ligands such as cyanide raising the energy of the d_{z^2} orbital such that spin pairing in the d_{xy} orbital is energetically favored.[71]

In addition to $[Fe(\eta^4\text{-}\mathbf{9})(CN)]^-$, Mössbauer spectra of the Ph_4PCl precipitates of the base containing TBHP reaction solutions revealed the presence of a S = 5/2 Fe^{III} species which accounted for about 10% of the total iron present in the sample. Since TAML ligated Fe^{III} complexes have $S = 3/2$, this product was proposed to arise from non TAML Fe^{III} which could arise from degradation of the Fe^{III} TAML complex. Comparisons of the synthetically prepared $Ph_4P[Fe(\eta^4\text{-}\mathbf{9})(CN)]$ and TBHP reaction precipitate IR spectra revealed the latter to contain an additional strong band at 1723 cm^{-1}. Chromatographic separation of Ph_4PCl reaction precipitates was unsuccessful, however that of Et_4NCl precipitates resulted in isolation of $Et_4N[Fe(\eta^4\text{-}\mathbf{9})(CN)]$ in 90% yield and a diamagnetic product in 10% yield having a very strong IR band at 1723 cm^{-1}. ^1H NMR and ^{13}C NMR revealed signals consistent with a product having three exchangeable amido N—H protons and a =CH—CH_3 unit. FAB-MS indicated a molecular mass of 468 Da. In conjunction with these, high resolution mass analysis revealed the product to be the hydantoin ring containing product shown in Figure 5. The infrared spectrum of dimethylhydantoin showed a strong absorbance similar to the 1723 cm^{-1} band of this hydantoin ring containing product.

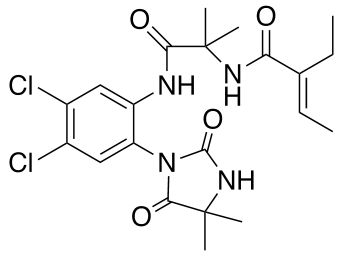

Figure 5. Hydantoin ring containing product formed on addition of TBHP to α C—H containing nitrile solvent solutions of $Et_4N[Fe(\eta^4\text{-}\mathbf{9})(H_2O)]$ or $[Et_4N]_2[Fe(\eta^4\text{-}\mathbf{9})(Cl)]$.

Studies of the ratio of the intensity of the 1723 cm^{-1} hydantoin IR signature to the amide absorptions of $Ph_4P[Fe(\eta^4\text{-}\mathbf{9})(CN)]$ of the Ph_4P precipitates formed by performing the TBHP reaction in various solvents revealed that the ratio decreased as the α C—H bond strength of the nitrile solvent decreased as would be expected if the two processes were in competition with each other. From this and observations of high valent complexes formed upon treatment of manganese TAML complexes with TBHP, a mechanism involving formation of a high valent iron species from $[Fe(\eta^4\text{-}\mathbf{9})(H_2O)]^-$ was postulated with this species then either abstracting H• from the solvent or undergoing decay to form the hydantoin ring containing product. The mechanism of this latter process was postulated to proceed via intramolecular H• abstraction from the methylene position of one of the geminal diethyl substituents of the malonamide residue of a high valent form of $[FeH_2O(\eta^4\text{-}\mathbf{9})]^-$. The resulting ligand centered radical is postulated to undergo rearrangement, ligand exchange, and hydrolysis to give the hydantoin ring containing product. This process was proposed to be very rapid as O_2 would be expected to intercept the ligand centered radical intermediate very quickly leading to other products.

Since the observed inactivation process was attributed to the geminal ethyl groups of the malonamide tail of $[FeH_2O(\eta^4\text{-}\mathbf{9})]^-$, these were replaced with methyl groups to give $[FeH_2O(\eta^4\text{-}\mathbf{14})]^-$, the analogous C—H bonds of which are ca 3 kcal mol^{-1} stronger since the less stable primary radical is formed upon hydrogen abstraction. Comparative studies of $[FeH_2O(\eta^4\text{-}\mathbf{9})]^-$ and $[FeH_2O(\eta^4\text{-}\mathbf{14})]^-$ catalysis of the bleaching of pinacyanol chloride (PC), an organic dye the structure of which is shown in Figure 6, by H_2O_2 in carbonate buffered pH 10 were undertaken.[80] An aliquot of H_2O_2 was added to a solutions containing $[FeH_2O(\eta^4\text{-}\mathbf{9})]^-$ or $FeH_2O(\eta^4\text{-}\mathbf{14})]^-$ and PC. When the UV absorbance of the solution at 600 nM reached 0, an additional aliquot of dye was added. The $[FeH_2O(\eta^4\text{-}\mathbf{14})]^-$ containing solutions were observed to bleach more aliquots of dye than the $[FeH_2O(\eta^4\text{-}\mathbf{9})]^-$ solutions. The first bleaching cycle was equally rapid for both sets of solutions. However, sequential $[FeH_2O(\eta^4\text{-}\mathbf{9})]^-$ cycles were increasingly slower while the rates of sequential $[FeH_2O(\eta^4\text{-}\mathbf{14})]^-$ cycles remained rapid. In 4 bleaching cycles, the rate displayed by $[FeH_2O(\eta^4\text{-}\mathbf{9})]^-$ solutions were only slightly greater than the background bleaching rate while $[FeH_2O(\eta^4\text{-}\mathbf{14})]^-$ solutions retained their ability to rapidly bleach over 7 cycles. More cycles were observed for $[FeH_2O(\eta^4\text{-}\mathbf{14})]^-$ at all of the tested neutral to basic pH levels. Addition of an excess of H_2O_2 to dye free, high concentration solutions of $[FeH_2O(\eta^4\text{-}\mathbf{9})]^-$ or $[FeH_2O(\eta^4\text{-}\mathbf{14})]^-$ resulted in an increase in absorbance at 454 nM. For $[FeH_2O(\eta^4\text{-}\mathbf{9})]^-$ solutions, this absorbance was observed to return to baseline in 200 seconds while $[FeH_2O(\eta^4\text{-}\mathbf{14})]^-$ solutions did not fully return to baseline after 2 hours. Together, these results were interpreted as evidence of a greater rate of

inactivation of $[FeH_2O(\eta^4\text{-}\mathbf{9})]^-$ than $[FeH_2O(\eta^4\text{-}\mathbf{14})]^-$, which is consistent with conclusions reached from the TBHP reactions.

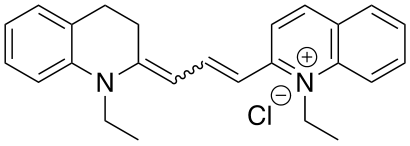

Figure 6. Structure of the Pinacyanol chloride dye.

The only observed inorganic product of TBHP reactions employing $[FeH_2O(\eta^4\text{-}\mathbf{14})]^-$ was $[FeH_2O(\eta^4\text{-}\mathbf{14})]^-$. However, addition of TBHP to $[FeH_2O(\eta^4\text{-}\mathbf{14})]^-$ solutions in CH_2Cl_2 results in degradation products having an IR absorption at 1721 cm^{-1} consistent with formation of a hydantoin ring containing product indicating that the substitution retards hydantoin formation but does not completely block it. Consequently, **15** and its iron complexes were designed and synthesized for evaluation with the expectation that placing fluorine atoms at the methylene position of the malonamide residue would so enhance the oxidation resistance of the ligand structure as to shut down this degradation process.[27]

Since Mn^V-oxo TAML complexes can be synthesized from TBHP and Mn^{III} TAML complexes, the reactive intermediate in the TBHP reactions was proposed to be an Fe^V-oxo complex.[68] It was postulated that the enhanced reactivity of this Fe^V-Oxo over the Mn and Cr analogues derives from the presence of a d electron in an orbital having Fe—O bond π^* character which endows the oxo oxygen atom with radical character while the d electrons of the Mn and Cr analogues reside in nonbonding orbitals in the ligand plane. Consequently, studies were undertaken to identify this intermediate. In the presence of

the trace potential ligands H_2O, pyridine, and benzoic acid, addition of 1 equivalent of *m*-chloroperbenzoic acid to $[PPh_4][Fe^{III}H_2O(\eta^4\text{-}\mathbf{16})]$ in -60 °C *n*-butyronitrile or -40 °C acetonitrile was observed to give the same green species after 15 minutes, regardless of the identity of the trace ligands present.[81] ESI-MS showed this species to have m/z of 442.2 the isotopic distribution pattern expected for $[Fe^{V}(O)(\eta^4\text{-}\mathbf{16})]^-$. In the presence of $H_2{}^{18}O$, the same procedure with a 30 minute reaction time gave the peak expected to derive from $[Fe^{V}(^{18}O)(\eta^4\text{-}\mathbf{16})]^-$. The major signal in the 28 K EPR spectrum of a glass sample of the green complex generated in n-butryonitrile at -60 °C showed a $S = 1/2$ species having *g* values 1.99, 1.97, and 1.74. Spectral simulations agreed with this formulation. The major feature of the 4.2 K Mössbauer spectrum at 45 mT was observed at a δ value of -0.42±0.03 mm s^{-1}, significantly lower than -0.18±0.02 mm s^{-1}, the lowest observed Fe-TAML δ value at the time found for $S = 1$ $[Fe^{IV}CN(\eta^4\text{-}\mathbf{9})]^-$ under similar experimental conditions.

Since ESI-MS data were consistent with $[Fe^{V}(O)(\eta^4\text{-}\mathbf{16})]^-$, the major EPR signal corresponded to an S = 1/2 complex, and the 4.2 K Mössbauer δ value was so low, the green complex was formulated as low-spin d^3 $[Fe^{V}(O)(\eta^4\text{-}\mathbf{16})]^-$. Fitting of a $S = 1/2$ Hamiltonian to 4.2-140 K, variable magnetic field Mössbauer data gave parameters that were used to generate simulations which fit the Mössbauer spectra well. Examination of the fine structure region of the X-ray absorption spectra of $[Fe^{III}(\eta^4\text{-}\mathbf{16})]^-$ and $[Fe^{V}(O)(\eta^4\text{-}\mathbf{16})]^-$ as well as simulations of the latter determined that and $[Fe^{V}(O)(\eta^4\text{-}\mathbf{16})]^-$ contained a novel 0.7 O scatterer located 1.58 Å from Fe, assigned as the oxygen atom of the Fe—O. DFT calculations indicated that the S = 3/2 ground state was preferred for $[Fe^{V}(O)(\eta^4\text{-}\mathbf{16})]^-$ and geometry optimization resulted in a predicted Fe—O bond length of 1.60 Å

consistent with that found by X-ray absorption. DFT calculations estimate Mössbauer δ values for $[Fe^{IV}(O)(\eta^4\text{-}\mathbf{16}^{+\bullet})]^-$ $[Fe^{V}(O)(\eta^4\text{-}\mathbf{16})]^-$ to be -0.15 and -0.39 mm s^{-1}, respectively, lending further support for the latter formulation. This method was able to closely reproduce experimental Mössbauer δ values for other TAML complexes. It was concluded that the strong σ donation of the TAML macrocycle raises the energy of the metal orbital from which oxidation occurs such that the energetically preferred location of the oxidation equivalent is the metal center rather than the ligand.

With the structure of $[Fe^{V}(O)(\eta^4\text{-}\mathbf{16})]^-$ well defined, the first iron(V)-oxo complex to be fully authenticated, the reactivity was examined. It was observed to rapidly oxidize Ph_3P to Ph_3PO quantitatively. Gas chromatography-mass spectrometry analysis of reaction solutions with 0.2% $H_2{}^{18}O$ by volume showed Ph_3PO^{18} formation. Oxidations of other substrates were also observed and in some cases did not result in $[Fe^{III}(\eta^4\text{-}\mathbf{16})]^-$ but instead diiron(IV) dimers and other forms of lower valency than V were observed. Future studies of the mechanism of stoichiometric oxidations by $[Fe^{V}(O)(\eta^4\text{-}\mathbf{16})]^-$ were planned. However, Fe-TAML catalysis of substrate oxidations is best examined using the tools of kinetics.

Conclusion

With this comprehensive background of the large body of coordination chemistry of PAC, MAC and TAML systems, I will present my thesis work which largely concerns expanding the fundamentals of the coordination and catalytic chemistry of the TAML systems. My work is focused on iron, because now that the group has mastered the difficult to enter iron coordination chemistry, the value of iron as the principal catalytic

element of enzymatic oxidations and the safety arising from its biochemical ubiquity means that, all other things being equal, it eclipses all other transition metals in its importance for commercially useful catalysis. This work is largely comprised of an expansive study of the kinetics of Fe-TAML catalyzed oxidation of the azo dye Orange II in water at pH 7, conditions preferred for water treatment. Drs Collins, Ryabov, and I hoped that these studies, which include both collaborative development of a method for measurements of the rate of catalyst inactivation under these conditions and its use, would shed light on the mechanism of catalyst inactivation, particularly that of Li[Fe^{III}(η^4-**16**)] which is not be capable of undergoing the aforementioned hydantoin ring formation. These studies have illuminated novel structure-activity relationships and provide evidence for an unanticipated mechanism of catalyst inactivation that has guided the design of a new class of catalysts that Dr. Collins, Genoa Warner, and I are in the process of patenting, the earliest members of which have already begun to display a better balance of cost and technical performances than TAMLs.

References

(1) Zalasiewicz*, J.; Williams, M.; Steffen, W.; Crutzen, P. *Environmental Science & Technology* **2010**, *44*, 2228.
(2) Schmidt, W. A. *Journal of Chemical Education* **1928**, *5*, 1224.
(3) Ternes, T. A.; Meisenheimer, M.; McDowell, D.; Sacher, F.; Brauch, H.-J.; Haist-Gulde, B.; Preuss, G.; Wilme, U.; Zulei-Seibert, N. *Environmental Science & Technology* **2002**, *36*, 3855.
(4) Luo, Y.; Guo, W.; Ngo, H. H.; Nghiem, L. D.; Hai, F. I.; Zhang, J.; Liang, S.; Wang, X. C. *Science of The Total Environment* **2014**, *473–474*, 619.
(5) Nam, S.-W.; Jo, B.-I.; Yoon, Y.; Zoh, K.-D. *Chemosphere* **2014**, *95*, 156.
(6) Westerhoff, P.; Yoon, Y.; Snyder, S.; Wert, E. *Environmental Science & Technology* **2005**, *39*, 6649.
(7) Snyder, W. L.; Lei, H.; Westerhoff, P.; Yoon, T. *Removal of EDCs and pharmaceuticals in drinking and reuse treatment processes*, Awwa Research Foundation, 2007.
(8) Joss, A.; Siegrist, H.; Ternes, T. A. *Water Sci Technol* **2008**, *57*, 251.
(9) Escher, B. I.; Fenner, K. *Environmental Science & Technology* **2011**, *45*, 3835.
(10) Schwarzenbach, R. P.; Escher, B. I.; Fenner, K.; Hofstetter, T. B.; Johnson, C. A.; von Gunten, U.; Wehrli, B. *Science* **2006**, *313*, 1072.
(11) Rice, J.; Westerhoff, P. *Environmental Science & Technology* **2015**, *49*, 982.
(12) *Pesticides*.
(13) Muir, D. C. G.; Howard, P. H. *Environmental Science & Technology* **2006**, *40*, 7157.
(14) Voutchkova, A. M.; Kostal, J.; Steinfeld, J. B.; Emerson, J. W.; Brooks, B. W.; Anastas, P.; Zimmerman, J. B. *Green Chemistry* **2011**, *13*, 2373.
(15) Schenker, S.; Scheringer, M.; Hungerbühler, K. *Environmental Science & Technology* **2014**, *48*, 5017.
(16) Boxall, A. B. A.; Sinclair, C. J.; Fenner, K.; Kolpin, D.; Maund, S. J. *Environmental Science & Technology* **2004**, *38*, 368A.
(17) Kidd, K. A.; Blanchfield, P. J.; Mills, K. H.; Palace, V. P.; Evans, R. E.; Lazorchak, J. M.; Flick, R. W. *Proceedings of the National Academy of Sciences* **2007**, *104*, 8897.
(18) Phillips, P. J.; Chalmers, A. T.; Gray, J. L.; Kolpin, D. W.; Foreman, W. T.; Wall, G. R. *Environmental Science & Technology* **2012**, *46*, 5336.
(19) Rosario-Ortiz, F.; Rose, J.; Speight, V.; Gunten, U. v.; Schnoor, J. *Science* **2016**, *351*, 912.
(20) Richardson, S. D. *Analytical Chemistry* **2009**, *81*, 4645.
(21) *Water Reuse: Potential for Expanding the Nation's Water Supply Through Reuse of Municipal Wastewater*; The National Academies Press, 2012.
(22) *Centers for Disease Control and Prevention. Fourth Report on Human Exposure to Environmental Chemicals*, 2009.
(23) Coetsier, C. M.; Spinelli, S.; Lin, L.; Roig, B.; Touraud, E. *Environment International* **2009**, *35*, 787.
(24) ; Control, D. o. H. a. E., Ed. South Carolina, 2013; Vol. 37.

(25) Tang, L. L.; Denardo, M. A.; Gayathri, C.; Gil, R. R.; Kanda, R.; Collins, T. J. *Environmental Science & Technology* **2016**, *Submitted*.
(26) DeNardo, M. A.; Mills, M. R.; Ryabov, A. D.; Collins, T. J. *Journal of the American Chemical Society* **2016**.
(27) Collins, T. J. *Accounts of Chemical Research* **2002**, *35*, 782.
(28) Gupta, S. S.; Stadler, M.; Noser, C. A.; Ghosh, A.; Steinhoff, B.; Lenoir, D.; Horwitz, C. P.; Schramm, K.-W.; Collins, T. J. *Science* **2002**, *296*, 326.
(29) Kundu, S.; Chanda, A.; Thompson, J. V. K.; Diabes, G.; Khetan, S. K.; Ryabov, A. D.; Collins, T. J. *Catalysis Science & Technology* **2015**, *5*, 1775.
(30) Kundu, S.; Chanda, A.; Khetan, S. K.; Ryabov, A. D.; Collins, T. J. *Environmental Science & Technology* **2013**, *47*, 5319.
(31) Shen, L. Q.; Beach, E. S.; Xiang, Y.; Tshudy, D. J.; Khanina, N.; Horwitz, C. P.; Bier, M. E.; Collins, T. J. *Environmental Science & Technology* **2011**, *45*, 7882.
(32) Beach, E. S.; Malecky, R. T.; Gil, R. R.; Horwitz, C. P.; Collins, T. J. *Catalysis Science & Technology* **2011**, *1*, 437.
(33) Beach, E. S.; Duran, J. L.; Horwitz, C. P.; Collins, T. J. *Industrial & Engineering Chemistry Research* **2009**, *48*, 7072.
(34) Chanda, A.; Khetan, S. K.; Banerjee, D.; Ghosh, A.; Collins, T. J. *Journal of the American Chemical Society* **2006**, *128*, 12058.
(35) Banerjee, D.; Markley, A. L.; Yano, T.; Ghosh, A.; Berget, P. B.; Minkley, E. G.; Khetan, S. K.; Collins, T. J. *Angewandte Chemie International Edition* **2006**, *45*, 3974.
(36) Mills, M. R.; Arias-Salazar, K.; Baynes, A.; Shen, L. Q.; Churchley, J.; Beresford, N.; Gayathri, C.; Gil, R. R.; Kanda, R.; Jobling, S.; Collins, T. J. *Scientific Reports* **2015**, *5*, 10511.
(37) Bour, J. J.; Steggerda, J. J. *Chemical Communications (London)* **1967**, 85b.
(38) Steggerda, J. J.; Bour, J. J.; Birker, P. J. M. W. L. *Inorganic Chemistry* **1971**, *10*, 1202.
(39) Anson, F. C.; Christie, J. A.; Collins, T. J.; Coots, R. J.; Furutani, T. T.; Gipson, S. L.; Keech, J. T.; Krafft, T. E.; Santarsiero, B. D.; Spies, G. H. *Journal of the American Chemical Society* **1984**, *106*, 4460.
(40) Sigel, H.; Martin, R. B. *Chemical Reviews* **1982**, *82*, 385.
(41) Margerum, D. W. *Pure Appl. Chem.* **1983**, *55*, 23.
(42) Diaddario, L. L.; Robinson, W. R.; Margerum, D. W. *Inorganic Chemistry* **1983**, *22*, 1021.
(43) Kimura, E.; Sakonaka, A.; Machida, R.; Kodama, M. *Journal of the American Chemical Society* **1982**, *104*, 4255.
(44) Buttafava, A.; Fabbrizzi, L.; Perotti, A.; Seghi, B. *Journal of the Chemical Society, Chemical Communications* **1982**, 1166.
(45) Fabbrizzi, L.; Perotti, A.; Poggi, A. *Inorganic Chemistry* **1983**, *22*, 1411.
(46) Bossu, F. P.; Chellappa, K. L.; Margerum, D. W. *Journal of the American Chemical Society* **1977**, *99*, 2195.
(47) Collins, T. J.; Santarsiero, B. D.; Spies, G. H. *Journal of the Chemical Society, Chemical Communications* **1983**, 681.
(48) Christie, J. A.; Collins, T. J.; Krafft, T. E.; Santarsiero, B. D.; Spies, G. H. *Journal of the Chemical Society, Chemical Communications* **1984**, 198.

(49) Anson, F. C.; Collins, T. J.; Coots, R. J.; Gipson, S. L.; Krafft, T. E.; Santarsiero, B. D.; Spies, G. H. *Inorganic Chemistry* **1987**, *26*, 1161.
(50) Anson, F. C.; Collins, T. J.; Gipson, S. L.; Keech, J. T.; Krafft, T. E. *Inorganic Chemistry* **1987**, *26*, 1157.
(51) Anson, F. C.; Collins, T. J.; Coots, R. J.; Gipson, S. L.; Richmond, T. G. *Journal of the American Chemical Society* **1984**, *106*, 5037.
(52) Collins, T. J.; Richmond, T. G.; Santarsiero, B. D.; Treco, B. G. R. T. *Journal of the American Chemical Society* **1986**, *108*, 2088.
(53) Barner, C. J.; Collins, T. J.; Mapes, B. E.; Santarsiero, B. D. *Inorganic Chemistry* **1986**, *25*, 4322.
(54) Collins, T. J.; Coots, R. J.; Furutani, T. T.; Keech, J. T.; Peake, G. T.; Santarsiero, B. D. *Journal of the American Chemical Society* **1986**, *108*, 5333.
(55) Collins, T. J.; Lai, T.; Peake, G. T. *Inorganic Chemistry* **1987**, *26*, 1674.
(56) Collins, T. J.; Workman, J. M. *Angewandte Chemie International Edition* **1989**, *28*, 912.
(57) Collins, T. J.; Keech, J. T. *Journal of the American Chemical Society* **1988**, *110*, 1162.
(58) Anson, F. C.; Collins, T. J.; Richmond, T. G.; Santarsiero, B. D.; Toth, J. E.; Treco, B. G. R. T. *Journal of the American Chemical Society* **1987**, *109*, 2974.
(59) Collins, T. J.; Ozaki, S.; Richmond, T. G. *Journal of the Chemical Society, Chemical Communications* **1987**, 803.
(60) Ozaki, S.; Mimura, H.; Yasuhara, N.; Masui, M.; Yamagata, Y.; Tomita, K.; Collins, T. J. *Journal of the Chemical Society, Perkin Transactions 2* **1990**, 353.
(61) Brewer, J. C.; Collins, T. J.; Smith, M. R.; Santarsiero, B. D. *Journal of the American Chemical Society* **1988**, *110*, 423.
(62) Collins, T. J.; Gordon-Wylie, S. W. *Journal of the American Chemical Society* **1989**, *111*, 4511.
(63) Collins, T. J.; Powell, R. D.; Slebodnick, C.; Uffelman, E. S. *Journal of the American Chemical Society* **1990**, *112*, 899.
(64) Collins, T. J.; Uffelman, E. S. *Angewandte Chemie International Edition in English* **1989**, *28*, 1509.
(65) Collins, T. J.; Slebodnick, C.; Uffelman, E. S. *Inorganic Chemistry* **1990**, *29*, 3433.
(66) Miller, C. G.; Gordon-Wylie, S. W.; Horwitz, C. P.; Strazisar, S. A.; Peraino, D. K.; Clark, G. R.; Weintraub, S. T.; Collins, T. J. *Journal of the American Chemical Society* **1998**, *120*, 11540.
(67) Collins, T. J. *Accounts of Chemical Research* **1994**, *27*, 279.
(68) Bartos, M. J.; Gordon-Wylie, S. W.; Fox, B. G.; James Wright, L.; Weintraub, S. T.; Kauffmann, K. E.; Münck, E.; Kostka, K. L.; Uffelman, E. S.; Rickard, C. E. F.; Noon, K. R.; Collins, T. J. *Coordination Chemistry Reviews* **1998**, *174*, 361.
(69) Terrence J. Collins, P. C.
(70) Collins, T. J.; Kostka, K. L.; Munck, E.; Uffelman, E. S. *Journal of the American Chemical Society* **1990**, *112*, 5637.
(71) Chanda, A.; Popescu, D.-L.; de Oliveira, F. T.; Bominaar, E. L.; Ryabov, A. D.; Münck, E.; Collins, T. J. *Journal of Inorganic Biochemistry* **2006**, *100*, 606.

(72) Collins, T. J.; Nichols, T. R.; Uffelman, E. S. *Journal of the American Chemical Society* **1991**, *113*, 4708.
(73) Collins, T. J.; Kostka, K. L.; Uffelman, E. S.; Weinberger, T. L. *Inorganic Chemistry* **1991**, *30*, 4204.
(74) Collins, T. J.; Powell, R. D.; Slebodnick, C.; Uffelman, E. S. *Journal of the American Chemical Society* **1991**, *113*, 8419.
(75) Workman, J. M.; Powell, R. D.; Procyk, A. D.; Collins, T. J.; Bocian, D. F. *Inorganic Chemistry* **1992**, *31*, 1548.
(76) Collins, T. J.; Fox, B. G.; Hu, Z. G.; Kostka, K. L.; Munck, E.; Rickard, C. E. F.; Wright, L. J. *Journal of the American Chemical Society* **1992**, *114*, 8724.
(77) Kauffmann, K. E.; Bartos, M.; Kidwell, C.; Gordon-Wylie, S. W.; Collins, T. J.; Clark, G. C.; Weintraub, S. T.; Münck, E. *Journal of Inorganic Biochemistry* **1995**, *59*, 416.
(78) Chen, H. L.; Ellis, P. E.; Wijesekera, T.; Hagan, T. E.; Groh, S. E.; Lyons, J. E.; Ridge, D. P. *Journal of the American Chemical Society* **1994**, *116*, 1086.
(79) Collins, T. J.; Bartos, M. J.; Gordon-Wylie, S. W.; Fox, B. G.; Kauffmann, K. E.; Münck, E.; Rickard, C. E. F.; Weintraub, S. T.; Uffelman, E. S.; Wright, L. J. *Journal of Inorganic Biochemistry* **1995**, *59*, 318.
(80) Horwitz, C. P.; Fooksman, D. R.; Vuocolo, L. D.; Gordon-Wylie, S. W.; Cox, N. J.; Collins, T. J. *Journal of the American Chemical Society* **1998**, *120*, 4867.
(81) de Oliveira, F. T.; Chanda, A.; Banerjee, D.; Shan, X.; Mondal, S.; Que, L.; Bominaar, E. L.; Münck, E.; Collins, T. J. *Science* **2007**, *315*, 835.

Chapter 2

Comparative Evaluation of the Technical and Environmental Performances of TAML Activators and Assessment of the Potential of the Nitrile Group to Advance TAML Chemistry

Introduction

The mechanistic chemistry of TAML activator science is immensely rich in details as the Collins Group has for almost two decades been finding ways to isolate and quantify mechanistically the many individual elementary reactions that impact the catalytic performance under operating conditions. TAML activator catalysis is exquisitely pH dependent and, as my work has shown, subject to large quantifiable changes in reactivity based upon the different generational structures and the substituents appended to these. I will begin this chapter with a review of the mechanistic techniques and understanding that the Collins Group has assembled over the years. Then I will show, by studying very carefully a range of TAML activators in a common reaction, the comparative technical performances of the individual catalysts. I prepared a number of the catalysts discussed in this and the following chapter myself and obtained others from the Collins Group stock generated by previous students and current group members. I am most grateful to colleagues who prepared these samples. As the reader will learn, the comparative technical performance of TAML activators is determined by the relative rates constants for individual reactions that are key steps in the catalytic cycle. We call the most important of these "Technical Performance Parameters".[1] With this having been noted, the next section presents my interpretation of the published understanding of the mechanisms of action of TAML activators which is the springboard that I used for the described studies. It is my hope that this comprehensive mini-review will be of use to new students undertaking mechanistic work.

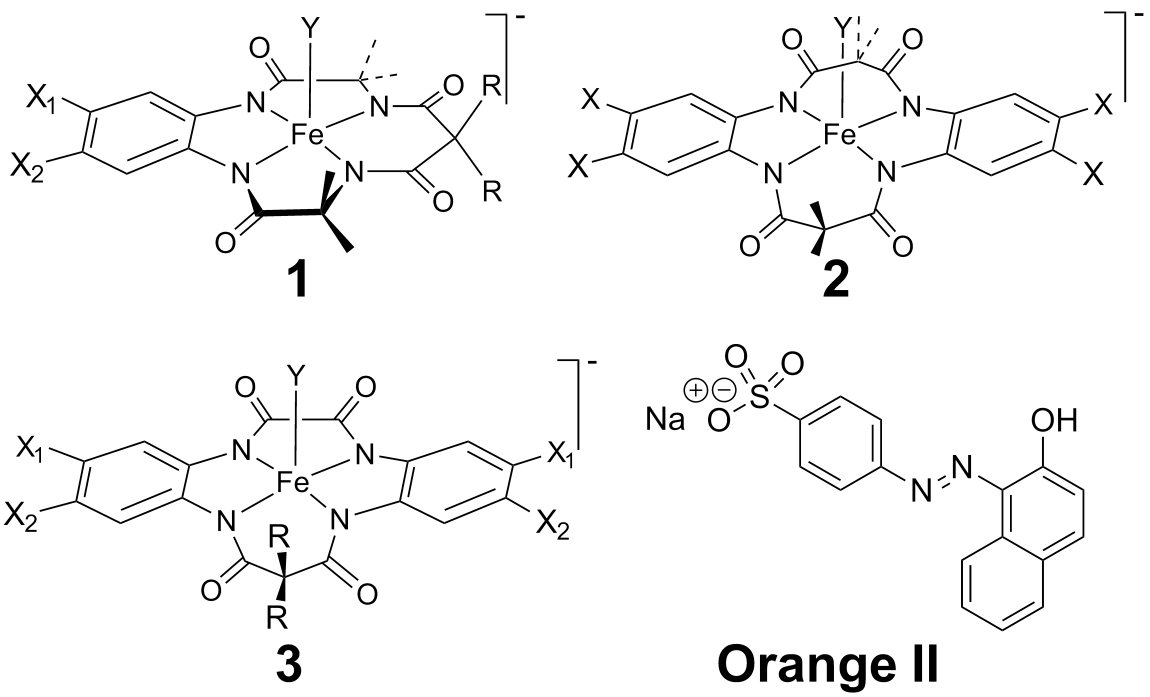

Figure 1. Structures of the catalysts referred to in Chapter 2 and the azo dye model substrate Orange II. **1a**: X_1=X_2=H, R=CH_3; **1b**: X_1=X_2=H, R=F; **1c**: X_1=NO_2, X_2=H, R=F; **1d**: X_1=X_2=Cl, R=F; **2a**: X=H; **2b**: X=Cl; **2c**: X=OCH_3; **3a**: X_1=X_2=H, R=CH_3; **3b**: X_1=X_2=H, R=F; **3c**: X_1=X_2=Cl, R=CH_3; **3d**: X_1=CN, X_2=H, R=CH_3; **3e**: X_1=NO_2, X_2=H, R=CH_3; **3f**: X_1=CO_2^-, X_2=H, R=CH_3.

TAML activators (Figure 1) have been advanced for water purification for which high performance under the ambient conditions of neutral pH and 25 °C are desirable. Activators of the **1** series have been commercialized and are being used in many applications. The recently synthesized **3** has been shown to outperform **1** in the oxidation of the azo dye model substrate Orange II.[2,3] This work concerns an assessment of the pH 7 relative technical, environmental, and health performances of **1a**, **1b**, **1c**, **3a**, **3b**, **3c**, **3d**, and **3e**.

Assessing TAML Technical Performance by Kinetics

To date, all TAML catalysts studied in the Collins Group have been found to obey the same stoichiometric mechanism in which the resting ferric catalyst (Fe^{III}) reacts with the primary oxidant (k_I) to form the catalytically active species (Ac), which then either oxidizes a substrate (k_{II}) to regenerate the resting catalyst or undergoes inactivation (k_i). By contrasting the values of catalyst specific pH dependent k_I, k_{II}, and k_i, assessments of the relative technical performance of TAML activators can be made. This chapter concerns the first two— the latter is the subject of Chapter 3.

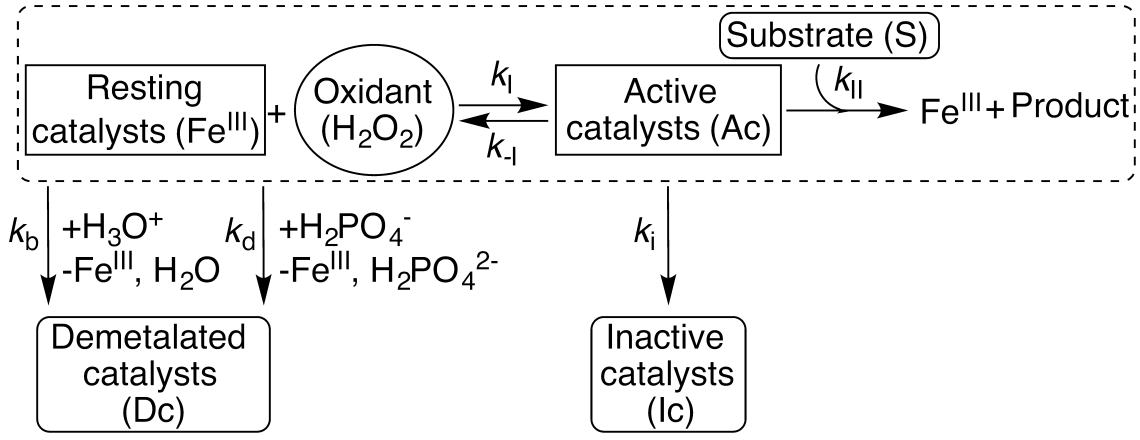

Figure 2. Elementary steps considered in TAML processes.

$$v = \frac{k_I k_{II}[H_2O_2][S]}{k_{-I} + k_I[H_2O_2] + k_{II}[S]} Fe_{Tot} \quad (1)$$

A comparison of the technical performance of TAML activators considering k_I and k_{II} alone requires that the rate constants be available. A few methods of obtaining them have been devised based on eq 1, a mathematical representation of the sequence of

events shown in the box of Figure 2 which has been found to accurately model the dependence of the initial rate of substrate oxidation, v, on the concentration of hydrogen peroxide, $[H_2O_2]$, substrate, [S], and catalyst, Fe_{Tot}, under steady state conditions with Fe_{Tot}=[Rc]+[Ac] applied to the mass balance of the catalyst.[4] The value of the rate constant for the reverse of catalyst activation is considered to be negligible ($k_{-I} \rightarrow 0$).

The simplest and most accurate way of obtaining k_I and k_{II} from a small data set involves measuring each independently. In theory, this can be achieved under any one set of conditions by choosing the pH, identity and concentration of a substrate, and concentration of H_2O_2 such that either $k_I[H_2O_2] << k_{II}[S]$ and eq 1 simplifies to eq 2 or $k_I[H_2O_2] >> k_{II}[S]$ and eq 1 simplifies to eq 3.

$$v = k_I[H_2O_2]Fe_{Tot} \quad (2)$$

$$v = k_{II}[S]Fe_{Tot} \quad (3)$$

For most combinations of oxidant, substrate, and catalyst under most conditions, $k_I << k_{II}$ and catalyst activation is rate determining. Consequently, in practice the former case is often easily attainable by selecting an appropriate $[H_2O_2]$ and [S] while the latter may not be. The bleaching of the most common substrate employed in evaluation of the performance of TAML activators, Orange II, displays large k_{II} values due to the relative ease with which it is oxidized by the Ac of TAML catalysts. As a result, measurements of k_I in the oxidation of Orange II are most easily conducted under conditions where eq 2 applies.

Here, determination of k_I is accomplished by measuring v over a low tenfold range of $[H_2O_2]$ at a high fixed [S] to ensure a linear dependence is observed as shown in Figure 1A which indicates that eq 2 applies. The slope of the line of best fit to this dependence is k_I*Fe_{Tot} provided a zero-order dependence of v on [S] at a $[H_2O_2]$ within this range is also observed as shown in Figure 3B.

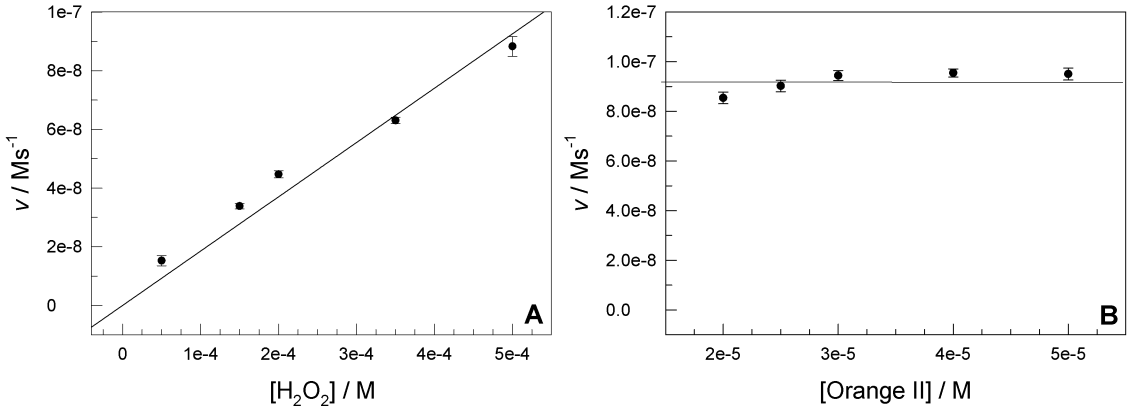

Figure 3. A: Plot showing the initial rates of the **3d**-catalyzed bleaching of Orange II by H_2O_2 as a function of $[H_2O_2]$ at pH 7 with [**3d**] = 1×10^{-7} M and [Orange II]= 2.5×10^{-5} M in 0.01 M phosphate, 25 °C. **B**: Plot showing the initial rates of the **3d**-catalyzed bleaching of Orange II by H_2O_2 as a function of [Orange II] at pH 7 with [**3d**] = 1×10^{-7} M and $[H_2O_2]$= 2.5×10^{-5} M in 0.01 M phosphate, 25 °C Each data point is the mean value of at least three determinations.

Both k_I and k_{II} can be obtained by measuring v at [S] and $[H_2O_2]$ holding one fixed and varying the other over at least a tenfold range over which a hyperbolic dependence as shown in Figure 4A is observed. Fitting the linear form eq 4 to the data in Figure 4B gives k_I and k_{II}. This is referred to as the Lineweaver-Burke method.

$$\frac{1}{v} = \frac{1}{k_I[H_2O_2]Fe_t} + \frac{1}{k_{II}[S]Fe_t} \qquad (4)$$

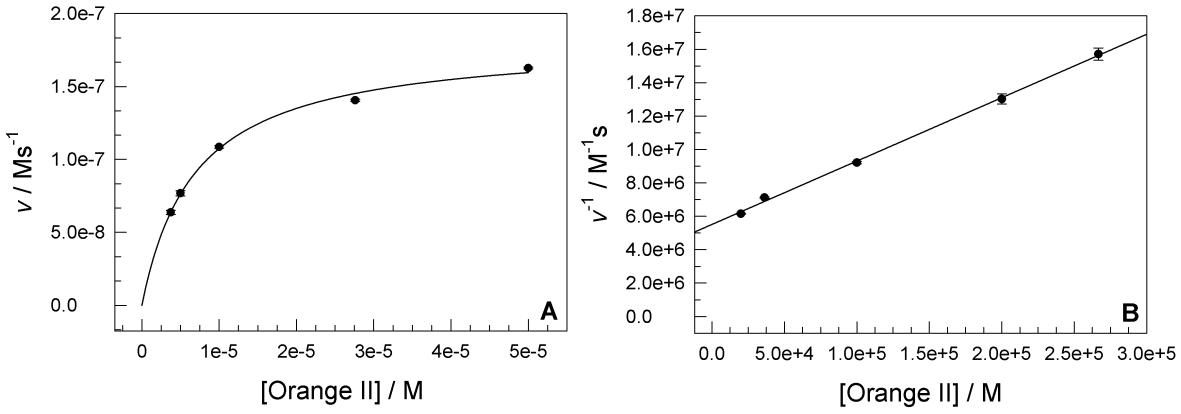

Figure 4. A: Plot showing the initial rates of **2c**-catalyzed bleaching of Orange II by H_2O_2 as a function of [Orange II] at pH 7 with [**3d**] = 1×10^{-7} M and [H_2O_2]= 1.0×10^{-3} M in 0.01 M phosphate, 25 °C. The line was generated by eq 1 using the rate constants obtained from B. **B**: Lineweaver-Burke plot of the data shown in **A**. Rate constants k_I and k_{II} were calculated from the slope and intercept of the line of best fit to the data according to eq 4. Each data point is the mean value of at least three determinations.

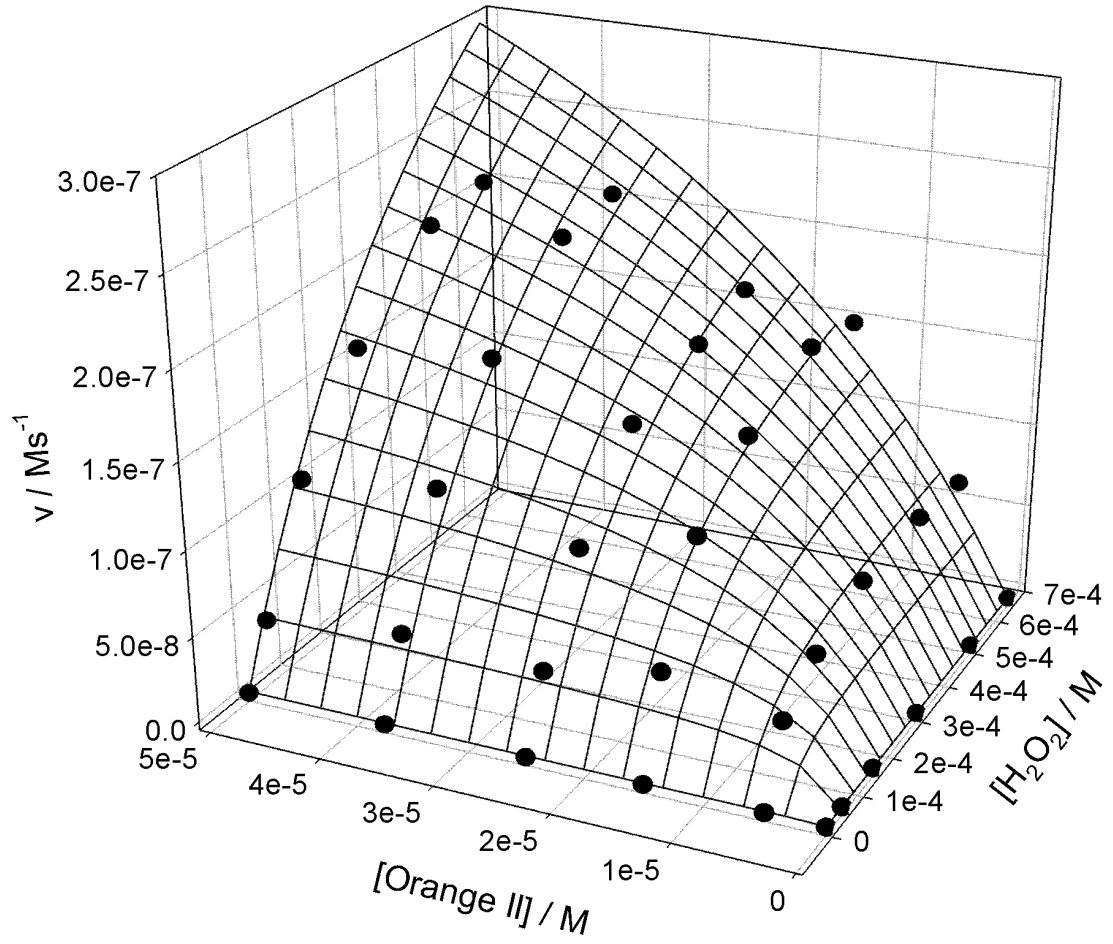

Figure 5. 3D-plot showing the initial rates of **3d**-catalyzed bleaching of Orange II by H_2O_2 as a function of $[H_2O_2]$ and [Orange II] at pH 9 with [**3d**]= 5×10^{-8} M in 0.01 M phosphate, 25 °C. Each data point is the mean value of at least three determinations. The rate constants in Table 1 were determined by fitting eq 1 to the data shown and used to calculate the mesh shown.

Alternatively, fitting eq 1 to a three dimensional plot such as that shown in Figure 3 in which a hyperbolic dependence of v on both $[H_2O_2]$ and [S] over at least a ten-fold concentration range of each also gives k_I and k_{II}. This is the method that was applied to obtain the pH 7, 9, and 11 **3e** rate constants in the bleaching of the azo dye Orange II.[2]

The strength of this approach is that it provides for the determination of both values from a large set of data. However, I have found using eqs 2 and 4 in tandem to be both more reliable and precise.

pK_{a1} as a Measure of TAML Catalyst Technical Performance

The reactivity of TAML catalysts is strongly influenced by pH.[5] Operation at near neutral pH is desirable for the removal of micropollutants from water, a major application of TAML catalysts, as it allows large volumes of ambient influent to be treated and released without substantial pH adjustment.[6] For large-scale removal of micropollutants in municipal water treatment, rapid function at neutral pH is nearly mandatory, and thus a significant part of the TAML catalyst design program has been aimed at meeting this requirement. Since the overall rate of most TAML processes is limited by catalyst activation, the design of novel catalysts has focused on those having greater pH 7 k_I values than their predecessors. Studies of the bell shaped distribution of the dependency of k_I on pH in the region of ~5–13.5, such as that shown in Figure 4 below for catalysis of the Orange II oxidation by **1a** in 0.01 M phosphate buffer at 25 °C, have determined the catalyst properties that raise k_I at neutral pH.[7]

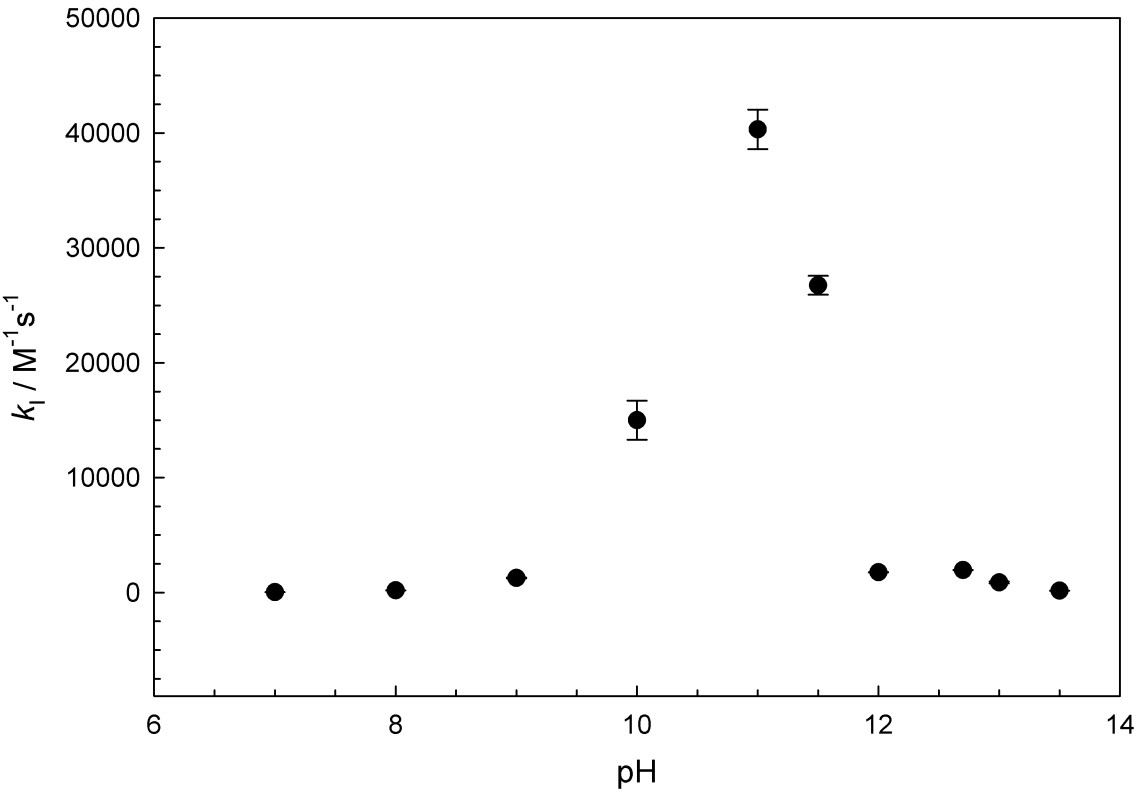

Figure 6. pH profile of the rate constant k_I for the oxidation of Orange II by H_2O_2 catalyzed by **1a**. Measurements were performed with [**1a**]=1 × 10^{-7} M in 0.01 M phosphate buffer at 25 °C.

For pH 7-13.15 **1** catalysis of substrate oxidation, a bell shaped dependence of k_I on pH is observed as shown in Figure 6. The three plateaus indicate that the reactivity may be attributable to three species interrelated by the loss or gain of at least one proton. In water at pH 6, resting TAML catalysts are considered to possess two labile axial water molecules.[7,8] As the pH of a TAML containing solution rises from 6–13, these water molecules are deprotonated giving the first two species shown in the box of Figure 7. Doubly deprotonated $\mathbf{A_3}^-$ has not been observed in the case of **1**, and has only been observed for **3e**, presumably because the Lewis acidity at the **3e** metal is much higher. A complete k_I scheme can be assembled through inclusion of the speciation of H_2O_2 within this range and consideration of all possible catalyst and oxidant combinations leading to

catalyst activation. Considering only k_1-k_4, the mathematical expression of these processes is eq 5. In the case of **1a**, the water ligands are not acidic enough for $\mathbf{A^{3-}}$ to be observed in the studied pH region (7–13.5) such that k_5 and k_6 related reactions are not relevant.

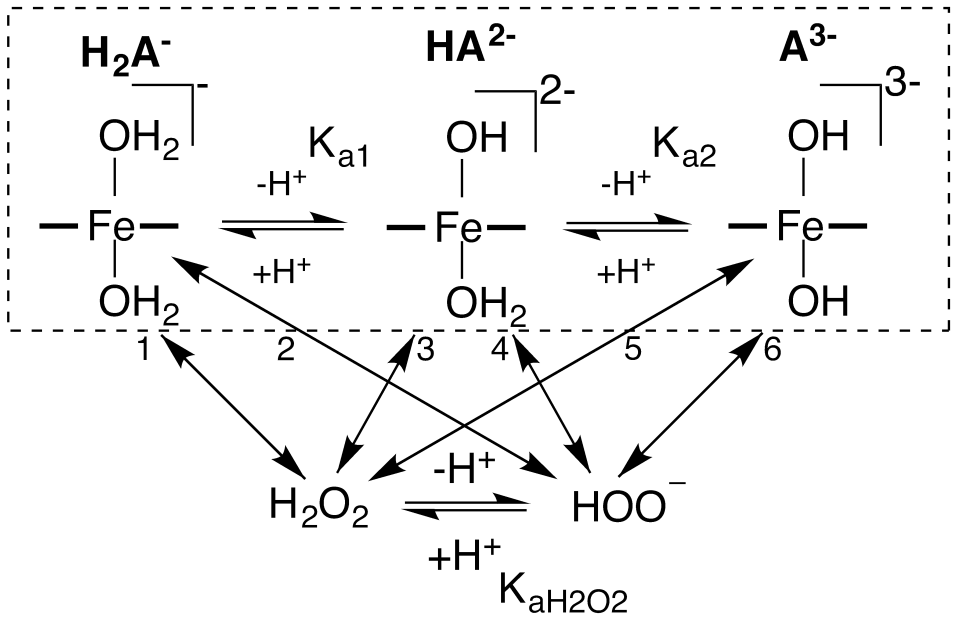

Figure 7. Aqueous resting TAML catalyst speciation and catalyst activation pathways found to operate in the presence of H_2O_2/HOO^- within the pH region of 6–13. The numbers adjacent to arrows 1–6 correspond to the respective catalyst activation pathway.

$$k_{\mathrm{I}} = \frac{k_1[\mathrm{H^+}]^2 + (k_3 K_{\mathrm{a1}} + k_2 K_{\mathrm{aH2O2}})[\mathrm{H^+}] + k_4 K_{\mathrm{a1}} K_{\mathrm{aH2O2}}}{[\mathrm{H^+}]^2 + (K_{\mathrm{a1}} + K_{\mathrm{aH2O2}})[\mathrm{H^+}] + K_{\mathrm{a1}} K_{\mathrm{aH2O2}}} \quad (5)$$

Fitting eq 5 to the bell shaped profile gives k_1 and k_4. Estimates of the kinetically indistinguishable k_2 and k_3 can be generated by assuming that one is negligible in fitting the data. In catalysis of ruthenium dye oxidation by **1b,** such fitting has found k_2 and k_3 to

be about 100 and 10 times greater than k_1 and k_4, respectively. Since the ~10^6 $M^{-1}s^{-1}$ value of k_2 found for this system was very large, k_3 was considered to be more reasonable. Since $\mathbf{HA^{2-}}$ is more electron rich than $\mathbf{H_2A^-}$, which should result in greater rates of activation for the former, it was assumed that $k_3 > k_2$, giving an order of $k_3 > k_2 > k_1 > k_4$. This assumption aligns with the relative values of k_4 and k_1 as the lower k_4 value has been rationalized as possibly resulting from a decreased rate of interaction of negatively charged HOO^- with the negatively charged catalysts coupled to its reduced oxidizing ability compared to H_2O_2 based on charge considerations. Consequently, $\mathbf{HA^{2-}}$ has been determined to be the most reactive form of resting TAML catalysts.[6,7] The bell shape derives from the markedly enhanced reactivity of this catalyst species relative to that of $\mathbf{H_2A^-}$ and $\mathbf{A_3^-}$ as well as the diminished reactivity with the peroxo anion which is present at negligible concentrations in the pH regime where $\mathbf{HA^{2-}}$ dominates the iron speciation.

The acid dissociation constant of the resting diaqua TAML catalyst can be obtained independently through spectrophotometric titration for comparison to the values obtained by fitting eq 5 to the kinetic data. When the pH of aqueous solutions of **1** is varied within the region of 7–12, a reversible sigmoidal change in the absorbance at a specific wavelength representing the loss of one proton is observed.[8] Fitting eq 6 to the data gives K_{a1} values that have been found to align well with those obtained by eq 5. Typical **1** pK_{a1} values range from 9.3–10.5[7].As noted above, **1** pKa_2 values have not be observed by this method. Maximum **1** k_1 values are typically found at pH 9.8–11[7], 0.5 pH units above pK_{a1}.[7,8]

$$\frac{\mathrm{A}}{[\mathrm{Fe^{III}}]_{\mathrm{tot}}} = \frac{\varepsilon_{\mathrm{H_2}A}[\mathrm{H^+}]+\varepsilon_{\mathrm{HA}}-K_{\mathrm{a1}}}{[\mathrm{H^+}]+K_{\mathrm{a1}}} \quad (6)$$

Since catalyst activation is typically rate determining, $\mathbf{HA^{2-}}$ most rapidly undergoes activation, K_{a1} controls the [$\mathbf{HA^{2-}}$] at pH 7, and maximum k_I values are found at 0.5 pH units above pK_{a1}, the key to maximizing the overall TAML oxidation rate of most substrates here lies in raising K_{a1} to 3.16×10^{-7} M^{-1} to give a pK_{a1} of 6.5. Since this process is iron atom centered, Lewis acid catalysis of the deprotonation of a water molecule, this can be achieved by decreasing the electron donation of the deprotonated amide ligands. Counterintuitively, the key to increasing the rate of oxidation of the iron center lies has been in making it less electron rich.[7,8] One method of accomplishing this is the appendage of electron-withdrawing substituents to the aromatic ring of the macrocycle.[8]

Impacts of Electron-Withdrawing Aromatic Substituents on TAML Technical Performance

Appendage of electron withdrawing groups to the aromatic ring of the **1** series of iron tetra-amido macrocyclic ligand (Fe-TAML) catalysts shown in Figure 1 has been observed to increase the rates of the pH 9 hydrogen peroxide-dependent activation of the resting catalysts (Fe^{III}) to form the active catalysts (Ac) (k_I) via the aforementioned decrease in the pK_a of the axial water molecules.[7] Hammett plots show a linear dependence for **1** of log(k_I) on composite Hammett parameters σ_{m+p} or $2\times\sigma_{m+p}$ (in the case of doubly substituted activators) in the pH 9 oxidation of Orange II[4] and a ruthenium

dye[7] with ρ=0.4 and ρ=0.3, respectively, in 0.01 M phosphate buffer at 25 °C. Similarly, a linear free energy relationship between the pKa$_1$ values of **1** and the pH 9 k_I values for **1** activation by ^{t}BuOOH in 0.01 M phosphate buffer at 25 °C has been found to have a line of best fit with a slope of -1 showing a strong correlation between the two.[6]

Rates of the pH 9 oxidation of Orange II by **1-Ac** have been shown to be markedly less sensitive to the appendage of electron withdrawing groups to the aromatic ring at pH 9. Hammett plots reveal a weak linear relationship (ρ=0.2) indicating that log(k_{II}) is nearly independent of σ_{m+p} in the pH 9 oxidation of Orange II in 0.01 M phosphate buffer at 25 °C.[4] This observed insensitivity of k_{II} to substitution with aromatic electron-withdrawing groups was attributed to the dominance of the keto tautomer of Orange II at pH 9 shown in Figure 8. However, a weak correlation was also observed in the pH 9 oxidation of ruthenium dyes[7] indicating that this may be a general feature of **1** catalysis at pH 9. A similarly weak correlation can be discerned from examination of the linear free energy relationship generated for pH 11 **1** catalysis of Safranine O oxidation.[9]

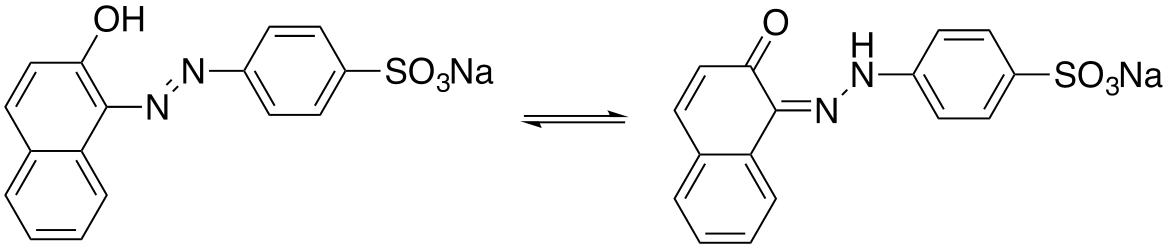

Figure 8. Previously proposed tautomerization of the azo dye model substrate Orange II.[4]

Electron-Withdrawing Groups and Operational Stability

Appendage of electron-withdrawing groups has also been found to increase the resistance of the resting catalysts to demetalation. As shown in Scheme 1, two demetalation pathways have been discovered. The first is specific acid demetalation which activators **1** undergo at pH < 4 the product of which has been confirmed to be the free ligand.[8,9] Equation 7 can be fit to the dependence of the observed rate of demetalation, k_{obs}, on [$HClO_4$]. Inclusion of a term for the second order dependence on [H^+] does not improve the fit. No increase in k_{obs} was observed on increasing the phosphate buffer ion concentration by one order of magnitude from 0.01 to 0.1 M confirming that this pathway is specific acid mediated.[5]

$$k_{obs} = k_1^*[\mathrm{H}^+] + k_3^*[\mathrm{H}^+]^3 \qquad (7)$$

Equation 7 indicates that the specific acid demetalation of TAML catalysts occurs via two pathways, one with a first order dependence on [H^+] parameterized by k_1^* and the other with a third order dependence on [H^+] parameterized by k_3^*. These can be rationalized by the sequence of events shown in Figure 9 below.

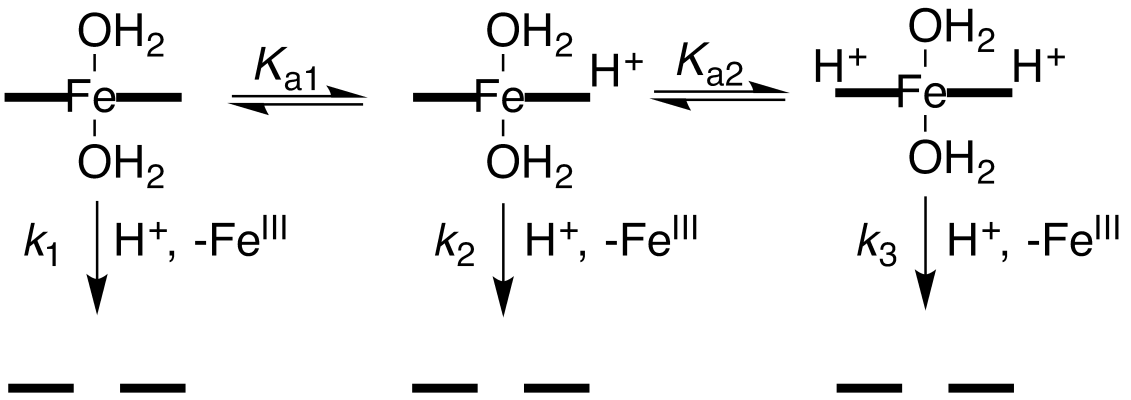

Figure 9. Pathways of specific acid demetalation of Fe-TAML resting catalysts to give the free base ligand.[8]

The mathematical expression of the sequence of events shown in Scheme 3 with the assumptions that K_{a1} and K_{a2} are sufficiently large for $K_{a1}K_{a2}$>>($K_{a2}[H^+]+[H^+]^2$) and k_2 is sufficiently small enough that ($k_1K_{a1}K_{a2}$-$[H^+]$+ $k_1[H^+]^3$) is >> $k_2K_{a2}[H^+]^2$ is eq 8 in which k_1*= k_1 and k_3*= $k_3(K_{a1}K_{a2})^{-1}$.

$$k_{obs} = \frac{(k_1K_{a1}K_{a2}[H^+]+k_2K_{a2}[H^+]^2+k_3[H^+]^3)}{(K_{a1}K_{a2}+K_{a2}[H^+]+[H^+]^2)} \quad (8)$$

While aromatic substitution with electron-withdrawing groups has little effect on either k_1^* or k_3^*, substitution of the geminal methyl groups of the malonamide with electron-withdrawing fluorine such as in **1b** and **1d** has been found to decrease by four and nine orders of magnitude, respectively. This indicates that for activators containing the geminal methyl groups, the more electron rich N—Fe bonds of the malonamide are likely to be the dominant site of amido N protonation.

The second pathway of **1** demetalation is a general acid process that can be mediated by phosphate at pH 5–7 as shown in Figure 10.[9] The product has been confirmed to be the free ligand.[5] Activators containing electron-withdrawing fluoro and cyclopropyl substituted malonamides do not undergo this phosphate buffer ion mediated demetalation under these conditions indicating that the process is also very sensitive to tail group substitution[5] likely because protonation of the more electron-rich malonamide N—Fe bonds is preferred over that of the phenylene diamine N—Fe bonds. First order linear dependencies of the rate of **1a** demetalation on the concentration of phosphate with intercepts of ~0 are observed at pH 6–9 and 45 °C confirming that at this elevated pH and temperature a general acid pathway operates and the specific acid demetalation pathway does not. The pH dependence of this k_{obs} is sigmoidal dependence with an inflection point at ~6.5, the pK_a of $H_2PO_4^-$, and approaches 0 at pH 9 implicating $H_2PO_4^-$ in the general acid process. Demetalation was also observed in the presence of picolinic acid however no demetalation was observed in the presence of the 3- and 4-substituted structural isomers indicating that for picolinic acid binding of the nitrogen of the heterocycle to the iron center precedes intramolecular proton transfer to the N—Fe bond. By analogy, the proposed mechanism of demetalation by phosphate shown in Scheme 4 below includes this preequilibrium binding though protonation from the bulk solution is kinetically indistinguishable. Aromatic substitution with electron-withdrawing groups was not found to alter the rate of general acid demetalation[5] indicating that the more electron-rich malonamide N—Fe bonds are the preferred site of protonolysis as the malonamide is isolated from the electronic effects of the aromatic substituents.

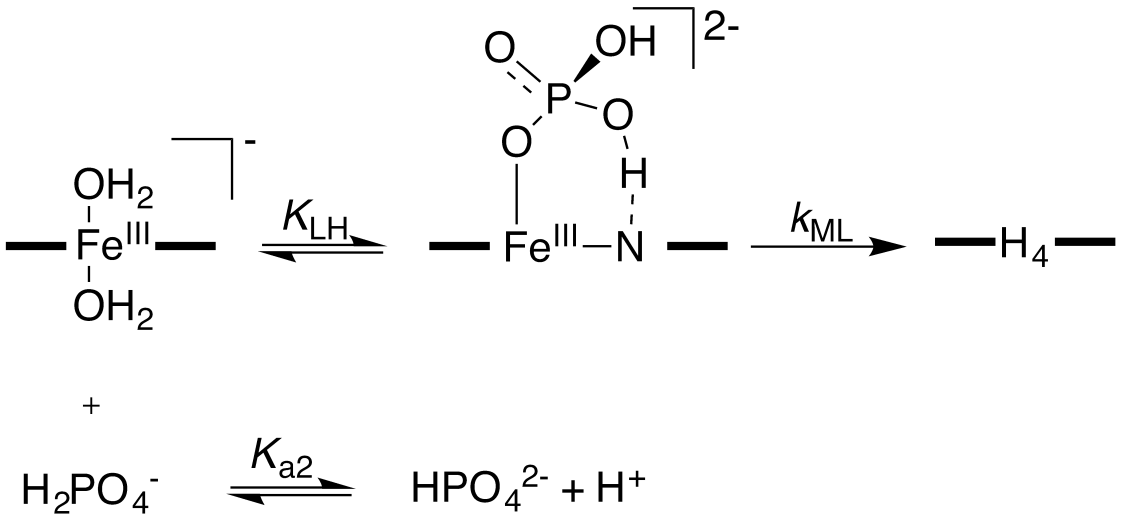

Figure 10. Proposed Mechanism of the Phosphate-Buffer Mediated General Acid Demetalation.[5]

Attempts to Advance the Technical Performance of TAML Catalysts Through the Design and Synthesis of Catalysts Having Novel Ligand Structures

Attempts have been made to advance the technical performance of TAML catalysts beyond that of **1** through the design of novel ligand systems. Such efforts by Sayam Sen Gupta and undergraduate Duane Prasuhn Jr. resulted in **2**, a 5'6'5'6 chelate ring system. Unfortunately, as was found for the 5'6'5'6' complexes of H_4**8** discussed in Chapter 1 of this thesis, **2a** is prone to specific acid demetalation the rate of which is given by eq 9 below. The **2a** k_1^* value of $5.5\pm0.5\times10^3$ is more than 1000 times greater than any **1** studied and compromises **2a** aqueous catalysis at pH 7.[8]

$$k_{obs} = (2 \pm 1) + (5.5 \pm 0.5) \times 10^3[\mathrm{H^+}] \qquad (9)$$

The nonplanar amides evident in crystal structures of **2a**, also observed for H_4**8** complexes, are thought to account for its instability. These are thought to derive from the

14-membered ring macrocycle of **2** which is larger than the 13-membered ring macrocycle of **1**. This work serves as a further indication that 14-membered 5,6,5,6 macrocyclic systems are not well suited to Fe-TAML catalysis. Though the synthesis of **2b** and **c** were planned and **2b** was generated, neither was characterized. The impacts of substitution with aromatic electron-withdrawing groups on **2** remain unknown. While **2a** has not proven itself to be a useful TAML activator, the synthetic pathway developed to generate it, shown in Figure 11 below, has.

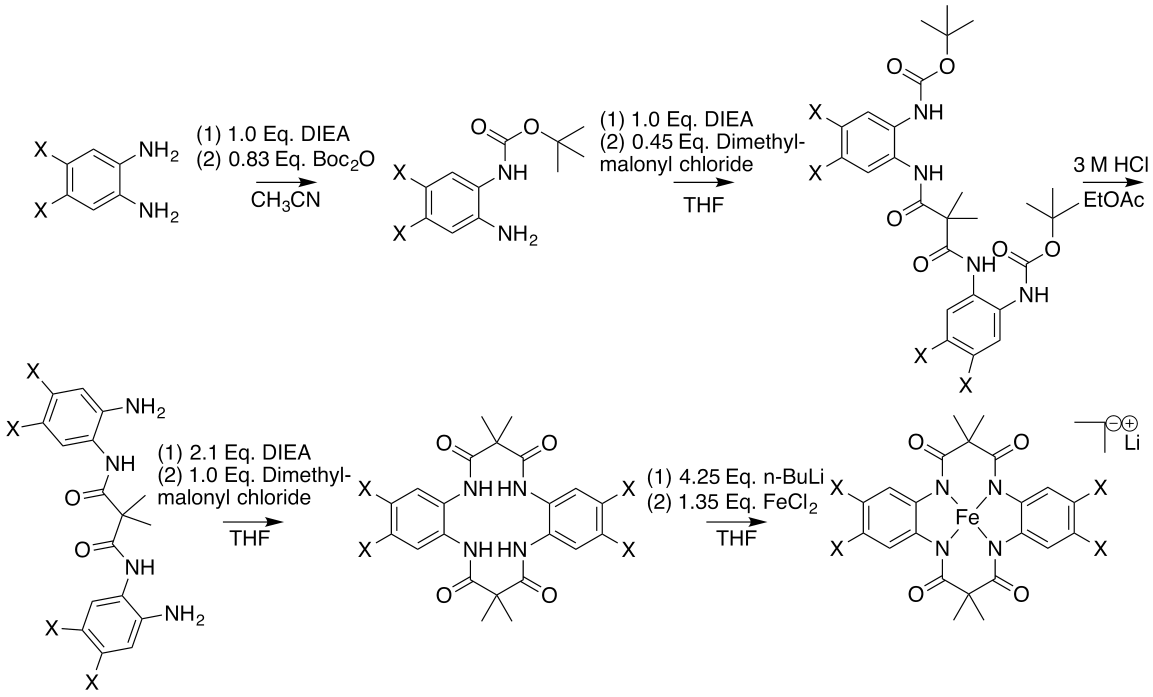

Figure 11. Synthetic sequence followed to generate **2**. **2a**: X=H; **2b**: X=Cl; **2c**: X=OCH_3.

Since catalysts with 14-membered ring macrocycles having alternating 5 and 6 membered ring chelates have been observed to be susceptible to hydrolysis, the synthetic pathway devised to generate **2** was modified by replacement of the second aliquot of dimethylmalonyl chloride of Scheme 2 with oxalyl chloride to give the 13-membered 5,5,5,6 chelating macrocycle **3**.[2,3] This pathway was used to generate **3a**, **3c**, and **3e**.

Unfortunately, **3a** was found to undergo slow phosphate buffer mediated demetalation in the absence of H_2O_2.[3,5] Additional hydrolytic stability was attained by appendage of electron withdrawing groups to the aromatic ring to give **3c** and **3e**, the latter of which was found to undergo $H_2PO_4^-$ induced demetalation 100 times more slowly than **3a** rendering the stability of **3e** comparable to that of **1a** by this measure.[35] Notably, **3** substitution with aromatic electron-withdrawing groups confers resistance to general acid demetalation whereas for **1** such substitution does not impact stability. This is because the aromatic substituents of **3** are able to communicate with the nitrogen atoms of the malonamide electronically via the conjugated π system to decrease the electron density of the malonamide N—Fe bonds, just as would be expected to result from substitution of the malonamide methylene carbon with electron-withdrawing groups.

Activator **3e** catalyzes the pH 7 oxidation of Orange II with k_I and k_{II} values of 1900±100 and (520±70)×10^3 M^{-1} s^{-1}, the highest of any TAML catalyst to date.[2] The kinetics of **3a**-catalyzed oxidation were not investigated. Neither the operational stability nor the kinetics of **3c**-catalyzed oxidation were investigated.

Table 1. Hammett parameters for aromatic substituents.

X	σ_m	σ_p
H	0.000[10]	0.000[10]
CO_2^-	+ 0.104[11]	+ 0.132[11]
	- (0.1±0.1)[11]	(0.0±0.1)[11]
$CONH_2$	+ 0.28[12]	+ 0.36[12]
Cl	+ (0.373±0.041)[10]	+ (0.227±0.040)[10]
CN	+ 0.678[10]	+ (1.000±0.042)[10]
NO_2	+ (0.710±0.069)[10]	+ (1.27±0.052)[10]
		+ (0.778±0.066)[10]

When the pH of aqueous solutions of **3e** is varied within the region of 7–12 changes in the absorbance at a specific wavelength are observed. These changes manifest as two sigmoidal patterns representing the sequential loss of two protons. Fitting eq 10 to the data gives K_{a1} and K_{a2} values that have been found to align well with those obtained through the use of eq 6. The highest K_{a1} and lowest pK_{a1} values of 3.98 ±0.05 × 10^{-9} and 8.4±0.1 to date have been found for TAML **3e**.[3] Consequently, the **3e** maximum k_I value is found at ~pH 9, much lower than the maximum k_I values attained at pH 11 and 10.2 for **1a** and **1c**, respectively.[2] Since two pKa values could be determined for **3e**, all three species H_2A^-, HA^{2-}, and A^{3-} were included in the catalyst activation scheme as shown in Scheme. Equation 9 is the mathematical representation of catalyst activation processes 1–6.

$$k_I = \frac{k_1[H^+]^3+(k_2K_{a1}+k_3K_{aH2O2})[H^+]^2+(k_4K_{a1}K_{aH2O2}+k_5K_{a1}K_{a2})[H^+]+k_6K_{a1}K_{a2}K_{aH2O2}}{[H^+]^3+(K_{a1}+K_{aH2O2})[H^+]^2+(K_{a1}K_{aH2O2}+K_{a1}K_{a2})[H^+]+K_{a1}K_{a2}K_{aH2O2}} \quad (10)$$

The **3e** activation rate constants $k_{1\text{-}6}$ as well as the acid dissociation constants K_{a1} and K_{a2} were determined by fitting eq 7 to the bell shaped dependence of k_I on pH. Of these, k_3 and k_4 have been estimated to be the largest indicating that the singly deprotonated $\mathbf{HA^{2-}}$ form of **3e** most rapidly undergoes activation.[3] While the proposed rationalization that **1** k_1 and k_2 are less than k_3 and k_4 as a result of more rapid resting catalyst oxidation due to additional electron donation to the iron center by the hydroxide ligand[7], this logic cannot be applied to $\mathbf{A_3^-}$ when the relative magnitudes of the **3e** k_5 and k_6, which are less than the **3e** k_2 are considered.[3] The so observed **3e** k_1 is within error of 0.

Green Design of TAML Catalysts

As the main application of TAML activators is removal of micropollutants from water, it is essential that they not become micropollutants themselves. For example, concerns have been raised about the incorporation of fluorine[6] as well as that of halogens in general and fragments not commonly found in nature[1] into the catalyst structure. Attention has been paid to the green design of TAML catalysts by the Collins Group in ways that are rare in catalyst development or *design* (as in this case).

In addition the potential for **1a**, **1b**, and **3e** to activate transcription mediated by the nuclear hormone human thyroid receptor (TRβ), human estrogen receptor (ERα), and rat androgen receptor (AR) at typical operating concentrations of 1×10^{-11}–1×10^{-5} M was assessed.[3] No transcription was observed implying that none of the activators studied bind to these receptors that are thought to be common targets for endocrine disruptors. While in both cases these results are undoubtedly good news for TAML chemistry, they are unable to provide insight into the design of activators of reduced toxicity. As will be seen in this chapter, this has been accomplished through comparative assays which screen for the disruption of zebrafish development.

Expanding the Suite of Activators Available

The possession of aromatic nitro groups has been associated with toxicity. For this and other reasons, an advanced precautionary stance has been adopted toward the use of **1c** and **3e** in large-scale water treatment. Nitrile groups are known to possess electron-withdrawing capacities similar to those of nitro groups (Table 1), however they have never been incorporated into a TAML framework. Consequently, the technical,

environmental, and health performances of **3d** were assessed in order to determine the relative suitability of **3** for large-scale implementation in water treatment. At this point, the general background of my studies having been established, with the absolute need to understand this for anyone like myself doing such and any student who might pick up on themes emanating from my work, the actual studies that have significantly expanded catalyst design will now be presented.

Results and Discussion

Synthesis of 3d

A **3** having each aromatic ring substituted with one nitrile group, **3d**, was synthesized following an adaptation of the **2** synthesis used to generate **3a**, **3c**, and **3e** shown in Figure 12.

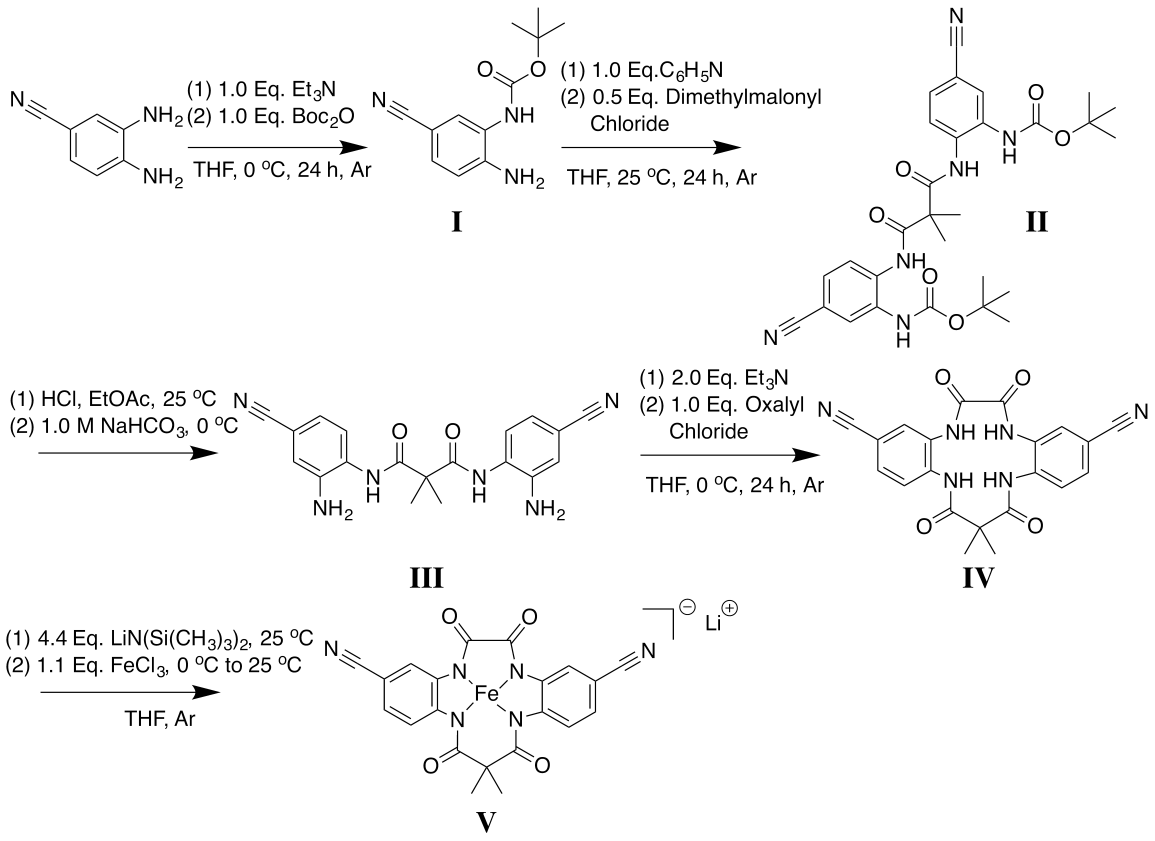

Figure 12. Synthetic sequence followed to generate **3d**.

Cation metathesis was performed to generate the Ph_4P^+ and PNP^+ salts of anion **3d**. In both cases recrystallization following the literature procedure gave red needles. While extremely dilute catalyst solutions gave squares. Unfortunately X-ray structures could not be obtained from any of the samples.

Evaluation of the Relative Technical Performances of 1 and 3

The pH 9 **3d** rate constants k_I and k_{II} in the oxidation of Orange II were determined through fitting eq 1 to a three-dimensional plot of the data shown in Figure 3 as was previously performed for **3e**.[2] Since the pH 9 k_I values so observed were very close to those of **3e** as shown in Table 2, a two-step method for determining accurate k_I

and k_{II} that provides a verification of the rate constants and requires less data points than the three-dimensional mesh was devised for use at pH 7. First the initial rate of overall substrate oxidation, v, was measured where a linear dependence on $[H_2O_2]$ was observed, the zero order dependence on [S] confirmed, and k_I determined by fitting eq 2 to the data as described and shown in Figure 1. Then both k_I and k_{II} were obtained using the previously described Lineweaver-Burke method as shown in Figure 2. Measurements of v were taken at increased $[H_2O_2]$ until v became nearly independent of $[H_2O_2]$, The k_I value obtained through the Lineweaver-Burke method approached that from eq 2. The second set of rate constants are reported. This has proven to be the most rigorous method for determining k_I and k_{II} in the neutral pH oxidation of Orange II by most TAML activators. The pH 7 **1a, 1b, 1c, 3c, 3d, and 3e** k_I and k_{II} in the oxidation of Orange II were determined in this manner. Only the Lineweaver-Burke method could be employed for **3a** and **3b** because of the similarity of the k_I and k_{II} values for these activators. The data so obtained are reported in Table 1 along with composite Hammett parameters $n\times\sigma_{m+p}$ where n represents the number of aromatic substituents and σ_{m+p} is the sum of the respective Hammett parameters for meta and para substitution in Table 1. In the case of the nitro group, the larger σ_p value of 1.27 was employed rather than the more widely reported value[11] of 0.778 because Hammett reported that the former more accurately models the behavior of aniline and phenol derivatives.[10]

Table 2. Rate constants ($M^{-1}s^{-1}$) for the neutral pH Fe^{III}-TAML catalyzed bleaching of Orange II by H_2O_2 at 25 °C in 0.01 M phosphate buffer.

pH	**TAML**	$X_1/X_2/R$	$10^{-1} \times k_I$	$10^{-3} \times k_{II}$	$n \times \sigma_{m+p}$	k_{obs} ratio
9	**3d**	$CN/H/CH_3$	1,800±300[a]	240±40[a]	—	
9	**3e**	$NO_2/H/CH_3$	1,600±200[2]	1,000±100[2]	—	
7	**1a**	$H/H/CH_3$	3.14±0.01	4.95±0.02	—	
7	**1c**	$NO_2/H/F$	35.0±0.2	41±1	—	
7	**1d**	Cl/Cl/F	36.1±0.1	120±10	—	
7	**3a**	$H/H/CH_3$	25±6	0.84±0.03	0.000	
7	**3b**	H/H/F	90±10	0.9±0.1	—	
7	**3c**	$Cl/Cl/CH_3$	149±2	40±2	1.290	
7	**3d**	$CN/H/CH_3$	185±9[b]	260±10[b]	3.356	
7	**3d**	$CN/H/CH_3$	190±10[c]	—	3.356	
7	**3e**	$NO_2/H/CH_3$	190±10[2]	520±70[2]	3.960	

[a]Generated from the data shown in Figure 3, [b]Generated from the data shown in Figure 2B, [c]Generated from the data shown in Figure 1A.

Six key insights can be gained from the data in Table 2. First, the reactivities of **1** Rc and Ac differ from those of **3** Rc and Ac. The **1a** Rc undergoes activation an order of magnitude more slowly than does the **3a** Rc. However, the **1a** Ac oxidizes Orange II 5–6 times more rapidly than does that of **3a**.

Second, in most pH 7 and pH 9 applications, **3d** and **3e** will display nearly identical initial overall rates of substrate oxidation in accordance with the often rate determining pH 7 and pH 9 k_I values. This is significant as **3e** has the highest pH 7 k_I of any TAML catalyst to date.[2] However, in the case of very difficult to oxidize substrates **3e** will outperform **3d** by this measure in accordance with the pH 7 and pH 9 k_{II} values, which are indicative of the relative oxidative potency of the Ac of each. This difference will be most prominent at pH 9 in systems where $k_{II}[S] << k_I[H_2O_2]$ and eq 3 applies.

Third, pH 7 activation of **3** Rc is sensitive to the identity of the geminal substituents of the malonamide while substrate oxidation at pH 7 by **3** Ac is not.

Replacement of the geminal dimethyl groups of the malonamide of **3a** with fluorine to give **3b** increases catalyst activation, k_I, by a factor of four. However, the k_{II} values are unaffected indicating that this site does not contribute substantially to the Ac LUMO into which the substrate electron flows during its oxidation. It is possible that this is indicative of an Ac arising during sequential electron transfer from the substrate most accurately formulated as a radical cation with substantial presence of the oxidation equivalent in the aromatic rings in the cases of **3a** and **3b**. If so, these comparatively low **3** $\boldsymbol{k_{II}}$ values would represent the diminished reactivity of such an Ac possibly due to increased stability deriving from delocalization of the oxidation equivalent or less efficient electron transfer to it. This will be further examined in Chapter 3.

Fourth, with the exception of **3a**, all **3** activators display greater initial overall rates of substrate oxidation in most pH 7 applications than any **1** activator in accordance with the relative k_I values. However, only **3d** and **3e** outperform **1** by this measure in all pH 7 applications in accordance with the relative k_{II} values.

Fifth, the pH 7 oxidation of Orange II by **3** Ac is limited by the same rate-determining step that is accelerated by appendage of electron withdrawing groups to the catalyst. As shown in Figure 13B, $\log(k_{II})$ exhibits a linear dependence on $n\times\sigma_{m+p}$. Such linear dependencies are observed for reactions in which all compounds evaluated share both a common mechanism and rate-determining step.[13] The slope of this dependence, $\rho=0.72\pm0.03$, is significantly larger than those observed for **1** at pH 9. It is possible that this difference derives from the same increased communication of the aromatic electron-withdrawing groups with the malonamide nitrogen atoms that accounts for resistance of substituted **3** to general acid demetalation. Unlike the demetalation, the greater impact of

aromatic substitution with electron-withdrawing groups on k_{II} of **3** would result from the impact of such groups on all four amido nitrogens whereas in **1** only two are affected.

Sixth, the available data indicate that for **3**, the pH 7 elementary catalyst activation step shown in Scheme 1 is the sum of at least two steps. While caution must be used when abstracting from a sample of only four activators, the clear linear dependence shown in the log(k_{II}) Hammett plot of Figure 13B adds confidence to conclusions based on the concave downward dependence of the log(k_I) Hammett plot displayed in Figure 13A. This differs from the linear relationship with ρ=0.4 observed for **1** in the pH 9 oxidation of Orange II[4], as with the difference in the dependence at k_{II} this likely derives from the speciation of Rc as the H_2A form.

Nonlinear Hammett relationships such as that shown in Figure 4A are evidence that the observed rate constant is composed of rate and equilibrium constants of several steps.[13] This behavior contrasts with the linear dependence of k_{II} shown in Figure 13B to which eq 11 is the analytical form of line of best fit. Given (i) the known difference in Rc speciation at pH 7, (ii) the proposed mechanism of phosphate buffer induced **1** and **3** demetalation observed at pH ~7, (iii) the similarity of the **3d** and **3e** k_I values that may signal a shift in the rate determining step of catalyst activation from one dependent on the electronic environment of the iron center to one which is less sensitive to it, and (iv) the pH 7 evidence of weak binding and inhibition of k_I by one solvent molecule recently observed by fellow graduate student Ms. Liang Tang and I,[14] it is possible that the nonlinear Hammett plot observed for **3** derives from a preequilibrium binding of H_2O_2 followed by a catalyst activation step. While a binding of H_2O_2 to the Fe^{III} of the resting catalyst almost certainly occurs and precedes activation, we have yet to find evidence of

it. This **3** nonlinear Hammett relationship may be the first evidence of it. Unfortunately the error in the **3a** k_I value which is likely a consequence of the similarity of the **3a** k_I and k_{II} values which can complicate measurements compromises this assertion due to the relative concentrations of H_2O_2 ca 10^{-3} and Orange II ca 10^{-5} which allow accurate measurement and dictate appropriate measurement time intervals and UV absorption. Confirmation with a different substrate might better establish this as would a comparison of the performance of the two over a wide pH range. The similarity of the pH 9 **3d** and **3e** k_I values does indicate that this behavior may be characteristic of **3** catalysis.

A similar sequence of steps leading to activation of **1** Rc has been proposed.[7] Previous work found that exchange of peroxide to the active site of the Rc was not rate determining. This conclusion was based on the pH 9.2 rate constant for the exchange of water to the active site, k_{ex}, which was estimated to be $\geq 1.9 \times 10^5$ s^{-1}. If exchange of peroxide to the active site were rate determining the equality $k_{ex}=k_I[H_2O_2]$ should hold. This would give $k_I = 1.9 \times 10^8$ $M^{-1}s^{-1}$ at 1×10^{-3} M at the highest $[H_2O_2]$ used in the study however the experimental pH 9 k_I value was determined to be only $\sim 5 \times 10^3$ $M^{-1}s^{-1}$ indicating that some other much slower process determines the rate of **1** activation.

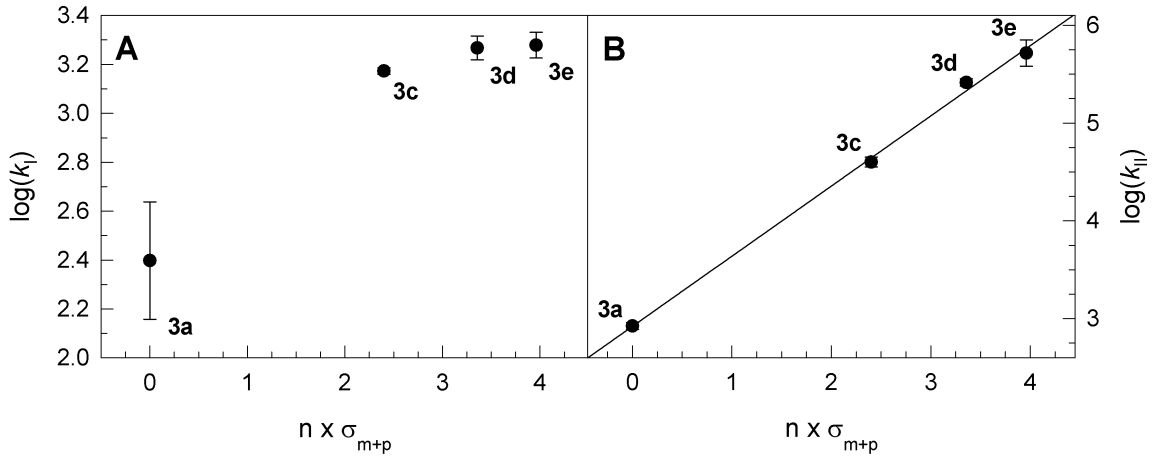

Figure 13. Hammett plots of the dependence of log(k_I) (**A**) and log(k_{II}) (**B**) on n×σ_{m+p}. Equation 10 is the analytical form of the line in (**B**). Measurements of rate constants were made at 25 °C in 0.01 M Phosphate buffer at pH 7 using the procedure discussed in the text.

$$\log(k_{II}) = (0.72 \pm 0.02)\text{n}\times \sigma_{\text{m+p}} + (2.92 \pm 0.07) \qquad (11)$$

Evaluation of the Electrochemistry of 3

The tetraphenylphosphonium salts of four **3** activators were studied by cyclic voltammetry to examine the relationship between the formal potential for any redox couples and the rate constants k_I and k_{II} in catalysis of the oxidation of Orange II by H_2O_2. Cyclic voltammograms of **3a**, **3c**, **3d,** and **3e** (1×10^{-3} M) were recorded in a CH_3CN solution of 0.1 M [^{n}Bu$_4$N][PF_6]. Two redox couples were observed as shown in Figure 14A. In all cases, a linear dependence of the forward peak current, $i_{p,f}$, on the square root of the scan rate, $v^{1/2}$, was observed as shown in Figure 14B indicating that the observed electron transfer was reversible. The redox potentials for each couple are shown in Table 3.

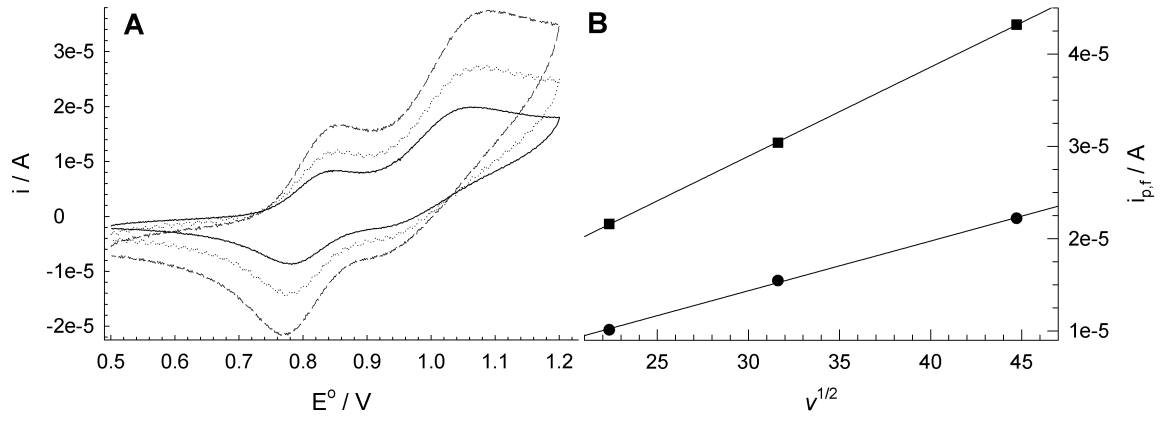

Figure 14. Electrochemical properties of **3e**. **A:** Cyclic voltammagrams of a 1.00×10^{-3} M CH_3CN solution of **3e** with 0.1 M [^{n}Bu$_4$N][PF_6] at a glass carbon electrode recorded at scan rates of 0.5 (solid line), 1.0 (dotted line), and 2.0 V/s (dashed line). **B**: plot of the square root of the scan rate, $v^{1/2}$, vs forward peak current, $i_{p,f}$. Circles: E^o_1, squares E^o_2.

Table 3. Redox potentials of various **3** activators (1.00×10^{-3} M) in 0.1 M [^{n}Bu$_4$N][PF_6] / CH_3CN.

TAML	E^o_1	E^o_2
3a	0.49	0.80
3c	0.68	0.93
3d	0.74	1.00
3e	0.81	1.01

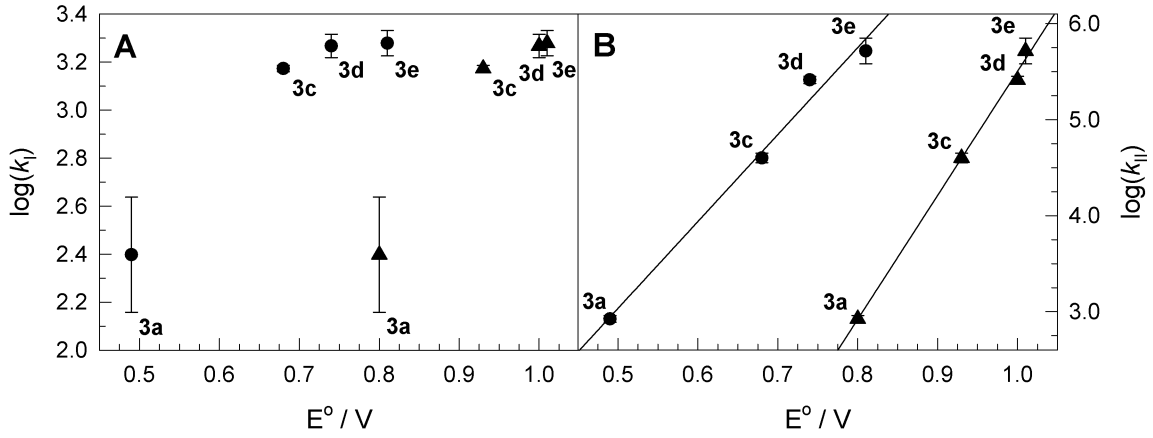

Figure 15. Dependence of log(k_I) (**A**) and log(k_{II}) (**B**) on the redox potentials of **3**. Circles: E^o_1, squares E^o_2. Equations 12 and 13 are the analytical forms of the lines of best fit to the first and second redox potentials, respectively, in (**B**).

The logarithms of the rate constants k_I and k_{II} were correlated to the first and second redox potentials as shown in Figure 15. A concave downward dependence of log(k_I) on each set of redox potentials is observed which agrees well with that of the Hammett plot Figure 13A. This dependence is more clear than that of Figure 13A likely as a result of the greater accuracy of electrochemical experiments over estimations of electronic properties based on Hammett parameters. This was cautiously interpreted as further evidence that k_I is the sum of at least two steps.

The dependence of log(k_{II}) on each set of redox potentials is linear in agreement with that observed in the Hammett plot Figure 13B again indicating that a common mechanism operates in the oxidation of Orange II by the Ac of **3** the rate of which is increased by appendage of electron withdrawing substituents. Equations 12 and 13 are the analytical forms of the lines of best fit to the first and second redox potentials, respectively, as shown in Figure 15B.

$$\log(k_{II}) = (9.1 \pm 0.1)\mathrm{E^o}_1 - (1.5 \pm 0.5) \quad (12)$$

$$\log(k_{II}) = (12.9 \pm 0.5)\mathrm{E^o}_2 - (7.4 \pm 0.5) \quad (13)$$

Determination of the pK_a of the 3d Axial Water Molecule

In previous work, fitting of eq 10 to a **3e** k_I pH profile was observed to give pK_{a1} and pK_{a2} values of 8±1 and 10±1, respectively, which agree well with the respective values obtained through spectrophotometric titration of 8.43±0.15 and 9.98±0.15, the lowest pK_a values of any TAML to date. This represented a massive shift in the pH of the maximum rate of substrate oxidation in most applications from ~10.4 to ~8.9 and accounts for the approximately one order of magnitude increase in the pH 7 k_I over that of **1c** giving it the greatest pH 7 k_I value of any TAML to date. Consequently, an important comparison between **3d** and **3e** concerns the value of pK_{a1} since any new activators should preserve this lower pK_{a1} advantage to be competitive. This value can also be used to estimate the pH at which the maximum rate of overall substrate oxidation by **3d** will be found in most applications.

Consequently, experiments to determine the pK_a of the axial water molecules of **3d** in water by spectrophotometric titration were undertaken. Spectra of a 0.01 M phosphate buffered 7.58×10^{-5} M **3d** solution were recorded periodically during the gradual basification of the solution from pH 5.9–11.7 as shown in Figure 16. As was found for **3e**, spectral changes of **3d** are smaller than those of **1** so the absorbance changes at two different wavelengths were fit to eq 14 and pK_a values were determined singly as has been described.[15]

These small spectral changes require each pK_a to be obtained independently of the other. This was performed by examining absorbance changes at a wavelength at which the absorbance of one conjugate acid/base pair changes, but that of the third species does not allowing the distribution of the conjugate acid/base pair to be observed over the entire pH range of the titration without interference from the third species.

$$\frac{\mathrm{A}}{[\mathrm{Fe^{III}}]_{\mathrm{tot}}} = \frac{\varepsilon_1[\mathrm{H^+}]+\varepsilon_2 K_\mathrm{a}}{[\mathrm{H^+}]+K_\mathrm{a}} \tag{14}$$

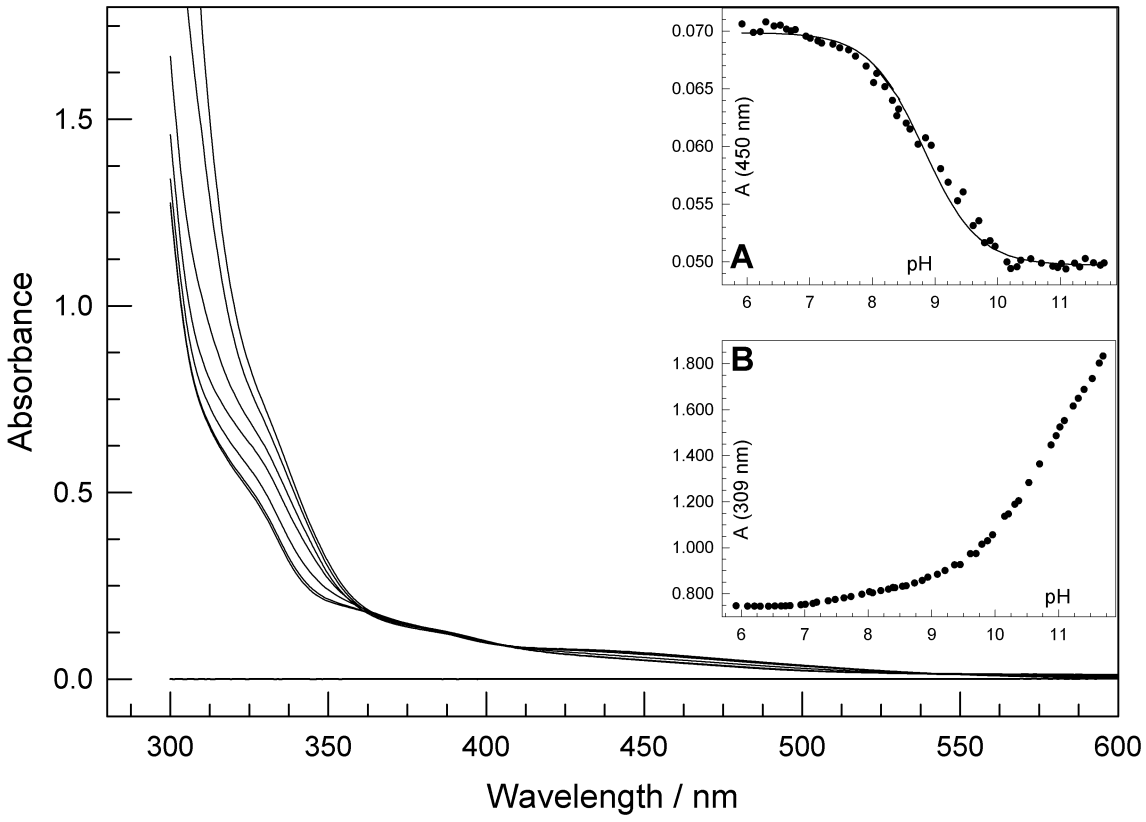

Figure 16. Spectral variations with increase in pH of **3d** (7.58×10^{-5} M) in 0.01 M Phosphate solution over the pH range 5.9-11.7 and the instrument baseline 25 °C. Insets **A** and **B** show the 450 and 309 nm spectral changes respectively. The solid line in inset **A** was calculated using the best-fit parameters of eq 11.

For **3d**, the most appropriate wavelength for observing the first conjugate acid/base pair is 450 nm (Figure 16A). Fitting the data in Figure 16A to eq 14 with the parameters shown in Table 4 resulted in a pK_{a1} value of 8.8±0.1, 0.4 units greater than the **3e** pK_{a1} of 8.43±0.15.[15] The reversibility of these changes was confirmed by quickly measuring spectra of a fresh sample of **3e** in 0.01 M phosphate buffer sequentially at pH 7.6, 9.0, and 7.6. While the spectrum at pH 9 was unique, the initial and final spectra were identical indicating that these changes are fully reversible. No wavelength could be found for the determination of pK_{a2}. As shown in Figure 16B, the 309 nm absorbance of one of the species observed at 450 nm was insensitive to pH. It appeared as if the 309 nm data might adopt the desired sigmoidal shape if measurements were taken at more basic pH values.

Table 4. Titration parameters for **3d**: Extinction coefficients (in M^{-1} cm^{-1}; ε_1 and ε_2 are 450 nm extinction coefficients for the fully protonated and singly deprotonated forms, respectively), K_{a1} (in M^{-1}) and pK_{a1} values obtained by fitting the data in the inset of Figure 7 to Equation 3.

Inset	Direction	λ / nm	Species	ε_1	ε_2	K_a	pK_a
16A	Basification	450	H_2A^-/HA^{2-}	922	656	$1.5\pm0.1\times10^{-9}$	8.8±0.1
17A	Acidification	450	H_2A^-/HA^{2-}	2138	727	$2.8\pm0.2\times10^{-11}$	9.6±0.1

In hopes of observing a plateau in the absorbance changes at 309 nm for the determination of pK_{a2}, a second spectrophotometric titration was performed. UV-Vis spectra of a pH 12.9, 0.01 M phosphate buffered, 7.58×10^{-5} M **3d** solution were recorded

while gradually acidifying to pH 6.1, the reverse direction of the previous titration, as shown in Figure 17. The spectral changes differ markedly from those observed on basification. Most notably, the absorbance values at wavelengths above 400 nm rise with decreasing pH. Unfortunately, no 309 nm endpoint was observed as is shown in Figure 17B. A plot of the sigmoidal absorbance changes at 450 nm differs from that observed previously. Fitting eq 14 with the parameters shown in Table 5 to the data in Figure 17A resulted in a pK_{a1} value of 9.6±0.1, 0.8 units greater than the aforementioned pK_{a1} of 8.8±0.1.

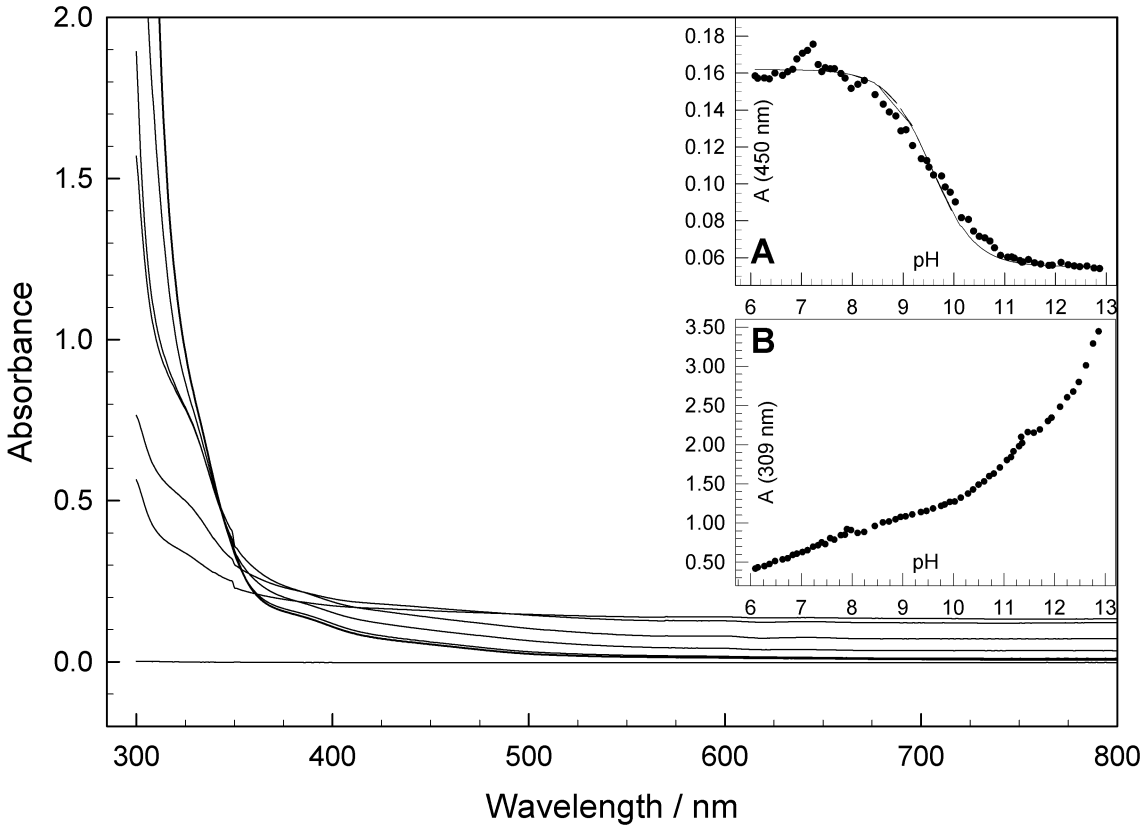

Figure 17. Spectral variations of a **3d** (7.58×10^{-5} M) solution in 0.01 M Phosphate buffer at 25 °C over the pH range 5.9-12.9 and the instrumental baseline. The inset shows the 450 nm spectral changes selected for calculating pK_a. The solid line was calculated using the best-fit parameters of eq 11.

Spectra recorded at pH 11 and 8 from each experiment were superimposed as shown in Figure 18. The pH 11 spectra from basification and acidification are nearly identical while those at pH 8 differ markedly. This is a strong indication that the species present at pH 11 are identical while those at pH 8 are not.

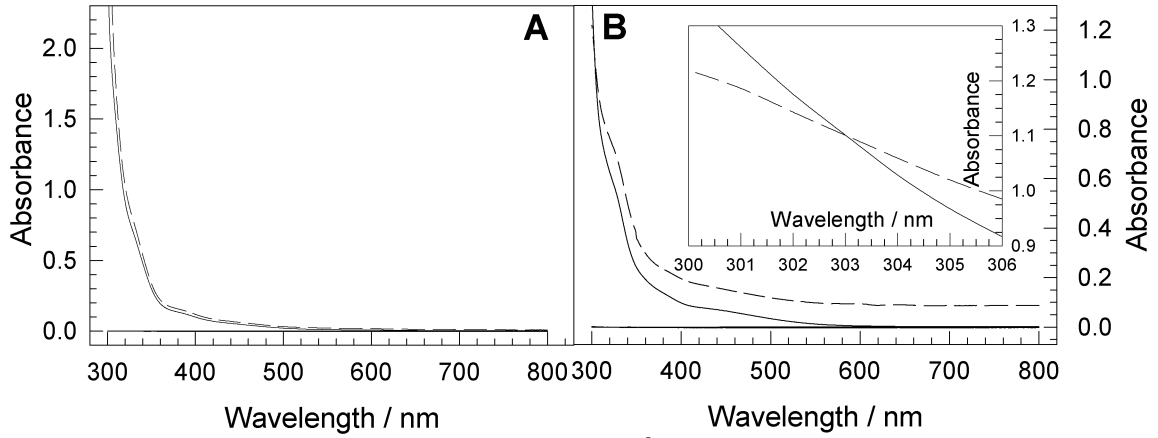

Figure 18. (A) pH 11 and **(B)** pH 8 spectra of **3d** (7.58×10^{-5} M) solutions in 0.01 M Phosphate buffer at 25 °C. Solid lines show spectra from basification titration, dashed show those from acidification.

Taken together these observations strongly indicate the following. First, the pK_a observed on basification of 8.8±0.1 is the pK_{a1} of diaqua **3d**. This value is consistent with that expected from the Hammett parameters in Table 1, the respective **3d** and **3e** k_{II} values in Table 2, the redox potentials of Table 3, and the **3e** pK_{a1} value of 8.43 ±0.15. Second, **3d** undergoes an irreversible change at pH 11. Acidification of a pH 12.7 solution of **3d** to pH 11 results in the same species observed to result from basification however at lower pH a different set of species having a p*K*a distinct from that of **3d** is observed.

Third, this irreversible change is likely the hydrolysis of the nitrile groups of **3d** to give structure **3f** shown in Scheme 1. At ~pH 11 **3d** undergoes irreversible conversion to a less electron-withdrawing aromatic group. Nitro-substituted **3e** did not undergo an irreversible change at this pH indicating that it is likely attributable to the nitrile groups of **3d**. The p*K*a$_1$ value assigned to **3f** is found at 0.8 units higher than that of diaaqua **3d** as would be expected of a catalyst bearing significantly less electron-withdrawing

aromatic groups than nitriles. Nitriles are known to undergo hydrolysis under basic conditions to give carboxylic acids via intermediate amides. As carboxylic acids are known to have pK_a values of ~6, above pH 7 the carboxylate anion is the predominant final form. As an aromatic group, both the amide and the carboxylate anion are less electron-withdrawing than nitriles as indicated by the relative values of the Hammett parameters in Table 1. Consequently the structure present at the beginning of the second titration is not **3d** but instead a different species which may be **3f** or an intermediate amide also expected to have significantly reduced elctron-withdrawing capacity; **3f** is identified in Figure 1.

Fourth, **3f** may form additional species that result from hydration of the carboxylate. The **3e** pK_{a2} value is 9.98±0.15, ca 1.6 pH units above pK_{a1}, and the endpoint of this titration occurs at pH 10.5, 0.5 pH units above the pK_{a2}. Assuming **3f** behaves similarly, the pK_{a2} of **3d** would be expected to be found at ~11.2 with the endpoint of the titration occurring at pH ~11.7. While the absorbance changes at 309 nm do show a slight deviation at pH 11.5 (Figure 16B) no clear endpoint is observed upon further basification. The continual rise in absorbance observed instead indicates that the distribution of species present continues to evolve with increased pH. This may be due to hydrolysis of the amide intermediate en route to the carboxylate. However, carboxylate anions have been observed to undergo hydrolysis via the standard tetrahedral intermediate proposed to result from nucleophilic addition to carbonyl compounds. At high pH, it is also possible that this second endpoint is muddled by the reversible addition of hydroxide to one or both **3f** carboxylates.

In sum, the second p*K*a of **3d** is unobservable because the nitrile groups undergo an irreversible chemical change, probably to eventually yield **3f** upon approaching pH 11, the pH at which the second endpoint should be observed. Since this new species bears two less electron-withdrawing groups it has a higher pK_{a1} than **3d**. This transformation is expected to decrease the activity of **3d** in line with the known relationships between k_I, k_{II} and the Hammett parameters for electron-withdrawing aromatic substituents. Consequently, it is unlikely that **3d** will match the performance of **3e** in applications at pH >10.

Evaluation of the Environmental Performances of 1 and 3

Finally, the environmental and potential health performances of **1a, 1b, 1c, 3a, 3b,** and **3c** were assessed by zebrafish development assays, a TiPED Tier 4 test which expands opportunities for exploring a diversity of toxicity endpoints which may or may not result from endocrine disruption.[16] This insistence that TAML catalysts be first tested for low dose adverse effects before being commercialized is a foundational principle of the IGS research. The zebrafish is an emerging model for the assessment of developmental toxicity and human health.[17-19] It's great advantage is that it has the power to detect a broad range of low dose adverse effects, endocrine related or otherwise. Experiments were performed by Dr. Lisa Truong in the Tanguay lab at Oregon State University. The chorion, a protective acellular embryonic membrane was removed from the zebrafish embryos prior to their exposure to 0.08, 0.4, 2, 10, 50, and 250 μM solutions of each activator though concentrations of activators used in TAML applications are typically below 3 μM. Negative and positive controls were conducted by

exposure to 0 μM TAML and 5 μM trimethyltin chloride, respectively. Each embryo was evaluated for developmental malformations at 24 and 120 hours post fertilization (hpf). At 24 hpf embryos were evaluated for mortality (MO24), developmental progression (DP24), spontaneous movement (SM24), and notochord distortion (NC24). At 120 hpf the embryos were screened for 18 endpoints. First they were scored for mortality (MORT) then euthanized and evaluated for abnormal morphology. The embryos which survived exposure were then evaluated for sixteen morphological malformations and one behavioral effect including yolk sac edema (YSE_), bent body axis (AXIS), eye (EYE_), snout (SNOU), jaw (JAW_), otic (OTIC), pericardial edema (PE__) brain (BRAI), somite (SOMI), pectoral fin (PFIN), caudal fin (CFIN), circulation (CIRC), pigmentation (PIG_), trunk length (TRUN), swim bladder (SWIM), notochord distortion (NC__), and alterations in touch response (TR__). The data are included below as Figure 19. The concentration of each compound which induced mortality in 50% of the sample (LC_{50}) and that at which adverse effects including mortality were observed in 50% of the sample (EC_{50}) were also determined as shown in Table 5.

Toxicity differentials were observed across **1** and **3**. Within **1**, **1c** displays the greatest toxicity while **1a** and **1b** show none at all concentrations tested. No **1** induced mortality. Consequently LC_{50} values could not be determined. Only **1c** induced malformations with an EC_{50} value of 32 μM including disruptions of notochord development. This indicates that **1a** and **1b** have similar environmental performances with respect to disruption of zebrafish embryo development. While **1b** and **1c** will exhibit the same technical performance in most pH 7 applications in accordance with the k_I values (Table 1), **1b** possesses superior environmental performance as indicated by this

model. This establishes **1b** as the optimal **1** as evaluated by both technical and environmental performance.

No toxicity was observed for activator **3a**. For the remaining **3**, developmental disruption increases in the order **3e**, **3d**, **3c** with EC_{50} values of 245, 25.6, and 4.5 μM, respectively. Only **3c** and **3e** induced mortality with LC_{50} values of 26.7 and 235 μM, respectively. Activator 3c was the most toxic **3** killing all of the developing zebrafish embryos at 50 and 250 μM. As a result no other **3c** exposure data could be obtained at these concentrations. Disruption of notochord development was observed for 10 μM **3c** exposure. While **3a** possesses the highest environmental performance, **3e** performs equally well at all tested concentrations below 250 μM. Though **3d** and **3e** will exhibit similar technical performance in most pH 7 and pH 9 applications, **3e** is superior as evaluated by both technical and environmental performance.

At application relevant concentrations of ≤2 μM the selected **1** and **3** TAML activators are not toxic to zebrafish that have had their protective chorions removed to increase bioavailability of test chemicals. Neither **1b** nor **3e** induced toxicity below 250 μM. However, **3e** possesses greater pH 7 technical performance in all applications. Thus at pH 7 **3e** has the highest technical and environmental performance of any TAML to date by these measures when employed at concentrations below 250 μM. Chlorine-substituted **1c** and **3c** induced the greatest amount of developmental disruption followed by nitrile-substituted **3d** while nitro-substituted **1b** and **3c** induced no toxicity below 250 μM. These results suggest a relative toxicity order for aromatic substituted TAML catalysts of $Cl>CN>NO_2$. This order has been observed in a study of toxicity para substituted chloro, cyano, and nitrophenols towards rainbow trout cells (RTG-2) with

EC^{50} values of 9.4, 10.3, and 12.1[20], respectively, and monosubstituted chloro, cyano, and nitrobenzene towards fathead minnows with $-\log LD_{50}$ values of 0.7, 0.21, and 0.01, respectively[21]. The order of **3** reactivity increases in the opposite direction Cl<CN<NO_2 indicating that for **3** increases in TAML reactivity are accompanied by decreases in toxicity with the exception of **3a**. The results suggest that substitution of future catalysts with aromatic nitro groups will likely increase reactivity while not substantially increasing toxicity.

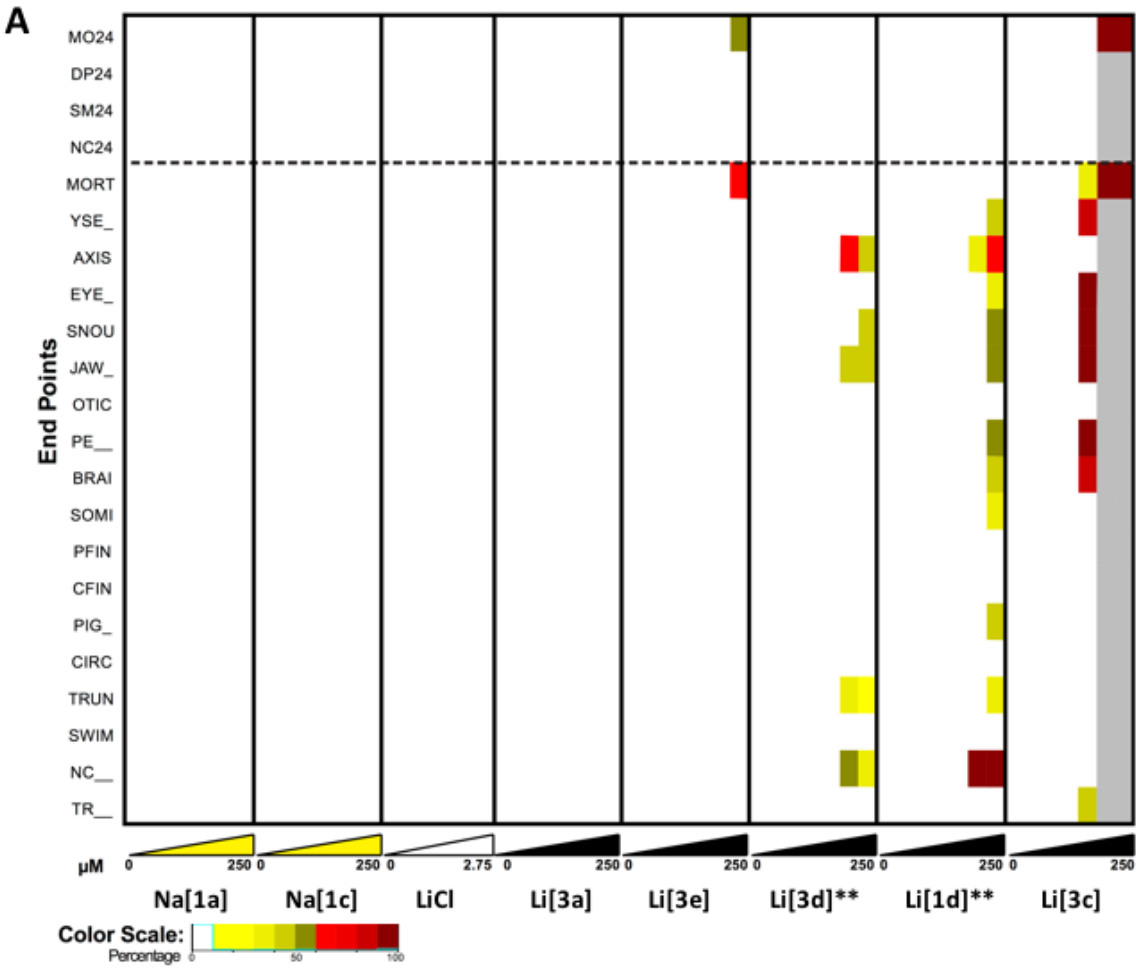

B

Na[1a]	Na[1c]	Li[3a]	Li[3e]	Li[3d]	Li[1d]	Li[3c]	LiCl
N/A	N/A	N/A	MO24†	AXIS† JAW † TRUN † NC †	NC † AXIS†	MO24† YSE † EYE † SNOU † JAW †	N/A

Figure 19. Biological responses of embryonic zebrafish after exposure to TAML catalysts. (**A**) Heatmap depicting the response of embryos exposed to each activator at 6 different concentrations. At each concentration, four and 18 endpoints were evaluated at 24 and 120 hours post fertilization (hpf), respectively. The grey bars indicate endpoints that could not be evaluated because no viable embryos were available as exposure to 50 and 250 µM Li[**3c**] resulted in 100% mortality within 24 hpf. **Denotes compounds that induced notochord distortions. (**B**) A table showing statistical significance and dose-dependent morphological malformations determined by logistic regression and denoted with a † ($p<0.001$).

Table 5. LC_{50} and EC_{50} values (in μM) generated by the Probit analysis of the data collected over 6 exposure concentrations.

TAML	LC_{50}	EC_{50}
Na[1a]	—	—
Na[1c]	—	—
Li[3a]	—	—
Li[3e]	235	245
Li[3d]	—	25.6
Li[3c]	—	32
Li[1d]	26.7	4.5

Experimental

Instrumentation

Kinetic spectrophotometric measurements were made in 1 cm plastic poly(methylmethacrylate) cuvettes on Hewlett-Packard Diode Array spectrophotometers (models 8452A and 8453) equipped with a thermostatted cell holder and automatic 8-cell positioner. ^{1}H NMR data were collected at 300 K with a Bruker Avance 300 operating at 300 MHz using DMSO-d_6 with chemical shifts reference to the residual proton DMSO peak at d = 2.5. Elemental analyses were performed by Midwest Microlab, Indianapolis, IN. Electrospray ionization mass spectra (ESI-MS) were obtained using a Finnigan MAT SSQ700 mass spectrometer with an Analytical of Branford electrospray ionization interface. ^{1}HNMR spectra were obtained using a Bruker Avance^{TM} 300 MHz spectrometer in d_6-DMSO (Cambridge Isotope Laboratories, Inc., Andover MA).

Spectrophotometric titration of **V** was performed on a Cary 5000 UV-Vis-NIR spectrophotometer in 1.0 cm quartz cells. An AUTOLAB PGSTAT 12 potentiostat-galvanostat was used for all electrochemical measurements . The working electrode, referene electrode, and auxiliary electrode were glassy carbon, SCE, and Pt wire, respectively, and were employed in a three-electrode setup. Before each measurement, the working electrode was polished with diamond paste, rinsed with HPLC grade acetone and water, and thoroughly dried. Solutions were deoxygenated by gentle sparging with argon for 20 minutes prior to measurement. Measurements were conducted under an argon pad.

Materials

Previously reported catalyst samples were prepared according to the literature procedures.[2,22,23,23] Activator **3b** was synthesized by Brendan McGee, a former Collins group member, using a modification of the **3** route in accordance with my direction. All solvents and reagents used were reagent grade and purchased from Thermofisher, Sigma Aldrich, or VWR unless otherwise noted. THF was freshly distilled from Na/benophenone ketyl under an argon atmosphere. Unless otherwise noted materials were used as received.

Collins Group Fe-TAML Nomenclature

To simplify communication between group members, a system of nomenclature has been developed based on the identity of the ligand. The ligand naming convention is as follows: the chemical symbol for and number of amido protons is listed, this is followed

by the chemical formula of the aromatic substituents of the o-phenylenediamine residue if any exist. In the case of **1** these are understood to occupy positions meta to the amino substituents. The system for **3** is more complex. If two o-phenylenediamine aromatic substituents are listed they are assumed to be appended to the carbon atoms meta to the amido nitrogens of the oxamide of the final ligand structure. If four o-phenylene diamine aromatic substituents are listed they are assumed to be appended to carbon atoms meta to the oxamide and those meta to the malonamide of the final ligand structure. The aromatic substituents are followed by the moniker assigned to the ligand structure lacking aromatic substituents. In the case of **1**, this is B. In the case of **3**, this is D. This is followed by a moniker denoting the identity of the geminal substituents appended to the carbon α to the carbonyls of the malonamide tail. The moniker assigned to dimethyl residues is '*', the most systematic moniker assigned to diethyl residues is 'Et_2', and the moniker assigned to geminal fluorine atoms is 'F_2'. For example, the ligand that is metallated to give **1a** is known as H_4B*. In the case of metallated complexes, the atomic symbol for the metal ion inserted takes the place of the amido protons. Consequently the trivial names of the catalysts referred to in this chapter are as follows: **1a** = $[FeB^*]^-$; **1b** = $[FeCl_2BF_2]^-$; **1c** = $[FeNO_2BF_2]^-$; **3a** = $[FeD^*]^-$; **3b** = $[FeCl_4D^*]^-$; **3c** = $[Fe(CN)_2D^*]^-$; **3d** = $[Fe(NO_2)_2D^*]^-$. Unfortunately, this system breaks down in the case of the seldom referred to **2** which were previously dubbed 'D'.

Synthesis of LiFe(CN)$_2$D* (3d).

i. *Tert*-butyl (2-amino-5-cyanophenyl)carbamate (**I**). A solution of Boc_2O (15 mmol, 3.27 g) in THF (40 mL) was added dropwise to a stirred solution of 3,4-

diaminobenzonitrile (15 mmol, 2.00 g) and triethylamine (15 mmol, 2.10 mL) in THF (80 mL) in a round bottomed flask at 0 °C under argon. After 24 hours, the reaction was warmed to 25 °C and de-ionized water (100 mL) was added. After separation of the organic layer, the aqueous layer was extracted with diethyl ether (3 x 100 mL). The combined organic layers were washed with an aqueous 1 M bicarbonate solution and an aqueous saturated brine solution, dried over Na_2SO_4, filtered, and concentrated *in vacuo*. The crude residue was purified by SiO_2 flash chromatography on 60 mesh gel pretreated with triethylamine (gradient elution, Hexanes:EtOAC 3:1 to EtOAC). **I** was isolated as a pale orange solid (1.961 g, 56%). ^{1}H NMR (ppm): 1.46 (s, 9H, CH_3), 5.88 (s, 2H, NH_2), 6.72 (d, J = 8.4 Hz, 1H, phenyl), 7.21 (dd, J^5_{HH}= 2.1 Hz, J^3_{HH}= 8.3 Hz, 1H, phenyl), 7.61 (d, J^5_{HH}= 2.1 Hz, 1H, phenyl) 8.43 (s, 1H, N<u>H</u>CO).

ii. Di-*tert*-butyl (((2,2-dimethylmalonyl)bis(azanediyl))bis(5-cyano-2,1-phenylene))dicarbamate (**II**). A solution of dimethylmalonyl chloride (3.44 mmol, 0.46 mL) in THF (23 mL) was added dropwise to a stirred solution of **I** (6.88 mmol, 1.604 g) and pyridine (6.88 mmol, 0.55 mL) in THF (103 mL) under argon at 25 °C. After 24 hours the reaction mixture was filtered through a fine porosity glass frit and concentrated *in vacuo* to give crude **II** used without purification. ^{1}H NMR (ppm): 1.41 (s, 18H, methyl), 1.56 (s, 6H, methyl), 7.58 (dd, J=2.1 Hz, J=8.4 Hz, 2H, phenyl), 7.79(d, J=8.4 Hz, 2H, phenyl), 7.87 (d, J=2.1 Hz, 2H), 8.93 (s, 2H, boc N<u>H</u>CO), 9.54 (s, 2H, malonyl N<u>H</u>CO).

iii. N^1,N^3-bis(2-amino-4-cyanophenyl)-2,2-dimethylmalonamide (**III**). HCl (12.1 M, 2.3 mL) was added to a stirred solution of crude **II** (50 mg) in EtOAC (16 mL) at 25 °C. The reaction was quenched by addition of the crude mixture to a vigorously stirred aqueous solution of $NaHCO_3$ (1.0 M, 50 mL) at 0 °C 20 minutes after the visible evolution of gas stopped. After 30 minutes of vigorous stirring, the organic layer was separated and the aqueous phase was extracted with EtOAC (3 x 20 mL). The combined organic layers were dried over Na_2SO_4, filtered, and concentrated *in vacuo* to yield **III** as a white solid (28 mg, 86% over 2 steps). ^{1}H NMR (ppm): 1.56 (s, 6H, CH_3), 5.34 (s, 4H, NH_2), 6.95 (dd, J=2.1Hz, J=8 Hz, 2H, phenyl), 7.05 (d, J=2.1Hz, 2H, phenyl), 7.22 (d, J=7.8 Hz, 2H, phenyl), 9.24 (s, 1H, NHCO).

iv. 15,15-Dimethyl-6,7,14,16-tetraoxo-6,7,8,13,14,15,16,17-octahydro-5*H*-dibenzo[*b*,*h*][1,4,7,10]tetraazacyclotridecine-3,10-dicarbonitrile (**IV**). A solution of oxalyl chloride (2.0 M in DCM, 0.138 mmol, 0.07 mL) in THF (14 mL) was added dropwise to a stirred solution of **III** (0.138 mmol, 50 mg) and triethylamine (0.276 mmol, 39 μL) in THF (10 mL) in a round bottom flask under argon at 25 °C. After 24 hours, the crude reaction mixture was filtered through a medium porosity glass frit and rinsed with deionized water to yield **IV** as a white solid (54 mg, 94%). ^{1}H NMR (ppm): 1.54 (s, 6H, CH_3), 7.62 (d, J=8.1 Hz, 2H, phenyl), 7.78 (dd, J=1.8 Hz, J=8.1 Hz, 2H, phenyl), 7.96 (d, J=1.8 Hz, 2H, phenyl), 10.03 (s, 1H, oxalyl NHCO), 10.19 (s, 1H, malonyl NHCO). Anal. Calcd (found) for $C_{21}H_{16}N_6O_4$: C, 60.57 (56.72); H, 3.87 (4.25); N, 20.18 (17.72). This elemental analysis likely reflects the presence of

solvents or Et_3NHCl which are difficult to remove due to the insolubility of **IV**, similar difficulties were encountered in purification of the **3e** analogue.

v. $LiFe(CN)_2D^*$ (**V**). A solution of $LiN(Si(CH_3)_3)_2$ (1.0 M in hexanes, 0.53 mmol, 0.53 mL) in THF (0.64 mL) was added to a rapidly stirred suspension of **IV** (0.12 mmol, 50 mg) in THF (15 mL) at 25 °C under argon resulting in a homogeneous light orange solution. After 10 minutes, a solution of $FeCl_3$ (0.132 mmol, 21.4 mg) in THF (11.36 mL) was introduced into the reaction mixture to give a dark brown solution. After 15 minutes, the reaction was opened to the air in the room and allowed to stir for 30 minutes. The solution was concentrated *in vacuo* resulting in a dark brown solid to which HPLC grade water (7 mL) was added. The solution was filtered and concentrated in vacuo. The crude residue was purified by reverse phase flash chromatography on C18 silica gel (gradient elution HPLC grade H_2O to 10:1 HPLC H_2O: HPLC MeOH) to give **V** (17 mg, 30%) as the lithium salt. ESI-MS neg. mode: m/z=468.2, Anal. Calcd (found) for $C_{21}H_{12}FeLiN_6O_4$: C, 53.08 (45.88); H, 2.55 (3.35); N, 17.69 (13.89) also likely solvated. IR. $\varepsilon_{375,\ MeOH} = 4850 \pm 50\ M^{-1}\ cm^{-1}$; $\varepsilon_{425,\ MeOH} = 2480 \pm M^{-1}\ cm^{-1}$.

vi. $Ph_4PFe(CN)_2D^*$ and $PNPFe(CN)_2D^*$. Cation methathesis of **V** to give both the Ph_4P^+ and PNP^+ salts was performed as has been reported. In both cases, slow evaporation of MeOH from an aqueous solution gave red needles approximately 0.25 cm in length.

Kinetic Studies of TAML catalyzed Orange II Oxidation by H_2O_2.

Stock solutions of **1** and **3** (5×10^{-6} M) in HPLC grade methanol were prepared. A stock solution of Orange II (4.5×10^{-5} M) in HPLC grade water was prepared. Hydrogen peroxide solutions (2×10^{-2} M) were prepared in 0.01 M phosphate buffer. Solutions of hydrogen peroxide were standardized daily by measuring the absorbance at 230 nm (ε = 72.8 $M^{-1}cm^{-1}$) and adjusted to pH 7. Aliquots of the Orange II and catalyst stock solutions were added to a polymethylmethacrylate UV-vis cuvette followed by 0.01 M pH 7 phosphate buffer to reach a final volume of 1 mL. An aliquot of the Orange II solution was added. The reaction was initiated by addition of an aliquot of the hydrogen peroxide stock solution. The cell holder was thermostatted at 25 °C. Initial rates of Orange II oxidation were calculated using the pH 7 extinction coefficient for Orange II of 18,100 M^{-1} cm^{-1}. All data points are the average of at least three measurements. Calculations of the initial rates and of the rate constants k_I, and k_{II} were performed using a Sigma Plot 2010 package (version 12.0).

Summary

The electrochemical and kinetic k_I data presented in this chapter provides admittedly limited evidence of an equilibrium binding of H_2O_2 to the resting catalyst which precedes catalyst activation not explicitly accounted for by the existing TAML mechanism. Further evidence is noted in Chapter 3 This is the subject of ongoing studies undertaken by Ms. Liang Tang and designed to determine the precise sequence of events leading to catalyst activation. These have revealed a very weak inhibition of **1** catalyst activation by nonaqueous solvents that are not oxidized by Ac to any great extent. The data, which

indicate that only 1 solvent molecule is necessary to intercept the resting catalyst and illuminate novel subtleties in the catalyst activation process including more substantial evidence of an equilibrium binding of H_2O_2 that precedes catalyst activation. This is sensible as H_2O_2 must gain access to the active site somehow and the concentration of H_2O_2 significantly less than that of H_2O under most TAML application conditions. Consequently, the diaqua form should dominate pH 7 resting catalyst speciation. We have interpreted this as evidence of one of the following possibilities concerning the speciation of the resting catalyst in pH 7 aqueous solutions at 25 °C: (i) that resting TAML catalysts are more accurately formulated as 5 coordinate complexes under these conditions as was found for Fe-TAMLs having an axial chloride ligand in which a second water molecule was considered to be held in place by the lattice of the crystal structure discussed Chapter 1, (ii) that the two axial sites of 6 coordinate resting TAML catalysts are inequivalent such that only binding to one is productive, likely that of the out of plane iron atom, or (iii) the two labile sites are cis and the observed effect is a consequence of steric hindrance. This work may lead to a reinterpretation of the observed k_I pH bell curve. We are examining this further and are optimistic that it will be the subject of a future publication.

In this chapter, the body of foundational mechanistic work involving TAML activators was first reviewed and then the behavior of a new catalyst was assessed. The cyano groups were chosen as ligand substituents because, like nitro groups, they are in among the strongest electron-withdrawing substituents comprised of biochemically common elements that the synthetic chemist can use deploy for controlling catalyst reactivities. Thus, a major incentive was to prepare TAML activators for study with

cyano in place of nitro substituents as insurance against any regulation or toxicity barriers that might arise if TAML catalysts with electron withdrawing substituents were to be deployed. Furthermore, the nitrile group has never been incorporated into an iron tetra-amido macrocyclic ligand. A new iron tetra-amido macrocyclic ligand (Fe-TAML), **3d**, has been synthesized following the procedure used to generate **3** which has yielded the most reactive TAML catalyst to date, **3e**. Since neutral pH is a preferred condition for to the primary TAML application of aqueous micropollutant removal, the neutral pH reactivity of this activator as well as that of **3a**, **3b**, and **3d** were determined for comparison with the known reactivity of **3e**. At pH 7 Attempts to determine the pKa values of the axial water molecules of $[Fe(CN)_2D^*]^-$ anion in 0.01 M phosphate reveal an instability of the system at high pH likely due to hydrolysis of at least one nitrile group. The electrochemistry of all four members of the **3** generation of TAML activators has been studied. Catalysts having the **3** parent ligand system require electron withdrawing groups at the phenyl positions in order to attain high hydrolytic stability. Zebrafish assays are performed on a variety of TAML activators in order to assess the phenyl substituents that endow the final catalyst with increased toxicity. The nitrile group is found to activate TAML catalysts in accordance with its known electron withdrawing properties, be hydrolytically unstable and, of particular significance to commercial development, has been found to endow the final catalyst with greater toxicity than the nitro group. Nitro bearing TAML activators of the **1** and **3** generations have passed zebrafish developmental assays without the detection of significant low dose adverse effects. For this reason, further study of nitrile bearing activators is not recommended.

References

(1) Collins, T. J.; Denardo, M. A.; Warner, G. R. 2015.
(2) Ellis, W. C.; Tran, C. T.; Denardo, M. A.; Fischer, A.; Ryabov, A. D.; Collins, T. J. *Journal of the American Chemical Society* **2009**, *131*, 18052.
(3) Ellis, W. C.; Tran, C. T.; Roy, R.; Rusten, M.; Fischer, A.; Ryabov, A. D.; Blumberg, B.; Collins, T. J. *Journal of the American Chemical Society* **2010**, *132*, 9774.
(4) Chahbane, N.; Popescu, D.-L.; Mitchell, D. A.; Chanda, A.; Lenoir, D.; Ryabov, A. D.; Schramm, K.-W.; Collins, T. J. *Green Chemistry* **2007**, *9*, 49.
(5) Polshin, V.; Popescu, D.-L.; Fischer, A.; Chanda, A.; Horner, D. C.; Beach, E. S.; Henry, J.; Qian, Y.-L.; Horwitz, C. P.; Lente, G.; Fabian, I.; Münck, E.; Bominaar, E. L.; Ryabov, A. D.; Collins, T. J. *Journal of the American Chemical Society* **2008**, *130*, 4497.
(6) Popescu, D.-L.; Chanda, A.; Stadler, M. J.; Mondal, S.; Tehranchi, J.; Ryabov, A. D.; Collins, T. J. *Journal of the American Chemical Society* **2008**, *130*, 12260.
(7) Ghosh, A.; Mitchell, D. A.; Chanda, A.; Ryabov, A. D.; Popescu, D. L.; Upham, E. C.; Collins, G. J.; Collins, T. J. *Journal of the American Chemical Society* **2008**, *130*, 15116.
(8) Ghosh, A.; Ryabov, A. D.; Mayer, S. M.; Horner, D. C.; Prasuhn, D. E.; Sen Gupta, S.; Vuocolo, L.; Culver, C.; Hendrich, M. P.; Rickard, C. E. F.; Norman, R. E.; Horwitz, C. P.; Collins, T. J. *Journal of the American Chemical Society* **2003**, *125*, 12378.
(9) Chanda, A.; Ryabov, A. D.; Mondal, S.; Alexandrova, L.; Ghosh, A.; Hangun-Balkir, Y.; Horwitz, C. P.; Collins, T. J. *Chemistry – A European Journal* **2006**, *12*, 9336.
(10) Hammett, L. P. *Journal of the American Chemical Society* **1937**, *59*, 96.
(11) McDaniel, D. H.; Brown, H. C. *The Journal of Organic Chemistry* **1958**, *23*, 420.
(12) Hansch, C.; Leo, A.; Taft, R. W. *Chemical Reviews* **1991**, *91*, 165.
(13) Schreck, J. O. *Journal of Chemical Education* **1971**, *48*, 103.
(14) Tang, L., Carnegie Mellon.
(15) Ellis, W. C., Carnegie Mellon University.
(16) Truong, L.; DeNardo, M. A.; Kundu, S.; Collins, T. J.; Tanguay, R. L. *Green Chemistry* **2013**, *15*, 2339.
(17) McCollum, C. W.; Ducharme, N. A.; Bondesson, M.; Gustafsson, J.-A. *Birth Defects Research Part C: Embryo Today: Reviews* **2011**, *93*, 67.
(18) Truong, L.; Tilton, S. C.; Zaikova, T.; Richman, E.; Waters, K. M.; Hutchison, J. E.; Tanguay, R. L. *Nanotoxicology* **2013**, *7*, 192.
(19) Eimon, P. M.; Rubinstein, A. L. *Expert Opinion on Drug Metabolism & Toxicology* **2009**, *5*, 393.
(20) Bols, N. C.; Boliska, S. A.; Dixon, D. G.; Hodson, P. V.; Kaiser, K. L. E. *Aquatic Toxicology* **1985**, *6*, 147.
(21) Eldred, D. V.; Weikel, C. L.; Jurs, P. C.; Kaiser, K. L. E. *Chemical Research in Toxicology* **1999**, *12*, 670.

(22) Horwitz, C. P.; Ghosh, A.; USPTO, Ed.; Carnegie Mellon University: United States, 2004.
(23) Sullivan, S. Z.; Ghosh, A.; Biris, A. S.; Pulla, S.; Brezden, A. M.; Collom, S. L.; Woods, R. M.; Munshi, P.; Schnackenberg, L.; Pierce, B. S.; Kannarpady, G. K. *Chemical Physics Letters* **2010**, *498*, 359.

Chapter 3

The Systematic Evaluation of pH 7 TAML Reactivities

Introduction

TAML activators shown in Figure 1 catalyze the oxidation of substrates (S) by an oxidant, which is usually H_2O_2, according to the sequence of events shown in Figure 2. In addition to oxidizing substrates, the active catalyst (Ac) can also undergo irreversible inactivation process(es) represented by k_i in Figure 2. TAML development has long focused on catalyst design to obviate decomposition processes. A short review of the qualitative and quantitative studies of catalyst inactivation as well as the speciation of the active catalysts is merited as this chapter largely concerns quantitative studies of the neutral pH inactivation of TAML catalysts in order to determine both the nature of this process as well as its relationship to catalyst structure under the most desirable conditions for the major TAML application of water treatment.

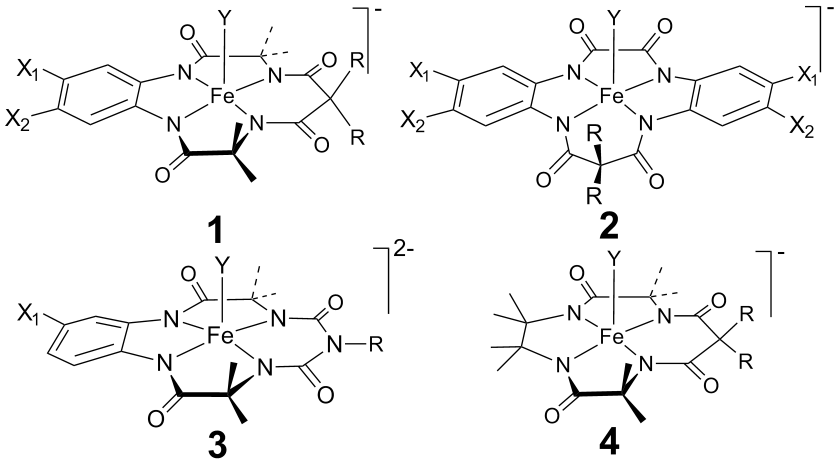

Figure 1. Structures of the catalysts referred to in Chapter 3. See table 2 for X, R.

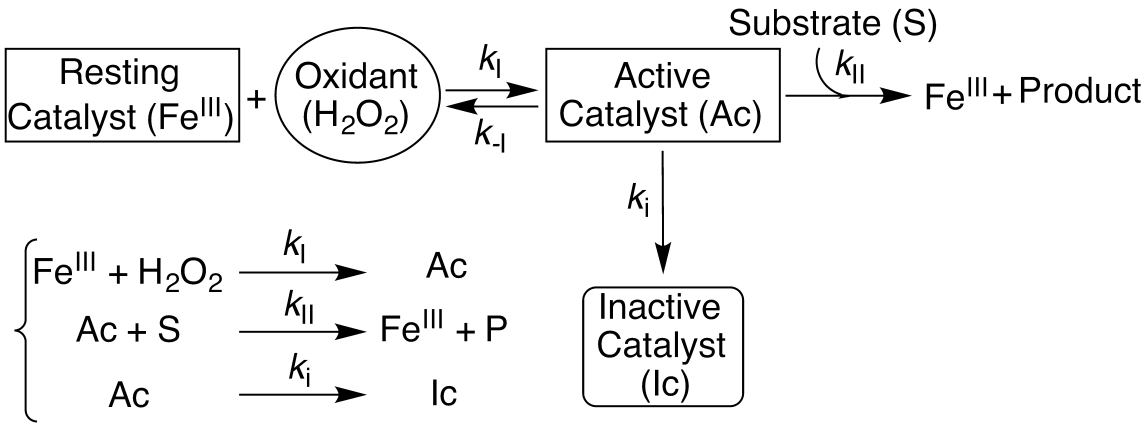

Figure 2. Elementary chemical steps involved in TAML catalysis and the chemical expressions that represent them.

Qualitative Studies of TAML Inactivation

The earliest published examples of this work include the examination of the electrochemical decomposition products of the osmium complexes of the PAC ligand that led to replacement of a ligand ethane unit with the carbons of aromatic ring, the incorporation of Margerum's method of blocking β hydrogen abstraction which led to peralkylation of the ligand structure, and observations of hydrolytic instability of 5'6'5'6 chelate ring macrocycles that led to the design of ligands forming 5'5'5'6 chelate ring systems. These were followed by studies of the Fe^{V} decomposition products of two **1** having the structure shown in Chart 1 with $X_1/X_2/R$ of Cl/Cl/Et and Cl/Cl/Me and the pH 10 pinacyanol chloride bleaching experiments which indicated that enhanced resistance to intramolecular catalyst inactivation due to hydantoin ring formation could be attained by substitution of the malonamide ethyl groups with methyl groups or fluorine atoms. The latter work is the first published study of TAML inactivation in functioning aqueous catalysis. The work compared the pH 10 reactivities of the previously mentioned two **1** relative catalytic efficiencies in terms of the rates and amount of dye oxidized by the

addition of successive 1.2×10^{-5} M aliquots of pinacyanol chloride dye to solutions containing 4.3×10^{-7} M catalyst and an excess of oxidant.

Quantitative Studies of pH 11 TAML Catalyst Inactivation

In addition to the qualitative studies reviewed above and those covered more deeply in Chapter 1, an approach for quantifying k_i was developed.[1] The method relies upon setting up an observable competition between substrate oxidation and catalyst inactivation. This is accomplished by measuring the initial rate of substrate consumption, *v*, under conditions where $k_{\mathrm{I}}[\mathrm{H_2O_2}] \gg k_{-\mathrm{I}} + k_{\mathrm{II}}[\mathrm{S}]$. Here, the general form for substrate consumption by a TAML activator under aqueous turnover conditions, discussed in Chapter 2 and depicted in eq 1, can be represented by the simplified form eq 2. As indicated by eq 2, under these conditions substrate oxidation is rate determining. However, as discussed in Chapter 2, for most TAML processes $k_{\mathrm{I}}[\mathrm{H_2O_2}] \ll$ or $\sim k_{-\mathrm{I}} + k_{\mathrm{II}}[\mathrm{S}]$ such that catalyst activation and not substrate oxidation is rate determining. Fortunately, experimental conditions can be chosen to switch from rate determining catalyst activation to rate determining substrate oxidation. Systems for which *v* is accurately modeled by eq 2 incorporate some or all of the following traits; (*i*) the substrate is very difficult to oxidize resulting in low values of k_{II}, (*ii*) the solution pH is greater than 10 resulting in large values of k_{I} for most activators due to the bell shaped k_{I}/pH dependence, (*iii*) high concentrations of H_2O_2 are employed to ensure the $k_{\mathrm{I}}[H_2O_2]$ term dominates the denominator of eq 1, and (*iv*) low high concentrations of S are employed. Consequently, these first quantitative experiments were performed at pH 11 with the difficult to oxidize dye substrate, Safranine O.

$$v = \frac{k_I k_{II}[H_2O_2][S]}{k_{-I}+k_I[H_2O_2]+k_{II}[S]} Fe_{Tot} \quad (1)$$

$$v = k_{II}[S]Fe_{Tot} \quad (2)$$

The low catalyst concentration of 7.5×10^{-8} M was chosen to increase the probability that inactivation processes would be unimolecular in catalyst as those that are bimolecular in catalyst should be very slow when $[Fe^{III}] < 10^{-6}$ M. Under these conditions, the inactivation of Ac can be considered to be modeled by eq 3 which gives eq 4 when integrated and evaluated with $[Ac]_0 = [Fe^{III}]$ and $[Ac]_\infty = 0$. Substitution into eq 2 with $v = -\frac{d[S]}{dt} = -\frac{d(D_{tot}-x)}{dt}$, where D_{tot} represents the initial concentration of dye and x is the amount of dye bleached at time t, gives eq 5. Since arriving at eq 5 requires use of eq 2, eq 5 was thought to be limited to systems that are accurately modeled by eq 2 indicating that the tested system should incorporate the features discussed above. Integration of eq 5 and evaluation with x_∞ as the concentration of dye bleached at time t_∞ gives eq 6 which is equivalent to eq 7 since the absorbance A at time t is $(D_{tot} - x)\varepsilon$ and $t = \infty$ is $(D_{tot} - x_\infty)\varepsilon$.

$$-\frac{d[Ac]}{dt} = k_i[Ac] \quad (3)$$

$$[Ac] = [Fe^{III}]_{tot}e^{-k_i t} \quad (4)$$

$$-\frac{d(D_{tot}-x)}{dt} = k_{II}(D_{tot} - x)[Fe^{III}]_{tot}e^{-k_i t} \quad (5)$$

$$\ln\left[\ln\left(\frac{(D_{tot}-x)}{(D_{tot}-x_\infty)}\right)\right] = \ln\left(\frac{k_{II}}{k_i}[Fe^{III}]_{tot}\right) - k_i t \quad (6)$$

$$\ln\left[\ln\left(\frac{A_t}{A_\infty}\right)\right] = \ln\left(\frac{k_{II}}{k_i}[Fe^{III}]_{tot}\right) - k_i t \quad (7)$$

Equation 7 was applied to incomplete UV traces of catalysis of Safranine O oxidation by 0.012 M H_2O_2 at pH 11 in 25 °C, 0.01 M Phosphate buffer by a series of **1** having $X_1/X_2/R$ of Cl/Cl/CH_2CH_3, H/H/CH_2CH_2 (fused cyclopropyl), H/H/Me, and Cl/Cl/F to give linear forms. Values of k_{II} and k_i for each catalyst were obtained from the slope and intercept of these linear forms. Comparing these pairs of values for each catalyst collected at any one temperature reveals that as the k_{II} for a catalyst increases, so does the k_i . This is a strong indication that substitution of the malonamide methylene unit neither halts nor negatively impacts pH 11 catalyst inactivation. These results contradict those qualitatively observed in the pH 10 pinacyanol chloride studies which reports decreased rates of inactivation on substitution of malonamide methyl groups for ethyl. Analysis of k_{II} and k_i data for this same set of catalysts collected over a temperature range of 13-60 °C under the same conditions as above found large negative values of $\Delta S_i^{\ddagger}$ indicative of a clean second order inactivation process that proceeds via a highly ordered transition state.

The dependence of the **1d** (H/H/Me) and **1f** (NO_2/H/Me) inactivation rate constant k_i on [H_2O_2] over a range of 0.012-0.12 M was determined and found to be linear. In both cases, fitting of a linear model to the data gave positive slopes and nonzero y-intercepts. From this it was concluded that the observed inactivation is the sum an [H_2O_2] independent process, $k_{i\alpha}$, and a process that is first order in H_2O_2, $k_{i\beta}$. Both the **1f** (NO_2/H/Me) $k_{i\alpha}$ and $k_{i\beta}$ values were found to be greater than those of **1d** (H/H/Me) as was the **1f** (NO_2/H/Me) k_{II} value indicating that substitution of the phenylenediamine residue with electron withdrawing groups gives catalyst which both oxidize substrates and

undergo inactivation more quickly. It was concluded that the 0.012 M [H_2O_2] employed in the variable temperature studies was sufficiently low to ignore contributions from the $k_{i\beta}$ pathway. Consequently, the $\Delta S_i^{\ddagger}$ value was considered to reflect the nature of the $k_{i\alpha}$ pathway, which was decided to be an intramolecular inactivation.

A linear free energy relationship (LFER) was constructed relating the k_{II} and k_i values for catalysis of the oxidation of Safranine O by 0.012 M H_2O_2 by several **1** catalysts including **1b** (Me/Me/Me) , **1d** (H/H/Me), **1e** (CO_2Me/H/Me), and **1f** (NO_2/H/Me) as well as those having X_1/X_2/R of Cl/Cl/CH_2CH_3, Cl/Cl/CH_3, CH_3/H/CH_3, COOH/H/CH_3, and CONH$(CH_2)_2N^+(CH_3)_3$. The line of best fit to this LFER was found to have a slope of ~ -1 when **1d** (H/H/Me) was excluded. From this result it was concluded that the substitution of the **1** phenylenediamine with electron withdrawing groups, which was known to increase k_{II}, decreases k_i. Consequently, the aromatic ring of the phenlyenediamine residue was considered to be a site of oxidative inactivation.

The dependence of **1d** (H/H/Me) k_i on pH in the region of 10–12 was also determined in this system and found to indicate that k_i is only weakly dependent on pH here. Surprisingly, treatment of incomplete bleaching curves for pH 11 **1d** (H/H/Me) and **1h** (Cl/Cl/F) catalysis of the oxidation of Orange II, a different dye substrate, by H_2O_2 using eq 7 found similar k_i values to those obtained in the oxidation of Safranine O indicating that the observed inactivation is not dependent on the structure of the substrate.

From the sum of this work it was concluded that at pH 11 $k_{i\alpha}$ involves an intramolecular suicide inactivation process, $k_{i\alpha}$, and one which involves involves H_2O_2 attack of Ac, $k_{i\beta}$. This work overturns previous inactivation work as the overall rate of catalyst inactivation is not observed to depend on the identity of the substituents of the **1**

malonamide methylene unit. This study concluded that substitution of the phenylenediamine residue with electron-withdrawing groups, known to increase k_{II}, retards k_i. Unfortunately, this method was considered to be restricted to conditions under which eq 2 applies. Consequently, it could not be used to determine k_i values at neutral pH, that preferred for the application of water treatment.

The Speciation of Ac

Since k_i and k_{II} pathways both involve Ac, recent progress made towards understanding the speciation of Ac is worthy of examination. A study of the **1d** (H/H/Me) and **1h** (Cl/Cl/F) catalyzed oxidation of $Fe^{II}(CN)_6^{4-}$ to $Fe^{III}(CN)_6^{3-}$ by H_2O_2 in 0.01 M Phosphate buffer at 25 °C over the pH range 7-12 has revealed the operation of four Fe^{IV} intermediates related by the loss or gain of a proton or protons as shown in Figure 3 below.[2] This speciation manifests itself in the form of a distorted, bell-shaped k_{II}/pH dependence with four plateaus indicative of the operation of four agents. Since H_2O_2 is a 2 e^- oxidant, the first Ac produced is thought to be a formally Fe^V intermediate.. However, its reduction to the reported Fe^{IV} species is thought to be so rapid as to be kinetically undetectable. As a result, the bell-shaped dependence has been determined to reflect the speciation of a less reactive Fe^{IV} species as the observed reduction of this species to Rc should be slower and rate-determining..Curiously, oxidations by species **C** have been observed to be the most rapid despite its larger negative charge than **A** or **B**. Calculations have found this to be attributable to its solvation.

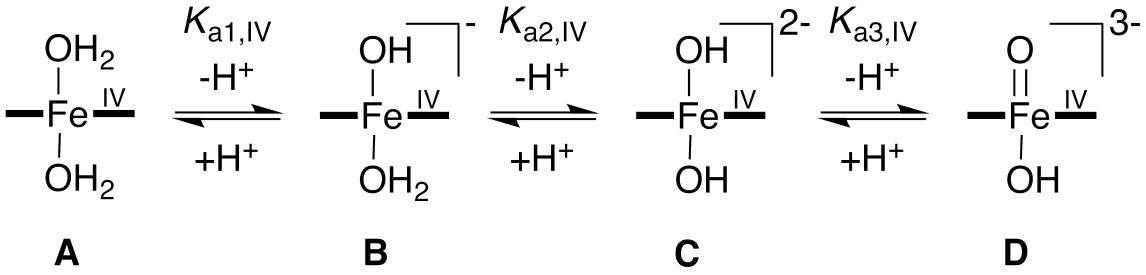

Figure 3. Proposed speciation of the Fe^{IV} Ac in catalysis of $Fe^{II}(CN)_6^{4-}$ at 25 °C in 0.01 M Phosphate buffer over the pH range of 7–12.

This Work

The above works are a representative sampling of the scale and depth of the mechanistic studies of TAML activators conducted by the Institute for Green Science (IGS) over the past fifteen years. This work has made massive contributions to catalysis and advanced chemists understanding of how oxidation catalysts decompose under operating conditions.[3] We have been able to make such contributions because TAML activators uniquely display long lifetimes, high reactivity, and wide applicability. The IGS has also heavily contributed to the development of the field of oxidation catalysis under ultra-dilute conditions including publication of an impressively fast **1g** (NO_2/H/Me) catalysis of ethinyl estradiol (EE2) oxidation at catalyst concentrations as low as 10 nM,[4] While these lab studies are not real world where other pollutants are also present, it is nevertheless significant to note that 1 kg of **1g** has been determined to be sufficient to remove trace EE2 from ca. 200,000 tonnes of water. Such a performance is unprecedented in the annals of chemistry. However, **1g** does undergo inactivation that cannot be accounted for by the catalyst design protocol proposed by Dr. Collins[25,6]that led to TAML catalysts. The goal of the work presented herein, advancing this long established and reliable set of guidelines, was formidable. However, it was estimated that

such an achievement could push treatment of EE2, for example, to perhaps 1 million tonnes or more, potentially a substantial contribution to water treatment and possibly to society.

The principal barrier to addressing this challenge is conducting detailed studies of catalyst inactivation at the extremely low concentrations involved in the real world relevant processes. Because the catalyst concentrations of interest are so low, it is virtually impossible to examine this problem using the approach that led to TAML activators, namely characterizing catalyst degradation species to identify sites of decomposition vulnerability. Consequently, in this work the collaborative refinement of the quantitative kinetic approach was undertaken that has yielded transformational insight into oxidation catalyst design. The approach is based on new kinetic tool developed through collaboration between the IGS and the mathematical group of Maria Emelianenko at George Mason University.[7] The key kinetic tool, eq 8, permits the easy evaluation of k_i under any conditions including those intended for water treatment, at pH 7 with nanomolar catalyst concentrations. The approach involves studying a broad range of TAML activators represented by **1**-**4**, including one I designed specifically for this purpose, mechanistically to evaluate and correlate the rate constants k_I, k_{II} and k_i, that we identify as critical "Technical Performance Parameters". I undertook this study to correlate the relative performances of fifteen different TAML activators in order to confirm my intuitive assessment of the catalyst structural feature accountable for inactivation. I then completed further studies of the H_2O_2 and OH^- dependences of k_i to confirm this assignment and lend support for my theory of the mechanism of the process. These have enabled the development of new insight into how TAML activators both

undergo activation and decompose under operating conditions, which in turn has led to a new series of catalytic compositions of matter that are far superior to TAML activators.

The results achieved have provided a basis for comprehending the role of a completely non-obvious and long dismissed as relevant route of catalyst degradation which has been in play and, under the presented conditions, appears to make a larger contribution to the catalyst inactivation process than the prevailing hypothesis of oxidative degradation. This is quite fortunate as design against oxidative degradation had already run its course and was no longer limiting the Group's ability to get longer lived catalysts even as much more reactive catalysts were being obtained. This insight has led us to file a new composition of matter patent application on which I am an inventor with Dr. Collins and one other colleague. Several of the new compositions have been obtained and these are far superior to TAML activators in combined technical, cost and environmental performances. In the interests of further patenting, some details have been excluded from this discussion.

Results and Discussion

Synthesis of TAML Activators

Samples of **2a**, **2c**, **2d** and **2e** were synthesized according to literature procedures.[7-10] Activator **2b** was synthesized by Brendan McGee, a former Collins group member, using a modification of the **2a** route suggested by me.

Development of a Mathematical Treatment for the Simultaneous Determination of k_I, k_{II}, and k_i From a Minimal Data Set

Since eq 2 does not accurately model TAML systems under the conditions that are valuable for most applications, an unrestricted model for the determination of k_i was sought by Dr. Ryabov. The resulting methodology would prove to be especially important for understanding catalyst design for water purification at near neutral pH where k_I plays a significant role in the rate of substrate oxidation. Such a model must incorporate the mathematically challenging system of all three processes, k_I, k_{II}, and k_i, depicted in Figure 2. Dr. Ryabov initiated a collaborative effort with George Mason University mathematicians Dr. Emelianenko and her student Diego Torrejon to do so. I coauthored a recent report of these collaborative studies which appeared in the Journal of Mathematical Chemistry. [7] This collaboration yielded eq 8 which allows k_i to be determined under any one set of conditions provided (*i*) the oxidant is employed in excess of that necessary for substrate S oxidation ([Oxidant] ≫ [S]), (*ii*) S_∞, the concentration of substrate when its consumption ceases, is greater than zero, and (*iii*) k_{II}, the initial concentration of substrate S_0, and S_∞ are known.[7]

$$\ln\left(\frac{S_0}{S_\infty}\right) = \frac{k_{II}}{k_i}[Fe^{III}]_{tot} \qquad (8)$$

In addition to eq 8, this collaboration yielded a general procedure for the estimation of k_I, k_{II}, and k_i from at least three kinetic traces of incomplete substrate oxidation collected at different $[H_2O_2]$. First, the value of $R = \ln(S_0/S_\infty)$ is calculated for each kinetic trace. Then each trace is fit to eq 9 to obtain M_1 values. These M_1 values are

used to construct a plot of M_1^{-1} versus $[H_2O_2]^{-1}$. The slope of the line of best fit to the M_1^{-1}/H_2O_2 data is M_2. The average of the k_I values obtained for each kinetic trace using eq 10 is an estimate of k_I. The average of the k_i values obtained from each kinetic trace using eq 11 is an estimate of k_i. Finally, the average of the k_{II} values obtained from eq 8 is an estimate of k_{II}.

$$\ln\left(\ln\frac{S_t}{S_\infty}\right) = \ln(R) - M_1 t \quad (9)$$

$$k_I = \frac{M_1[H_2O_2]}{[H_2O_2]-M_1M_2} \quad (10)$$

As reported in the publication, for **2d**, the predicted linear M_1^{-1}/H_2O_2 plots such as that shown in Fig. 4A were indeed observed for pH 7 catalysis of the oxidation of Orange II in 0.01 M Phosphate at 25 °C. I then took it upon myself to investigate apply the model to every TAML activator on hand. Linear linear M_1^{-1}/H_2O_2 plots were also observed for activators **1b**, **1c**, **2c**, and **2e**. The values of k_I, k_{II}, and k_i for these estimated by this mathematical approach are given in Table 1. However, nonlinear M_1^{-1}/H_2O_2 plots such as that shown in Fig. 4B were found for **1d-h**. The behavior of these activators is not well modeled by the mathematical approach. I was able to discern the source of these deviations through examination of the data in Fig. 4 and consideration of eq 11 which defines M_1 as a function of k_I, k_{II}, and k_i. Since both **1f** and **2e** have been found to follow the same mechanism of catalyst activation, it is reasonable to conclude that k_I is not the source of the deviations. Since substrate oxidation by the Ac of both are known to follow the same dependence on [S] and are independent of $[H_2O_2]$, k_{II} is an unlikely candidate. Since the same substrate and H_2O_2 stock solutions were employed at the measured

concentrations, neither H_2O_2 nor S_0 are likely to be accountable for the observed behavior. This leaves k_i as the most likely source. The model treats k_i as an H_2O_2 independent process. As a result, the rates of inactivation of the catalysts giving linear plots such as that shown in Fig. 4A must be independent of $[H_2O_2]$ or linear functions of it. For those activators which display a linear dependence of k_i on $[H_2O_2]$, then the rate constants estimated by this model can be expected to stray from the true values since the system cannot account for these contributions. Consequently, the deviations from linearity shown in Fig. 4B observed for **1d-h** must derive from nonlinear pH 7 k_i dependences on $[H_2O_2]$. Unfortunately, this means that the model should not be applied to the behavior of these activators, and may introduce error into estimates of k_I, k_{II}, and k_i for those to which it does apply. It may be possible to remedy this through further refinement of the model.

$$M_1 = \frac{k_I k_i [H_2O_2]}{k_I [H_2O_2] + k_i + k_{II} S_0} \quad (11)$$

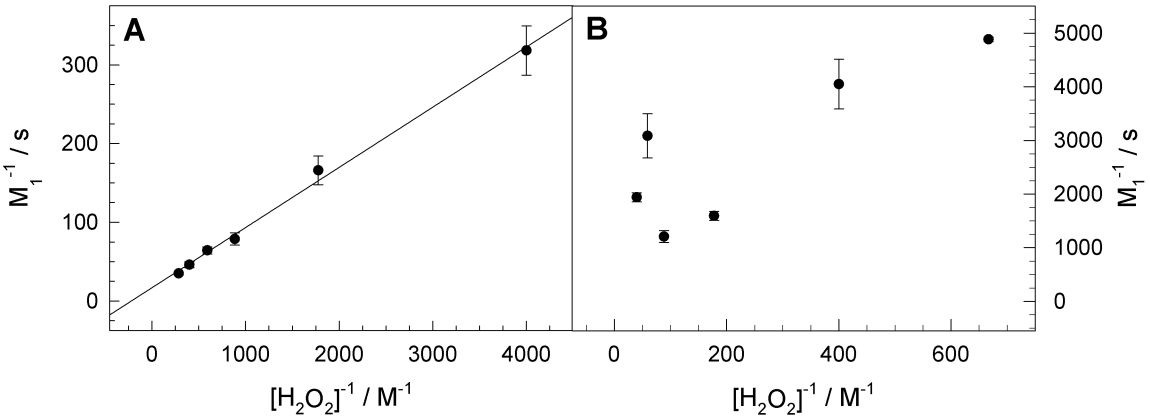

Figure 4. Double reciprocal plots of the slopes of dependence of M_1^{-1} on $[H_2O_2]^{-1}$ in the pH **7** oxidation of Orange II by H_2O_2 in 0.01 M Phosphate buffer at 25 C catalyzed by (**A**) **2e** and (**B**) **1f**.

Table 1. Rate constants (k_I and k_{II} units are $M^{-1}s^{-1}$, k_i units are s^{-1}) obtained using the Mathematical Approach for the neutral pH Fe^{III}-TAML catalyzed bleaching of Orange II by H_2O_2 at 25 °C in 0.01 M phosphate buffer.

Rc	$X_1/X_2/R$	$10^{-1} \times k_I$	$10^{-3} \times k_{II}$	$10^{4} \times k_i$
1b	Me/Me/Me	3.3±0.3	15±2	5.5±0.6
1c	NH_2/H/Me	0.34±0.02	1.9±0.2	5.5±0.4
1d	H/H/Me	N/A	N/A	N/A
1e	CO_2Me/H/Me	N/A	N/A	N/A
1f	NO_2/H/Me	N/A	N/A	N/A
1g	NO_2/H/F	N/A	N/A	N/A
1h	Cl/Cl/F	N/A	N/A	N/A
2c	Cl/Cl/Me	52±9	110±20	190±10
2d	CN/H/Me	63±5	220±50	160±30
2e	NO_2/H/Me	210±40	460±90	640±80

Determination of the Rate Constants

It occurred to me that while the procedure for estimating k_I and k_{II} from the mathematical approach may not apply to the behavior of all TAML activators, eq 8 and the method for obtaining very accurate k_I and k_{II} values discussed in Chapter 2 do. As a result, these methods were used to obtain the rate constants k_I, k_{II}, and k_i for TAML catalysis of Orange II oxidation by H_2O_2 in 0.01 M phosphate buffer at pH 7 by the **1** and **2** activators shown in Table 2 of the pH 7 parameters. Activator **4** and a rough outline of its synthetic preparation were conceived of by me for this study then implemented by a fellow Collins Group member, Matt Mills who also determined k_I, k_{II}, and k_i for this activator using this approach. Interpretation of these results has significantly advanced our understanding of the catalytic cycle. The **3** data were similarly obtained in a subsequent study and lend further weight to the conclusions drawn from the **1**, **2**, and **4** data.[11] The earlier publication date of this work reflects our decision to delay publication while drafting a patent application.

Table 2. Rate constants and redox potentials (k_I and k_{II} units are $M^{-1}s^{-1}$, k_i units are s^{-1}, E^o_1 units are mV) for the neutral pH Fe^{III}-TAML catalyzed bleaching of Orange II by H_2O_2 at 25 °C at pH 7 in 0.01 M phosphate buffer.

Rc	$X_1/X_2/R$	$10^{-1} \times k_I$	$10^{-3} \times k_{II}$	$10^4 \times k_i$	$n \times \sigma_{m+p}$	E_1
1a[12]	H/H/Et	0.18±0.01	2.8±0.1	0.9±0.1	—	
1b[12]	Me/Me/Me	4.9±0.3	9±0.5	4.2±0.1	-0.478[13]	440[14]
1c[12]	NH_2/H/Me	2.8±0.2	4.2±0.2	11.5±0.7	-0.821[13]	
1d[12]	H/H/Me	3.14±0.01	4.95±0.02	3.0±0.1	0.000	760[14]
1e[12]	CO_2Me/H/Me	3.8±0.1	7.3±0.1	1.1±0.1	+0.7	903[14]
1f[12]	NO_2/H/Me	15.2±0.5	27±2	3.4±0.2	+1.980[13]	745[14]
1g[12]	NO_2/H/F	35.0±0.2	41±1	11±3	—	
1h	Cl/Cl/F	36.1±0.1	120±10	25±0.3	—	1046[14]
1i	Cl/Cl/Et	—	—	—	—	—
1j[12]	Cl/Cl/Me	—	—	—	—	—
2a	H/H/Me	25±6	0.84±0.03	58±1	0.000	490
2b	H/H/F	91±7	0.85±0.05	330±20	—	—
2c[12]	Cl/Cl/Me	149±2	40±2	110±4	+1.290[13]	680
2d[12]	CN/H/Me	185±9	260±10	200±10	+3.356[13]	740
2e[8]	NO_2/H/Me	190±10	520±70	850±60	+3.960[13]	810
3a[11]	H/H/Ph	8.5±0.3	1.9±0.1	2.3±0.5	—	—
3b[11]	H/H/Me	14±2	23±2	30±4	—	—
3c[11]	NO_2/H/Me	150±3	68±7	22±3	—	—
4[12]	-/-/Me	0.063±0.002	(1.19±0.03) $\times 10^{-3}$	(4.1±0.1)× 10^{-3}	—	—

Several observations can be made based on the data from Table 2. First, k_I is very sensitive to substitutions of the methyl groups of the malonamide while k_{II} is not. Steric bulk at the malonamide residue hinders catalyst activation. Replacement of the ethyl groups of **1a** with methyl groups to give **1d** results in a significant factor of 20 increase in k_I from 1.8 to 31.4 $M^{-1}s^{-1}$, respectively, while the k_{II} values of 2800 and 4950 $M^{-1}s^{-1}$, respectively, remain similar. Substitution of the geminal methyl groups of the malonamide residue of **1f** with fluorine gives **1g** and results in a twofold k_I increase from 152 to 350 $M^{-1}s^{-1}$, respectively, while the k_{II} values of 27,000 and 41,000 $M^{-1}s^{-1}$, respectively, remain similar. Replacement of the same methyl groups of **2a** with fluorine

gives **2b** and results in an approximately four-fold k_I increase from 250 to 910 $M^{-1}s^{-1}$, respectively, while the k_{II} values of 840 and 850 $M^{-1}s^{-1}$, respectively, remain within error of each other. The 20-fold difference in k_I between **1a** and **1d** cannot be accounted for by the difference in the electronic effects of ethyl groups and methyl groups. It is more likely that the increase observed on switching to the smaller substituent derives from a decrease in steric hindrance near the iron center. Such a steric effect could derive from a hindering of the approach and/or binding of H_2O_2 to the iron atom of Rc, or disfavoring certain rotamers formed by rotation of axially bound H_2O_2 about the Fe—O bond axis. Decreases in k_I upon hindrance of the peroxide have been observed with the exception of benzoyl peroxide catalyst activation by which likely proceeds via a different mechanism from that of H_2O_2, *t*-BuOOH, and cumyl hydroperoxide.[15] All of these conclusions lend further support to the existence of a preequilibrium H_2O_2 binding for both **1** and **2** as proposed in Chapter 2. While it holds for both **1** and **2**, the origin of the small ~3 fold k_I increase on fluorine substitution for the methyl groups of the malonamide to give **1g** from **1f** and **2b** from **2a** is open to speculation as the effect is small. The k_I increase may derive from a further decrease in steric hindrance beyond that of the methyl groups. Alternatively, the increase could result from the electronegativity of fluorine however the same electronic effects would be expected to perturb k_{II}. Some perturbation is observed for **1** however none is observed for **2**. For **2b** the orbitals of this position may not contribute heavily to the active catalyst LUMO or SOMO into which electrons flow during substrate oxidation.

Second, **1b** is an outlier which may undergo intramolecular oxidation to a more active form. Substitution of **1d** with a methyl ester to give **1e** increases k_I by ~10 $M^{-1}s^{-1}$ to 38 $M^{-1}s^{-1}$ and k_{II} by ~2000 $M^{-1}s^{-1}$ to 7,300 $M^{-1}s^{-1}$. The k_I and k_{II} increases of **1b** over those

1d of ~20 $M^{-1}s^{-1}$ and ~4000 $M^{-1}s^{-1}$, respectively, align well with those expected to result from conversion of both **1b** electron-donating methyl groups to electron-withdrawing carbonyl group bearing functionalities. The oxidation portion of this process is likely intramolecular since the catalyst concentrations employed in these studies are 10^{-8}-10^{-7}, where processes which are bimolecular in TAML are unlikely.[1] The additional oxygen atom may derive from H_2O. Further studies of this behavior should be conducted as it could prove a useful property for synthesizing TAML catalysts in cases where the phenylenediamine must attack a poor electrophile.

Third, while the impacts of phenylenediamine substitution with electron-withdrawing groups on the k_I of **1** and **2** are similar, those on the k_{II} are substantially different. Aromatic substitution of **1** with electron-withdrawing groups raises both k_I and k_{II} proportionally. Substitution of **1d** with a nitro group to give **1f** results in an increase in k_I from 31.4 to 152 $M^{-1}s^{-1}$ and k_{II} from 4,950 to 27,000 $M^{-1}s^{-1}$, approximately fivefold in each. Likewise, substitution of **1d** with a methyl ester to give **1e** results in modest increases in k_I to 38 $M^{-1}s^{-1}$ and k_{II} to 7,300 $M^{-1}s^{-1}$, a very similar 1.2 and 1.5-fold in each. While previous work concluded that altering the substituents of methylene carbon of the **1** malonamide results in greater changes of TAML reactivity with respect to hydrolysis of the resting catalyst than aromatic substitution with electron-withdrawing groups[16], these data show both phenylenediamine and malonamide methylene substitution to have similar effects on k_I and k_{II}. The **2** k_{II} is disproportionately sensitive to phenylenediamine substitution with electron-withdrawing groups. Appendage of two nitro groups to the aromatic rings of **2a** to give **2e** results in an almost tenfold k_I increase from 250 to 1900 $M^{-1}s^{-1}$, about fivefold for each nitro group as for **1d** and **1f**. However, this substitution

increases k_{II} from 840 to 520,000 $M^{-1}s^{-1}$, a 600-fold increase. Substitution with two nitrile groups gives **2d** and increases k_I to 1850 $M^{-1}s^{-1}$ and k_{II} to 260,000 $M^{-1}s^{-1}$, approximately fivefold and 300-fold, respectively. Substitution with four chlorine atoms increases k_I to 1490 $M^{-1}s^{-1}$ and k_{II} to 40,000 $M^{-1}s^{-1}$, approximately twofold and 50-fold, respectively. When coupled with the previously mentioned decrease in k_{II} of **2a** to one sixth of that of **1d**, these dramatic increases in reactivity suggest a formulation of **1d** Ac as a metal centered Fe^{V}-oxo complex, as demonstrated for **1d**, and a contrasting formulation of **2a** Ac as either a less reactive delocalized Fe^{IV} radical cation or as its resonance hybrid with a more reactive metal-centered Fe^{V}-oxo. The surprisingly low k_{II} value of **2a** may be the result of the increased opportunities for delocalization afforded by the additional phenylenediamine residue of the **2** ligand. These analyses suggest that a comprehensive Mössbauer/EPR study of isolated Fe^{V}-oxo complexes for the studied suite of catalysts could be a fruitful avenue for future research. Electron-withdrawing groups may disfavor oxidation of the aromatic rings of **2** shifting the character of Ac towards the less delocalized metal centered Fe^{V}-oxo form, which reasonably would be expected to be more reactive. Notably, substitution of the geminal dimethyl groups of **2a** with fluorine to give **2b** does not increase k_{II}. This is consistent with the above logic as this substitution would not be expected to greatly disfavor the Fe^{IV} radical cation form.

Fourth, neither the phenylenediamine residues nor the geminal position of the malonamide are the sole site at which the observed catalyst inactivation pathway operates. While phenylenediamine-free **4** does display a rate of catalyst inactivation that is about 200-fold less than that of **1c**, the catalyst with the next smallest k_i, this rate is nevertheless nonzero indicating that the phenelyenediamine residue is not required for

inactivation. Importantly, at pH 7, the **1a** k_i is three fold lower that of **1d** indicating that the ethyl groups of the latter do not significantly alter the rate of catalyst inactivation under these conditions. Furthermore, substitution of the six-membered ring methyl groups of **1f** with fluorine atoms to give **1g**, which should block hydantoin formation, *increases* the degradation rate by a factor of 3.2. The analogous **2** substitution of **2a** to give **2b** increases k_i by an even greater factor of 5.7. This trend was also observed in catalysis of the pH 11 oxidation of Safranin O by H_2O_2,[1] suggesting that the pH 11 decay mechanism may be similar to that observed here.

Hammett Plots Analyzing the Technical Performance Parameters and Electrochemistry

With the rate constants k_I, k_{II}, and k_i for large number of closely related powerful oxidation catalysts in hand, Hammett plots and plots of the correlations with electrochemistry were constructed. However, at the outset it is important to point out some facts and observations that limit the number of **1** catalysts that can be included in Hammett plots. First, while phenylenediamine substitutions differentiate many of the catalysts, the rest of each compared catalyst must be identical. Therefore, I have compared only catalysts with geminal methyl groups appended to the methylene carbon of the malonamide. In addition, while it has the appropriate structure, the previously discussed outlier **1b**, must be excluded as it is likely that the oxidatively sensitive aromatic methyl substituents undergo oxidative conversion while the catalyst is functioning. Consequently, only the rate data for **1c**, **1d**, **1e**, and **1f** were considered suitable for constructing Hammett plots. Unfortunately, the relationships between the

redox potentials for **1** catalysts shown in Table 2 obtained by different researchers in the group at different times vs Ag/AgCl reference electrode reveal inconsistencies in the literature electrochemical data which render correlations with redox potentials impossible. The quantities of **1c**, **1e**, and **1f** currently available for a single study were insufficient for preparation of acetonitrile soluble salts to confirm this previously recorded electrochemical data.

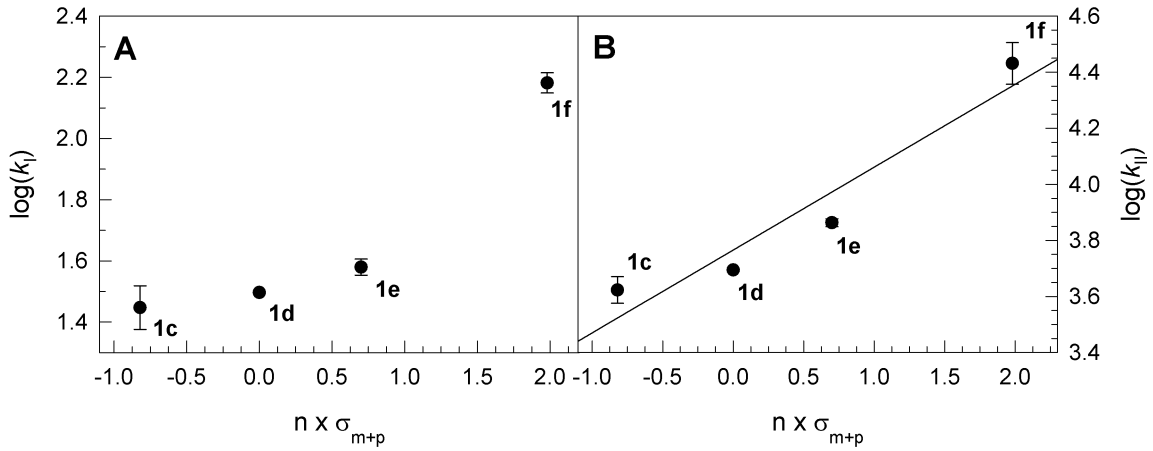

Figure 5. Hammett plots of the dependence of **1** log(k_I) (**A**) and log(k_{II}) (**B**) for data collected at 25 °C and pH 7 in 0.01 M phosphate buffer. Equation 12 is the analytical form of the line of best fit shown in B.

As was shown in Chapter 2, the Hammett plot for the log(k_I) linear dependency on σ_{m+p} for the **2** catalysts exhibits a strong concave downward trend bolstered by the near perfect fit (R^2~1) observed for that of k_{II} with similar correlations found for E^o_1 and E^o_2. However, the **1** catalysts at pH 7 do not show equally consistent trends. The k_I Hammett plot may display a nonlinear concave up trend as shown in Figure 5A, however **1d** and **1e** deviations from linearity are mirrored in the k_{II} Hammett plot of Figure 5B. The k_I data do not fit a linear model very well (R^2 = 0.85). It is likely that there is an

underlying mechanistic reason for the differences between the **1** and **2** k_I Hammett plots. This may derive, for example, from the available diffusion pathways to the much more open Fe centers in the **2** catalysts, in which all three five-membered rings lie in the plane of the amido N atoms as compared with the more sterically encumbered environment in the **1** catalysts where two of the rings have dimethylglycine components.

The **1** k_{II} data shown in Fig. 5B do fit a linear model quite well ($R^2 = 0.92$), though not as well as those of **2**. Equation 12 below gives the analytical form of the line of best fit shown in Figure 5B. The ρ value of (0.30±0.06) matches those found previously for pH 9 catalysis of the oxidation of Ru^{II} dyes and that of the pH 9 oxidation of Orange II by H_2O_2 at 25 °C of 0.3 and 0.4, respectively.[14,15] Unlike in prior studies, **1d** was not found to be an outlier here.

$$\log(k_{II}) = (0.30 \pm 0.06)\mathrm{n}\times\sigma_{m+p} - (3.8 \pm 0.1) \qquad (12)$$

The **1** k_i data shown in the Hammett plot of Figure 3 are ill-suited to linear regression analysis ($R^2 = 0.27$). However, a linear regression analysis of this pH 7 data was performed to see if any correlation could be found since phenylenediamine substitution with electron-withdrawing groups was found to confer resistance to catalyst inactivation in the previous pH 11 study.[1] Equation 13 is the analytical form of the line shown in Figure 6. No correlation between $\log(k_i)$ and σ_{m+p} is observed at pH 7 as indicated by the ρ value of (0.2±0.2). While this data set is limited, it provides no evidence of a correlation between phenylenediamine substitution with electron-withdrawing groups and catalyst inactivation.

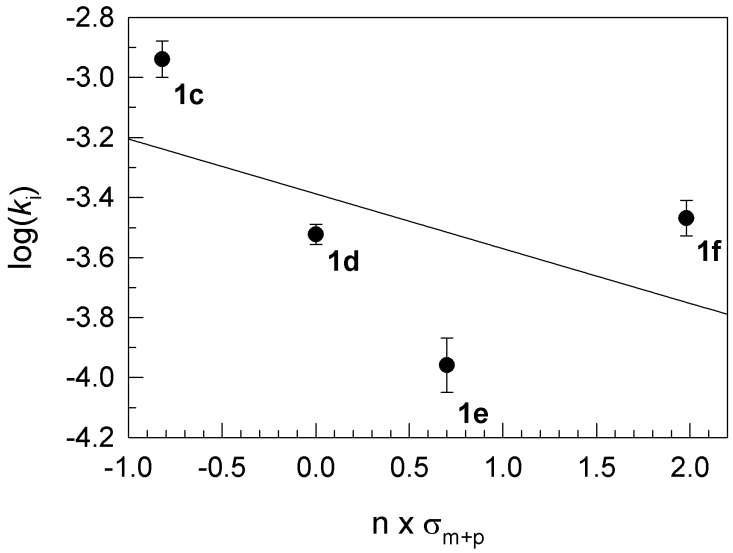

Figure 6. Hammett plot of the dependence of **1** log(k_i) for data collected at 25 °C and pH 7 in 0.01 M phosphate buffer on the composite Hammett parameter n × (σ_{m+p}). Equation 13 is the analytical form of the line of best fit shown.

$$\log(k_i) = -(0.2 \pm 0.2)n \times \sigma_{m+p} - (3.4 \pm 0.2) \quad (13)$$

Since calculations of k_i are dependent on k_{II} as indicated by eq 8, the perfect linear dependencies of the **2** log(k_{II}) vs σ_{m+p} as well as E^o_1 and E^o_2 plots reinforces conclusions based on the limited **2** k_i data set. Concave upward dependencies of log(k_i) on σ_{m+p}, E^o_1, and E^o_2 are observed as shown in Figures 7A and B. Such dependencies may be indicative of a change in mechanism or transition state across a series of compounds and have been observed for nucleophilic attacks of electrophilic alkyl and acyl halides.[17]

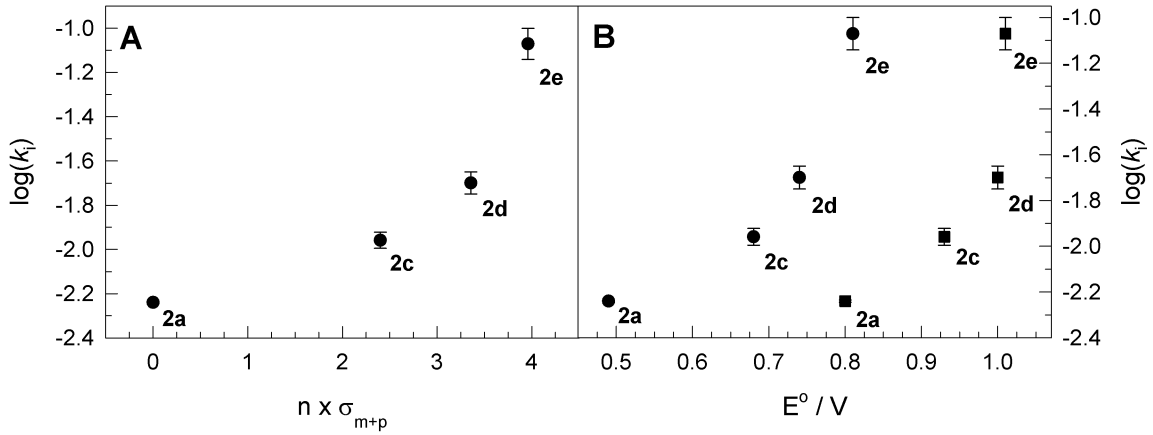

Figure 7. (A) Hammett plot of the dependence of **2** log(k_I) on the composite Hammett parameter n × (σ_{m+p}); data collected at 25 °C and pH 7 in 0.01 M phosphate buffer (**B**) Dependence of **2** log(k_I) on the first redox potential; data collected for 1.00×10^{-3} M CH_3CN solutions of **2** with 0.1 M [^{n}Bu$_4$N][PF_6] at a glassy carbon electrode.

Linear Free Energy Relationships (LFERs) Relating the Technical Performance Parameters

Some of the body of work described in this section was published in February 2016 in the *Journal of the American Chemical Society*—JACS chose the article for a "Spotlight". Different linear free energy relationships (LFERs) are presented here to highlight the properties of a larger **2** data set and permit a deeper analysis than that reported in the publication. Observation of a LFER between the pH 11 k_i and k_{II} values of 8 geminal dimethyl malonamide containing **1** catalysts for catalysis of the oxidation of Safranine O with a line of best fit having a slope of -1 was interpreted as evidence for the protective nature of electron-withdrawing phenylenediamine substituents against catalyst degradation.[1] To determine if the same trend holds for the oxidation of Orange II at pH 7, a similar k_i / k_{II} LFER of the pH 7 data for was constructed and subjected to the same

analysis as shown in Figure 8—**1b-f** are members of the set of 8 activators in the pH 11 LFER

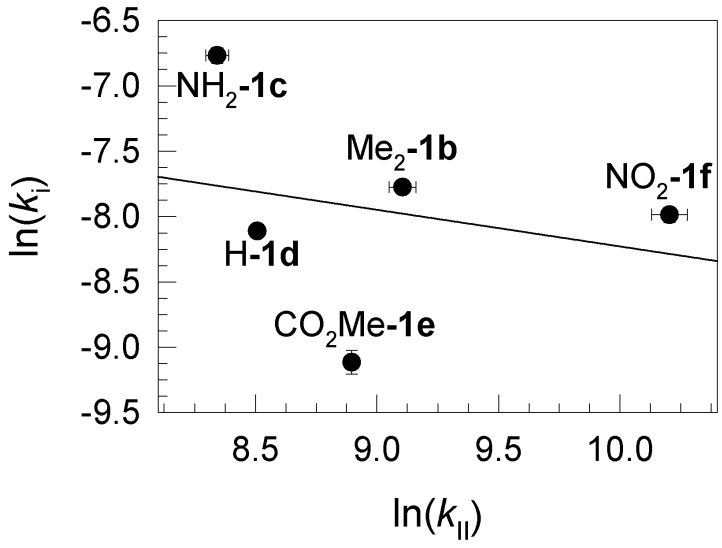

Figure 8. LFER between ln(k_i) and ln(k_{II}); data collected at 25 °C and pH 7 in 0.01 M phosphate buffer. Equation 6 is the analytical form of the line of best fit shown.

$$\ln(k_i) = -(0.3 \pm 0.6)\ln(k_{II}) - (5 \pm 6) \quad (14)$$

As at pH 11, the data are considerably scattered and not well modeled by linear regression ($R^2 = 0.06$). The line of best fit to the data shown in Fig. 8 is eq 14. While the value of the slope, -0.3±0.6, is within error of -0.9, which is close to the previously found value of -1, it is also within error of zero. Like the Hammett plot shown in Fig. 6, this limited data set provides no convincing evidence of a correlation between k_i and k_{II}. However, relationships between TAML catalyst activation, substrate oxidation, and catalyst inactivation processes become apparent over much broader reactivity ranges and

can be visualized by generating k_i/k_I and k_i/k_{II} LFERs containing all of the data in Table 2 as shown in Figs 9 and 10.

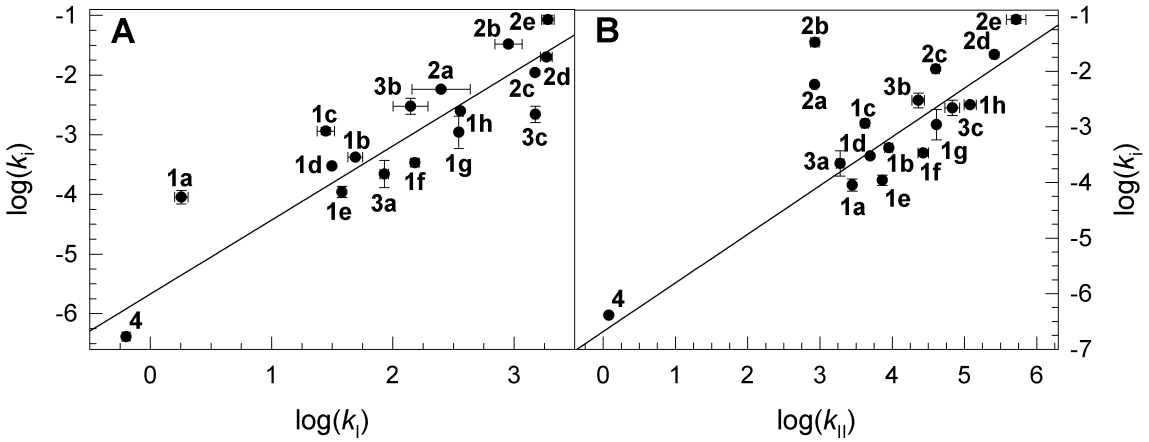

Figure 9. LFERs between (**A**) $\log(k_i)$ and $\log(k_I)$ and (**B**) $\log(k_i)$ and $\log(k_{II})$. Data collected at 25 °C and pH 7 in 0.01 M phosphate buffer. Equations 15 and 16 are the analytical forms of the lines of best fit shown in A and B, respectively.

First, as the most important relationship, k_i and k_I derive from a similar electronic origin. As shown in Fig. 9A, with the exception of the previously noted outlier **1a**, the deviation of which is indicated by its horizontal displacement from **1d**, for all activators k_i and k_I are directly proportional. A linear model was fit to the data excluding that of **1a** to generate the line shown in Fig. 9A having the analytical form of eq 15. No other analytical expression links k_i and k_I indicating that the two processes are not directly connected mechanistically. Consequently, the proportionality must derive from a shared electronic origin.

$$\log(k_i) = (1.2 \pm 0.2)\log(k_I) - (5.7 \pm 0.4) \quad (15)$$

Second, substitution in **1** of the malonamide methylene carbon with alkyl groups larger than CH_3 retards the catalyst activation of Rc. The only outlying data point in Fig. 9A is that of the geminal diethyl substituted malonamide containing **1a** the 50 fold lower k_I value of which has been noted by comparison to electronically similar **1d**. The **1** data set is primarily composed of **1** having geminal methyl groups appended to the methylene unit of the malonamide. The observed disproportional **1a** decrease in k_I may result from interference with H_2O_2 diffusion to the iron atom of **1a**, interference with the binding of H_2O_2 here, or the disfavoring of rotamers formed through rotation about the Fe—O bond of the peroxide bound Rc necessary for catalyst activation. While fluorine bearing **1g** and **1h** possessing less steric bulk at this location do not deviate from the line of best fit, these data alone should not be interpreted as an indication that decreased steric bulk will not enhance k_I as the hydration sphere of the electronegative fluorine atoms may increase their effective size.

Third, increasing steric bulk at the **1** five membered chelate ring on going from the phenylene diamine residue to the 2,3-dimethylbutane-2,3-diamine methyl group does not hinder catalyst activation. The **4** data conform to the Fig. 9A line of best fit indicating that the k_i/k_I proportionality is not significantly disrupted by this substitution.

Fourth, activators **2a** and **2b** display disproportionately low reactivity in catalysis of Orange II oxidation. As shown in Fig. 9A, the **2a** and **2b** data conform to the k_i/k_I proportionality indicating that the k_i values are not disproportionately high in comparison to those of the activator set. However, as shown in Fig 9B, the **2a** and **2b** k_{II} values are approximately 100 times lower than would be expected from the line of best fit shown in

Fig. 9B reflecting disproportionately low rates of Orange II oxidation. This diminished reactivity of **2a** is the source of the massive **2** k_{II} increases observed upon appendage of electron-withdrawing groups. This may reflect the enhanced stability or lower rate of charge transfer to a delocalized $Fe^{IV\bullet+}$ Ac in comparison to those of a localized Fe^{V}-oxo. In concert with the linear dependency of **2** $\log(k_{II})$ on E^o presented in Fig. 6B of Chapter 2, these data suggest that the reactivity of **2** reflects that of a series of activators which span a $Fe^{IV\bullet+}/Fe^{V}$-oxo spectrum with the nature of the electron-withdrawing groups of the phenylenediamine residues dictating their position on it.

Fifth, increases in catalyst reactivity are accompanied by proportional increases in the rate of catalyst inactivation. With the exception of outliers **2a** and **2b**, all of the catalysts studied conform to the same k_i/k_{II} proportionality as shown in Fig. 9B. A linear model was fit to the data excluding that of **2a** and **2b** to generate the line shown in Fig. 9B having analytical form eq 16. The eq. 16 slope of 0.9±0.1 indicates that the rate of Ac inactivation is closely tied to that of Orange II oxidation by Ac. The relative position of the **1a** data in Fig. 9B reinforces the assignment of the deviation shown in Fig. 9A to a low k_I rather than a high k_i as **1a** conforms to the k_i/k_{II} proportionality observed across the set.

$$\log(k_i) = (0.9 \pm 0.1)\log(k_{II}) - (6.7 \pm 0.4) \qquad (16)$$

Sixth, either the amides, the amido N—Fe bond, the iron atom itself or some combination of these are involved in the catalyst inactivation process. The **1a** data do not deviate from the observed k_i/k_{II} proportionality shown in Fig 9B which includes catalysts

with geminal methyl groups and geminal fluorine atoms appended to the methylene of the malonamide. This is a further indication that hydrogen abstraction at the methylene position of the geminal ethyl malonamide substituents is not the primary mechanism of **1a** inactivation in the catalysis of the pH 7 oxidation of Orange II by H_2O_2 at 25 °C. As was observed at pH 11[1] and is further established here by the relative positions of **1g** and **1h** in Fig. 9B, the substitution of methyl groups for fluorine atoms at this position does not alter the observed proportionality. Likewise, appendage of fluorine atoms to this position in **2** does not result in a greatly diminished k_i value as is indicated by the relative positions of **2a** and **2b** in Fig. 9B. It follows that the substituents of the malonamide methylene are not the primary sites of catalyst inactivation under these catalytic conditions as had long been thought. The **4** data do not deviate significantly from the trend observed for the set indicating that the inactivation process is not markedly altered by the absence of the phenylenediamine residue. The only structural components shared by all of the catalysts are the amides, the amido N—Fe bond, and the iron atom itself.

Seventh, while **1** substitution with electron withdrawing groups impacts both k_I and k_{II} equally, **2** substitution has a markedly greater effect on k_{II} than k_I. Consequently, the k_I/k_{II} proportionalities of **1** and **2** are distinct. Since the k_i/k_I and k_i/k_{II} LFERs reveal linear relationships, the k_I/k_{II} LFER also reveals a similar k_I/k_{II} relationship as shown in Fig. 10. However, here the **1** k_I/k_{II} trend differs significantly from that of **2**. Fitting a linear model to the **1** data alone, excluding that of **1a**, gives eq 17, the analytical form of the line of best fit shown in Fig. 10. Fitting the **2** data similarly gives eq 18. Since increasing the **2a** and **2b** k_{II} values to that of **2c** would not be likely to radically increase the 0.2 ± 0.1 slope of this line to the 0.9 ± 0.1 observed for **1**, the low value of the former

likely reflects a difference in the rate determining step of the k_I mechanisms with that of **2** nearly independent of the electronic environment of the iron atom rather than deriving from the proposed radical cation nature of **2a** and **2b**. It is hoped that the further exploration of k_I discussed in Chapter 2 will allow us to determine the exact natures of the **1** and **2** k_I process from the difference between the two. Since catalyst activation is often rate determining, this information could be very useful for the design of more rapidly activating TAML catalysts beyond that attainable by the aforementioned minimization of malonamide methylene carbon substituents. A detailed discussion of the merits of and motivations for this pursuit of higher k_I values can be found in the JACS communication.[18]

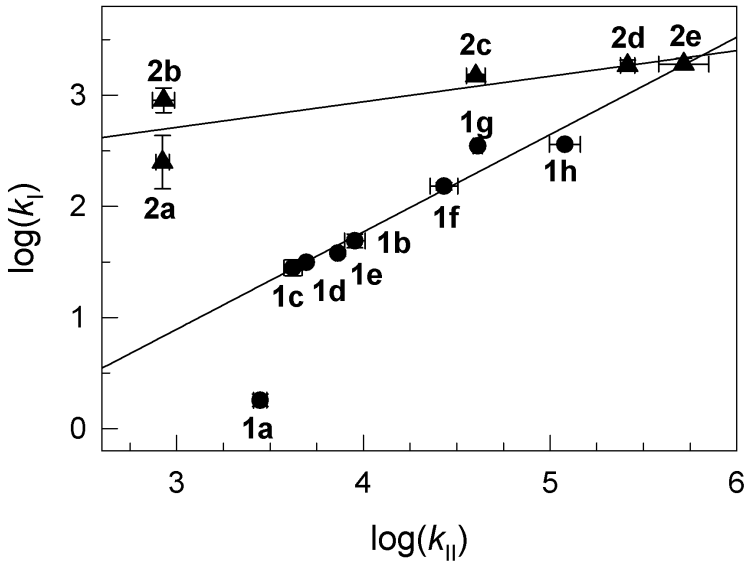

Figure 10. 1 and **2** LFERs between log(k_I) and log(k_{II}). Equations 17 and 18 are the analytical forms of the lines of best fit to the **1** and **2** data, respectively.

$$\log(k_{\mathrm{I}}) = (0.9 \pm 0.1)\log(k_{\mathrm{II}}) - (1.7 \pm 0.4) \quad (17)$$

$$\log(k_{\mathrm{I}}) = (0.2 \pm 0.1)\log(k_{\mathrm{II}}) + (2.0 \pm 0.4) \quad (18)$$

Molecularity of k_{i}

The dependence of k_{i} on [**1d**] was determined as shown in Fig. 8 below. The value of k_{II} in Table 2 and eq 8 were used to calculate k_{i} from incomplete bleaching curves collected at each [**1d**]. The dependence is best described as having a slope of zero indicating that the observed inactivation pathways are unimolecular in catalyst.

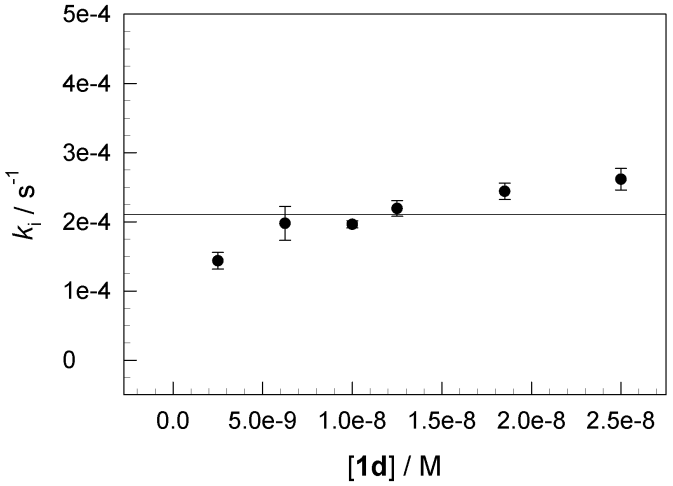

Figure 11. Dependence of the **1d** k_{i} on [**1d**] in catalysis of the pH 7 oxidation of 2.5×10^{-5} M Orange II by 2.5×10^{-3} M H_2O_2 in 0.01 M Phosphate buffer at 25 °C.

A Critical Examination of the Available k_{i} Data

Due to the considerable disagreement between this and the previous k_{i} studies, a thorough examination of the previously published was undertaken. Four conclusions can be drawn from the analysis. First, there is no evidence supporting an assignment of the major **1-4** inactivation process as oxidative decomposition with $[Fe^{III}] < 1\times10^{-6}$ M in 25

°C aqueous solutions that contain readily oxidized substrates, the conditions most relevant for the application of water treatment. While this process may underlie that proposed later in this thesis it does not appear to be the major contributor to catalyst inactivation under these conditions. Most observations of such inactivations have occurred in systems where the solvent is not primarily composed of water or at very high catalyst concentrations where inactivation processes that are bimolecular in catalyst cannot be ignored.[1] This statement also holds for the observed inactivation in catalysis of the oxidation of pinacyanol chloride by H_2O_2 at $[Fe^{III}] = 0.43\times10^{-6}$ M.[19] Observation of less effective catalysis of dye oxidation by **1i** than that of **1j** at $[Fe^{III}] = 0.43\times10^{-6}$ M upon addition of additional dye aliquots after the first has been completely oxidized ($[S]_\infty = 0$) is not indicative of catalyst inactivation under turnover conditions. No differences in the first dye aliquot **1i** and **1j** bleaching traces can be discerned. Differences in the kinetic traces are observed upon introduction of additional dye aliquots. Prior to the introduction of these additional aliquots, the catalyst remains in the presence of an excess of oxidant, but absence of a readily oxidized substrate, conditions distinct from those of functioning catalysis. At this time, the only available 'substrates' are Rc, other Ac, and H_2O_2. It is possible that a lower **1i** k_I with respect to **1j** similar to that observed for the **1a**/**1d** pair may lead to intermolecular inactivation of the **1i** Rc by another **1i** Ac as the absence of an excess of readily oxidizable substrate favors these interactions. This absence of substrate could also drive intermolecular activation occurring from the interaction of two **1i** Ac as well as the intramolecular activation of **1i** Ac due to the longer lifetime of Ac in this system as opposed to one in which an excess of readily oxidized substrate is available. In fact the quantitative data provided herein and in the pH 11 Safranine O studies show no

decrease in k_i across a range of catalysts having varied substituents appended to the malonamide methylene unit, direct evidence that such processes do not occur under turnover conditions in 25 °C aqueous solvents.[1] Just as there is no evidence for intramolecular oxidations of the malonamide substituents under these conditions, there is none for oxidation at the aromatic rings. The pH 11 k_i/k_{II} LFER cannot be interpreted as evidence of inactivation via oxidation of the aromatic residue of the **1** phenylene diamine unit. Visual inspection reveals sufficient scatter and error in data, the latter of which was acknowledged by the authors of the work, for a line with a slope of zero to reasonably fit all of the data shown as is observed for the subset of activators shown in Figs. 6 and 8 in this pH 7 work.[1]

Some evidence of such processes in the case of extremely difficult to oxidize substrates, like metaldehyde, does exist.[20] This is likely due to a shift in the system on going from readily oxidized substrates to very difficult to oxidize substrates which renders the latter much like systems which contain no substrate at all. Careful examination of the initial rate trends reveals that the mechanism of operation in these systems is either different altogether or a different step is rate determining. It is possible that in other systems the catalyst cycle will halt at Fe^{IV} intermediates incapable of substrate oxidation. It is also possible that an underlying catalase mechanism may be come more relevant as the substrate becomes more difficult to oxidize. The relationship between k_i and k_{II} across different substrates remains to be examined. Such a project would be a massive undertaking however the merits of it are equally matched.

Second, the existing quantitative data indicate that for readily oxidized substrates the catalyst inactivation process does not depend on the identity of the substrate.

Matching values of the k_i have been found in both **1d** and **1h** catalysis of Orange II and Safranine O oxidation by H_2O_2 at pH 10.6 and 10.5, respectively, in 0.01 M Phosphate buffer at 25 °C.[1] In addition, inhibition of catalysis by binding of substrate or the products of its oxidation to the metal center is unlikely as the axial ligands of TAML Fe centers have been observed to undergo rapid hydrolysis in water. [15,21]

Third, at pH 11 the **1** k_i dependence on H_2O_2 in catalysis of the oxidation of Safranine O by H_2O_2 may not be linear. The trend shown appears to be hyperbolic. However, this is difficult to determine since k_i varies with k_{II} and a hyperbolic trend is also observed in the k_{II} dependence on $[H_2O_2]$ which should not be the case as the mechanism commonly applied for TAML oxidations shown in Fig. 2 does not provide for this. While such a dependence of k_{II} on $[H_2O_2]$ could arise from contributions from a catalase pathway, my experience in applying the pH 11 model leads me to believe that the hyperbolic k_{II} trend observed is more likely to be a consequence of obtaining the k_{II} values from the intercept of eq 7 rather than the step-wise initial rates method outlined in Chapter 2 of this work. Since a linear fit was employed to determine $k_{i\alpha}$ and $k_{i\beta}$ rather than a hyperbolic form, neither the values so obtained nor their relative magnitudes can be interpreted with complete confidence.

Fourth, the rate-determining step of at least one of the catalyst inactivation processes is likely to be second order and proceeds through a highly ordered transition state as indicated by the large negative values of $\Delta S_i^{\ddagger}$ observed.[1] This value was arrived at from observations of the temperature dependence of k_i itself rather than $k_{i\alpha}$ and $k_{i\beta}$.

Dependences of the Rates of 1 and 2 Inactivation on [OH^-] and [H_2O_2]

Since a linear dependence of k_i on [H_2O_2] was observed in the **1d** and **1f** catalyzed oxidation of Safranine O at pH 11, the dependence k_i on [H_2O_2] was examined for five **1** and three **2** catalysts. This work is currently being refined for publication. A representative sample of the results is shown in Fig. 12 below. In catalysis of the pH 7 oxidation of Orange II by H_2O_2 at 25 °C, k_i exhibits a hyperbolic dependence on [H_2O_2] for these five **1** while all of the tested **2** k_i exhibit a linear dependence. Nonzero y-intercepts are observed in all cases indicating that peroxide independent processes also contribute to inactivation of both **1** and **2**.

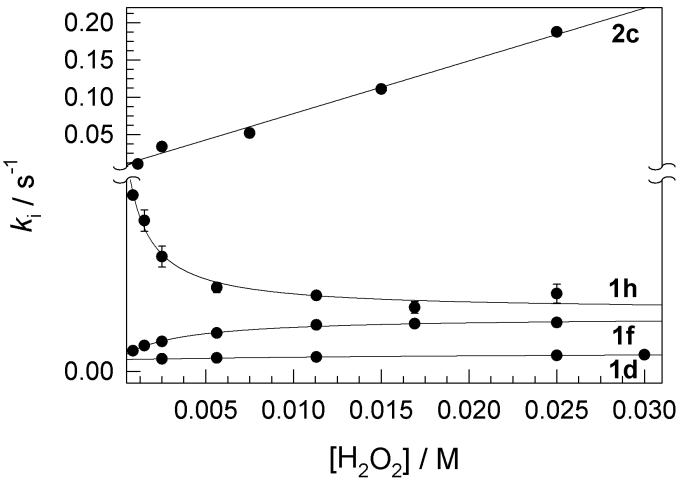

Figure 12. Plot of the [H_2O_2] dependence of k_i in catalysis of the oxidation of 2.5×10^{-5} M Orange II at 25 °C in 0.01 M phosphate buffer, [**1**] = 2×10^{-8} M, [**2**] = 1×10^{-7} M. The numbers indicate the identity of the activator. The value of k_i for each data point is the mean of at least three measurements. The curves fit to **1** were generated using the values in Table 3 and eq 19. The solid line fit to **2c** was obtained by fitting of a linear model to the data shown.

To gain further insight into the **1** inactivation processes, the dependences of **1f** inactivation on [OH^-] over the pH range 6.5–7.5 at [H_2O_2] = 2.5 x 10^{-3} M was determined. The [H_2O_2] was calibrated for a buffered, pH 7 solution. This calibration was assumed to hold over the narrow pH range of 6.5–7.5. Since the determination of k_i is dependent on k_{II}, the **1f** k_I and k_{II} values in the oxidation of Orange II were also determined at every 0.25 pH units over this range as shown in Figs 13A and B. The k_I pH trend in Fig. 13A is consistent with that expected to result from the known TAML bell shaped k_I pH profile. The k_{II} data in Fig. 13B also show a smooth trend consistent with that observed previously.[2] The k_{II} values shown in Fig 13B and eq 8 were used to calculate the k_i values shown in Fig 14.

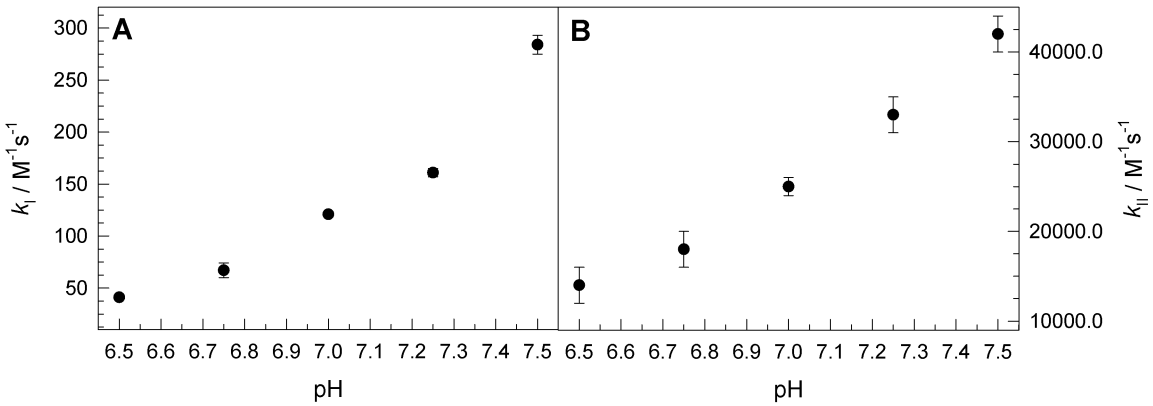

Figure 13. Plot of the dependence of **1f** k_I (**A**) and k_{II} (**B**) on pH in catalysis of the oxidation of 5×10^{-4} M Orange II in 0.01 M Phosphate buffer at 25 °C.

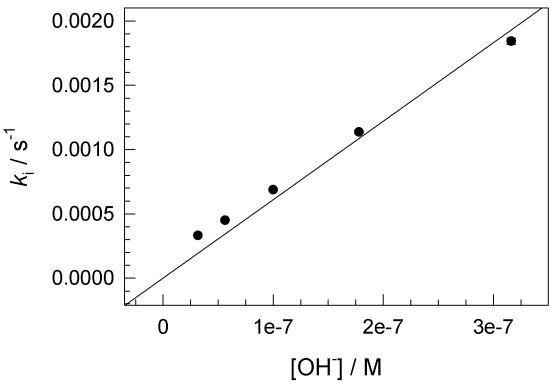

Figure 14. Plot of the linear dependence of **1f** k_i on [OH^-] in 2×10^{-8} M **1f** catalysis of the oxidation of 5×10^{-4} M Orange II by 2.5×10^{-3} M H_2O_2 in 0.01 M Phosphate buffer at 25 °C.

Under these conditions the rate constant of Ac inactivation of **1f** varies linearly with [OH^-]. A linear model with a y-intercept of zero can be fit to the data indicating that under these conditions all of the observed inactivation processes can be considered to be dependent on [OH^-] and k_i can be considered to be a the simple linear function of OH^-, $k_{i,OH}$-[OH^-]. Consequently, the peroxide independent pathway of **1** inactivation evidenced by the nonzero intercepts of the hyperbolic **1** k_i trends observed in Fig. 12 were considered to be hydroxide dependent. The hyperbolic dependence of **1** k_i on [H_2O_2] indicates that in addition to being hydroxide dependent, the binding of peroxide to **1** Ac is reversible. The sum of these pathways gives the scheme shown in Fig. 15 the analytical form of which is eq 19 when the preequilibrium approximation is applied to the concentration of {Ac—H_2O_2}. Fitting of eq 19 to **1** data such as that shown in Fig. 9 with many more data points for most activators gave the values of the rate constants $k_{i\alpha}$ and $k_{i\gamma}$ as well as the equilibrium constant $K_{i\beta}$ shown in Table 3. These and eq 19 were used to generate the curves shown in Fig. 9. In all cases the fits so obtained had R^2 values of

~0.99 indicating that **1** inactivation under these conditions is very well modeled by eq 19. Schemes assigning the identity of the nucleophile to be HOO^- were also considered. However, none of the analytical forms arising from these fit the **1** data. The importance of this observation will be discussed below.

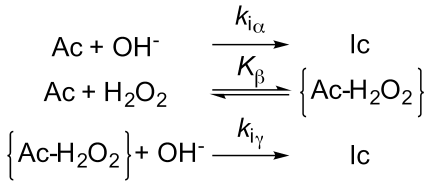

Figure 15. Sequence of events leading to **1** inactivation in catalysis of Orange II oxidation by H_2O_2 at pH 7.

$$k_i = \frac{k_{i\alpha}[OH^-] + k_{i\gamma}K_\beta[OH^-][H_2O_2]}{1 + K_\beta[H_2O_2]} \quad (19)$$

Table 3. Rate constants ($k_{i\alpha}$ units are $M^{-1}s^{-1}$, $k_{i\gamma}$ units are s^{-1}, K_β units are M^{-1}) for the neutral pH Fe^{III}-TAML catalyzed bleaching of Orange II by H_2O_2 at 25 °C in 0.01 M phosphate buffer.

Rc	$X_1/X_2/R$	$10^{-3} \times k_{i\alpha}$	$10^{-1} \times K_\beta$	$10^{-3} \times k_{i\gamma}$
1d	H/H/Me	4.00±0.05	3.5±0.7	7.1±0.2
1e	CO_2Me/H/Me	0.8±0.2	5±2	5±1
1f	NO_2/H/Me	3.9±0.8	31±7	18.5±0.5
1g	NO_2/H/F	36±8	40±30	14±1
1h	Cl/Cl/F	100±10	110±30	18±1

Since **1** inactivation was found to be a function of both $[OH^-]$ and $[H_2O_2]$, the dependence of **2c** inactivation on $[OH^-]$ over the pH range 6.5–7.5 and $[H_2O_2]$ over the concentration range 0.813–8.13 × 10^{-3} M was determined. To do so, the **2c** k_I and k_{II} values in the oxidation of Orange II were also determined at each pH as shown in Figs. 16A and B. The k_I pH trend in Fig. 16A is consistent with that expected to result from the

known TAML bell shaped k_I pH profile. The k_{II} data in Fig. 16B also show a smooth, expected trend typical of such TAML catalysis. The k_{II} values shown in Fig. 16B and eq 8 were used to calculate the k_i values shown in Fig. 17.

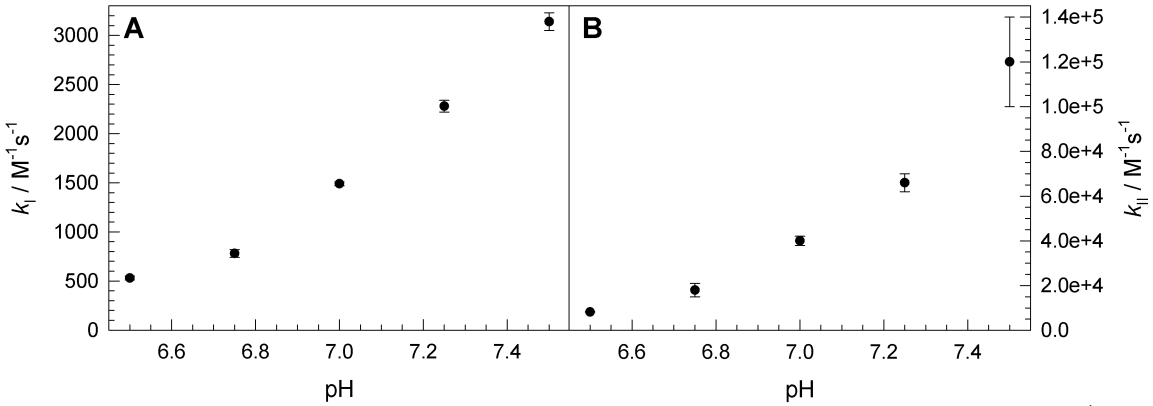

Figure 16. Plot of the dependence of **2c** k_I (**A**) and k_{II} (**B**) on pH in catalysis of the oxidation of 5×10^{-4} M Orange II in 0.01 M Phosphate buffer at 25 °C.

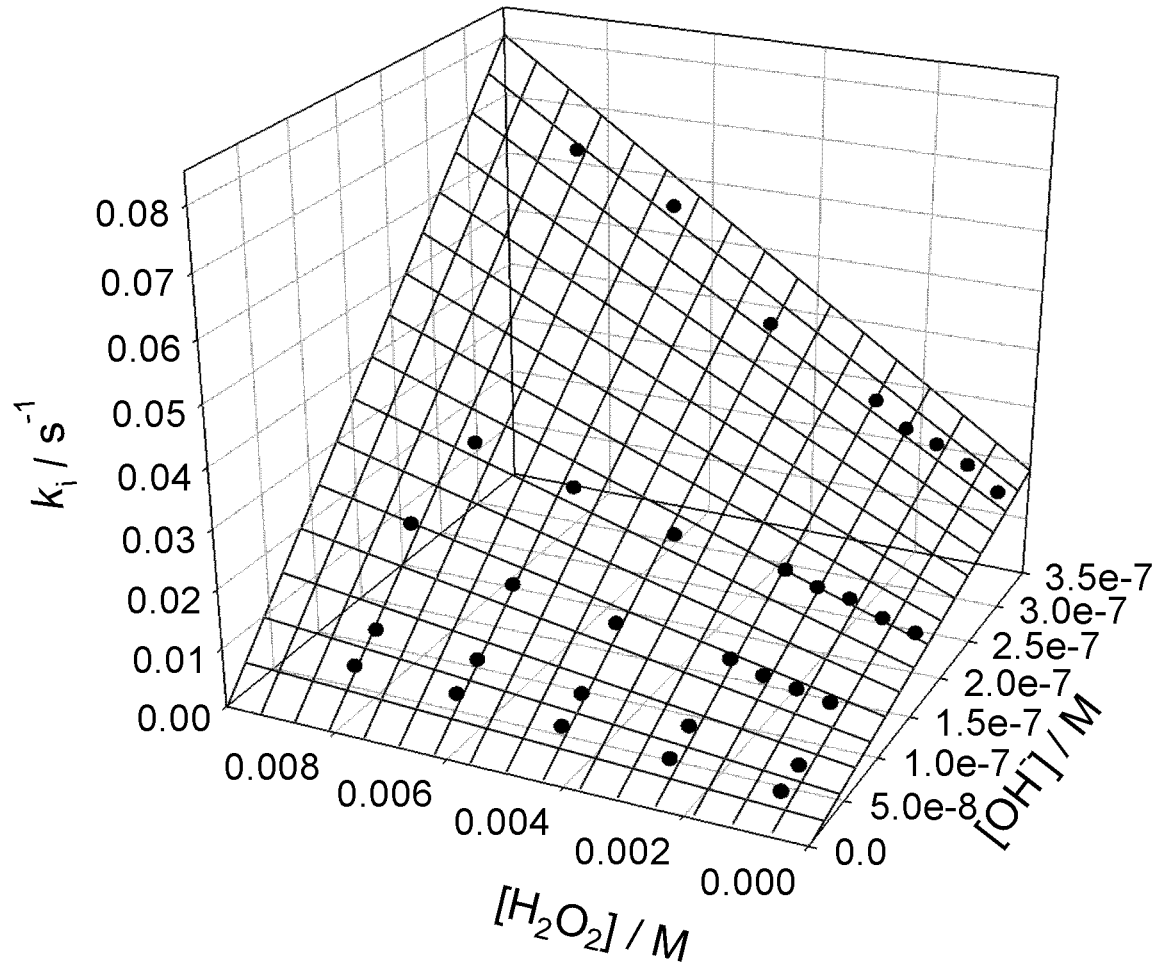

Figure 17. 3D mesh showing dependence of k_i on $[OH^-]$ and $[H_2O_2]$. Equation 20 is the analytical form of the mesh shown with the k_{io}, $k_{i\alpha}$, and $k_{i\beta}$ values listed in the text.

$$k_i = k_{i0} + k_{i\alpha}[OH^-] + k_{i\beta}[OH^-][H_2O_2] \quad (20)$$

Equation 20 gives the analytical form fit to the data in Fig. 14 with the parameters $k_{i0} = (-3\pm8)\times10^{-4}$ s^{-1}, $k_{i\alpha} = (5.5\pm0.5)\times10^{3}$ $M^{-1}s^{-1}$, and $k_{i\beta} = (1.8\pm0.1)\times10^{7}$ $M^{-2}s^{-1}$. Fitting of eq 20 to the k_i data resulted in an R^2 value of 0.97 indicating that under these conditions

2c inactivation is well modeled by eq 20. The k_{i0} value of $(-3\pm8)\times10^{-4}$ s^{-1} is within error of zero indicating that all **2** inactivation pathways are OH^- dependent and two major inactivation steps operate. Equation 20 indicates that one involves OH^- and Ac while the other involves OH^-, H_2O_2, and Ac. These elementary chemical steps are included in the scheme shown in Fig. 18. Equation 21 is the analytical form of the sequence of events shown with the steady state approximation applied to the concentration of {Ac—OOH^-}. Equation 21 takes the form of eq 20 when $k_{-i\beta} \rightarrow 0$, $k_{i\gamma} \gg k_{i\beta}[OH^-][H_2O_2]$, and $k_{i0} = 0$. An analogous scheme assigning the identity of the nucleophile to HOO^- gave an analytical form that also fits the **2** data. However, this assignment is inappropriate as will be discussed below.

$$\begin{aligned} \text{Ac} + \text{OH}^- &\xrightarrow{k_{i\alpha}} \text{Ic} \\ \text{Ac} + \text{H}_2\text{O}_2 + \text{OH}^- &\underset{k_{-i\beta}}{\overset{k_{i\beta}}{\rightleftharpoons}} \{\text{Ac-OOH}^-\} + \text{H}_2\text{O} \\ \{\text{Ac-OOH}^-\} &\xrightarrow{k_{i\gamma}} \text{Ic} \end{aligned}$$

Figure 18. Sequence of events leading to **2** inactivation in catalysis of Orange II oxidation by H_2O_2 over a pH range of 6.5-7.5 and a $[H_2O_2]$ range of 8.13×10^{-4} M to 8.13×10^{-3} M.

$$k_i = \frac{k_{i\alpha}k_{-i\beta}[OH^-]+k_{i\alpha}k_{i\gamma}[OH^-]+k_{i\beta}k_{i\gamma}[OH^-][H_2O_2]}{k_{-i\beta}+k_{i\gamma}+k_{i\beta}[OH^-][H_2O_2]} \quad (21)$$

Fitting of eq 20 to the H_2O_2 dependences of **2a**, **2d,** and **2e** similar to that shown in Fig. 12 with even more data points for most activators gives the $k_{i\alpha}$ and $k_{i\beta}$ values listed in Table 4 below alongside those obtained through fitting of the mesh to the **2c** k_i data shown in Fig. 17. I am in the process of constructing a similar mesh for the **1f**

inactivation process. The lower k_i of **1f** and greater complexity of eq 19 demand significantly longer measurement times, especially at pH 6.5, and a larger data set than required for **2c**.

Table 4. Rate constants ($k_{I\alpha}$ units are M^{-1} s^{-1}, $k_{i\beta}$ units are M^{-2} s^{-1}) for the neutral pH Fe^{III}-TAML catalyzed bleaching of Orange II by H_2O_2 at 25 °C in 0.01 M phosphate buffer.

Rc	$X_1/X_2/R$	$10^{-3} \times k_{i\alpha}$	$10^{-7} \times k_{i\beta}$
2a	H/H/Me	14±7	1.4±0.1
2c	Cl/Cl/Me	5.5±0.05	1.8±0.1
2d	CN/H/Me	120±10	6.4±0.7
2e	NO_2/H/Me	300±80	43±2

Four key observations can be made from the data. First, productive TAML catalysis of Orange II oxidation by H_2O_2 is dependent on maintaining a high [Orange II]/[OH^-] ratio. This is understood through careful examination of eq 16, which gives the line of best fit to the k_i/k_{II} LFER shown in Fig. 9B, eq 19 which models the OH^- and H_2O_2 dependence of **1** inactivation, and eq 20 which models the OH^- and H_2O_2 dependence of **2** inactivation when $k_{i0} = 0$. The relation $k_{iobs} = k_{iOH-}[OH^-]$ holds for both **1** and **2** inactivation as evidenced by the [OH^-] dependence of all inactivation processes modeled by eqs 19 and 20. Equation 16 is within error of $\log(k_{iobs}) = \log(k_{II}) - 7$. Substitution of k_{iOH-} as $k_{iobs}/[OH^-]$ for k_i into $\log(k_i) = \log(k_{II})$, the general form of the line of best fit to the k_i/k_{II} LFER gives $\log(k_{iobs}/[OH^-]) = \log(k_{II})$, which is equivalent to $\log(k_{iobs}) = \log(k_{II}) + \log([OH^-])$. Since all data were collected at pH 7, $\log([OH^-]) = -7$, which gives the form within error of eq 16. This lends further support to the [OH^-] dependence of k_i and importantly indicates that $k_{iOH-} \sim k_{II}$ with both having units of M^{-1} s^{-1}. This tells us that catalyst inactivation and substrate oxidation compete for Ac, with the rate of the former

given by d[Ac]/dt = k_{iOH}[Ac][OH^-] and that of the latter given by d[Orange II]/dt = k_{II}[Ac][S]. This is a strong indication that in applications where the substrate behaves like Orange II with $k_{iOH-} \sim k_{II}$, productive catalysis relies upon maintaining [S] > [OH^-]. The importance of the [S]/[OH^-] ratio can also be shown by substituting $k_{iOH-} = k_{II}$ into the two rate equations and dividing.

Second, nucleophilic attack of H_2O_2 at the **1** dimethyl glycine and **2** oxamide carbonyl carbons compromises functioning catalysis. The location of the attack by H_2O_2 can be inferred from the **1** and **2** k_i H_2O_2 dependences. The mechanistic rationale that follows should be interpreted with caution as it is impossible to definitively prove a mechanism. The reversibility of the **1** K_β step shown in Fig. 15, and accounted for in eq 19 by the preequilibrium approximation, is consistent with the nucleophilic addition of H_2O_2 to the most electrophilic carbonyl carbons of **1**, those of the dimethyl glycine residues as shown in Fig. 19 below. Before the addition, the carbonyl oxygen and adjacent geminal methyl groups of **A** adopt the staggered conformation shown in Newmann projection **A**. Addition of H_2O_2 here would yield a tetrahedral {Ac-H_2O_2} intermediate **B** having the eclipsed conformation shown in Newman projection **B** which is enforced by the constraints of the five membered chelate ring**.** The eclipsing steric interactions forced by the constraints of the five-membered chelate ring of **B** disfavor the formation of {Ac-H_2O_2} and should shift the K_β equilibrium further to the left. Deprotonation of the {Ac-H_2O_2} adduct generates {Ac-OOH^-} **C** which can gain stability by adopting the hydrogen bonded envelope conformation conformation shown in Newmann projection **C**. A similar mechanism has been to operate in formamide and acetamide hydroxylaminolysis[17] and ethyl trifluoroacetate hydrolysis[22].

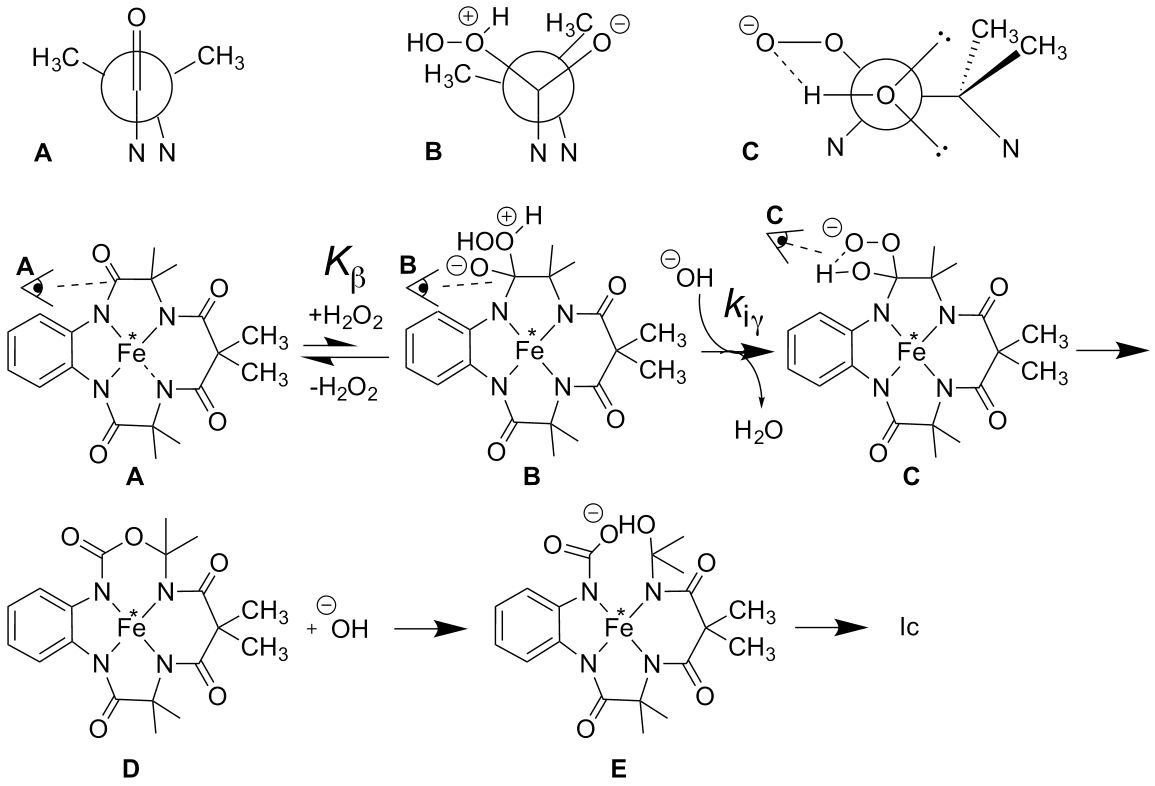

Figure 19. One of the three proposed mechanisms of the H_2O_2 dependent **1** inactivation in catalysis of Orange II oxidation by H_2O_2 at pH 7.

A significant structural difference between the **1** and **2** ligands is substitution of the **1** dimethylglycine residues with the **2** oxamide. This change shifts the identity of the most electrophilic carbonyl carbons from those of dimethyl glycine to those of the oxamide. The eclipsed steric environment of the oxamide carbonyl oxygen atoms shown in Newmann projection **F** of Fig. 20 differs substantially from that of staggered **A** shown in Fig. 19. The strain resulting from the steric clash of the oxamide oxygen atoms is substantial. Calculations performed by Dr. Longzhu Shen have shown that if the synthesis of **2** is attempted by tethering the amines of the phenylenediamines with oxalyl chloride to give the oxalamide first, rather than malonyl dichloride to give the

malonamide first, the anti orientation demanded by the oxamide oxygens produces a significant barrier to rotation which heavily disfavors the cis orientation. Experimental work by Dr. William C. Ellis has found this to preclude macrocycle formation.[23] Here, the strain resulting from the steric clash of the oxamide oxygen atoms is relieved upon addition of H_2O_2 to either oxamide carbonyl carbon of **F** to give the tetrahedral intermediate **G** which is forced to adopt the staggered form shown in Newmann projection $\mathbf{G_1}$ by the geometric requirements of the five membered chelate ring. Like **C**, tetrahedral intermediate **G** can gain stability by adopting a similar envelope conformation shown in Newmann projection $\mathbf{G_2}$. The composition of the **2** addition transition state is consistent with that expected to result from an exothermic process in which the release of strain energy on attack favors an early transition state as predicted by Hammond's postulate.[24] Restoration of the keto form **F** requires that the eclipsing interactions of the oxamide carbonyl oxygens be reestablished. The required simplifications of the **2** kinetic eq 21 provide further evidence of the operation of this mechanism. This steric constraint substantially disfavors the reverse process and may render the addition of H_2O_2 irreversible ($k_{-i\beta} \rightarrow 0$), a requirement for eq 21 to simplify to eq. 20 when $k_{i0} = 0$.

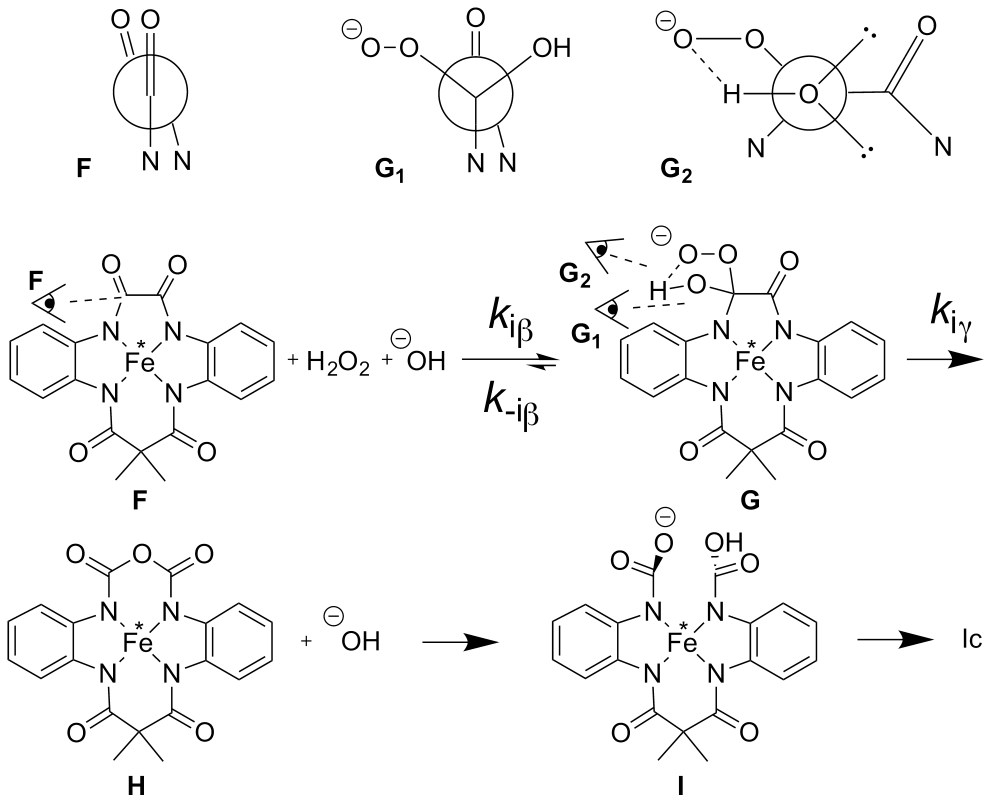

Fig. 20. One of the three proposed mechanisms of the H_2O_2 dependent **2** inactivation in catalysis of Orange II oxidation by H_2O_2 at pH 7.

Third, both **1** and **2** H_2O_2 dependent TAML inactivation mechanisms follow a general base pathway with H_2O_2 as the nucleophile and OH^- serving to accept a proton from an Ac-H_2O_2 complex. The assignment of H_2O_2 as the nucleophile rather than HOO^- is more appropriate as this assignment fits all **1** and **2** k_i data sets, and it is unreasonable to assume that the more electrophilic carbons of **2** would require a better nucleophile than those of **1**. Further evidence of a general base pathway involving H_2O_2 can be found through careful examination of the hydrolysis of activated carboxylic acid derivatives. One such parallel to this H_2O_2 attack of the TAML Ac can be found in the specific acid/general base mechanism of hydrolysis of the protonated form of 2,3,4,5-tetrahydro-

2-oxo-1,5-ethanobenzazepine, which is thought to be N-protonated[25], where H^+ and acetate are analogous to the high-valent Fe of Ac and OH^- in the TAML system, respectively.[26] Under basic conditions, this same substrate is thought to undergo hydrolysis via nucleophilic attack of OH^-.[26] Protonation renders the amido carbonyl carbon electrophilic altering the mechanism of hydrolysis. Similarly, simulations of the hydrolysis of the unactivated amide formamide indicates that nucleophilic attack of OH^- is the dominant mechanism under alkaline conditions,[27,28] however hydrolysis of the more electrophilic carbonyl carbon containing methyl trifluoroacetate, has been calculated to proceed via a general-base mechanism at neutral pH[29] like that proposed for **1** and **2.** A similar mechanistic changeover from nucleophilic attack by OH^- to general base catalysis was reported in a classic paper by Jencks and Carriuolo that reports observations of nucleophilic catalysis of hydrolysis for esters activated in the alcohol portion with the reaction dependent upon the nature of the nucleophile rather than its pK_a and general base catalyzed hydrolysis observed for esters activated in the acyl portion of the molecule with the reaction dependent upon the pK_a of the added base.[30] The former represents the effects of increased stability of the nucleophile while the latter reflects the effects of increased Lewis acidity.

The role of Lewis acidity in **1** and **2** inactivation is clearly visible in the LFERs of Figs. 21 and 22. The **1** K_β/k_{II} proportionality represented by the eq 22 slope of 1.2±0.1 shown in Fig. 21A is evidence that the electrophilicity of the **1** Ac carbonyl carbons is enhanced by the same property that endows the Ac with greater rates of substrate oxidation, increased Lewis acidity at iron. A similar relationship has been found between the equilibrium constant for hydration of esters and increased Lewis acidity of the acyl

substituent.[31] The **1** $k_{i\gamma}/k_{II}$ proportionality shown in Fig. 21B with the line of best fit given as eq 23 may also indicate that Lewis acidity influences this step however the scatter of the data indicate that a fit with no dependence may also be appropriate.

The dependence of the $k_{i\beta}$ pathway on $[H_2O_2]$ and $[OH^-]$ observed for **2** is consistent with that expected to result from H_2O_2 attack with OH^- acting as a general base as in **1**. Similar hydrolysis analogues of this process have also been reported. The hydrolysis of cyclic 1,2-diones, the carbonyls of which are sterically and electronically similar to the oxamide of **2**, has been calculated to proceed via a general base mechanism[32] indicating that the presence of an adjacent carbonyl group alone is sufficient to render the neighboring carbonyl carbon electrophilic enough to undergo hydrolysis via a general-base mechanism. The formulation of the **2** transition state as containing one H_2O_2, one OH^-, and one Ac is precisely as expected based on that calculated[33] for the general base catalyzed[22] hydrolysis of ethyl trifluorothiolacetate.

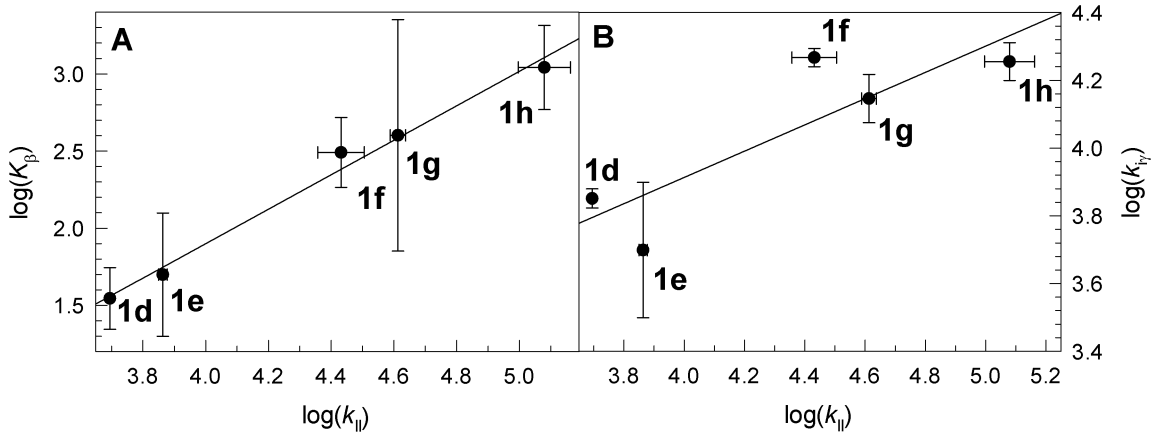

Figure 21. LFERs between (**A**) K_β and k_{II} and (**B**) $k_{i\gamma}$ and k_{II}. Equations 22 and 23 are the analytical forms of the lines shown in (**A**) and (**B**), respectively.

$$\log(K_{\beta}) = (1.2 \pm 0.1)\log(k_{II}) - (2.6 \pm 0.3) \quad (22)$$

$$\log(k_{i\gamma}) = (0.4 \pm 0.1)\log(k_{II}) - (2.4 \pm 0.6) \quad (23)$$

Fourth, the remaining steps of catalyst inactivation may follow a perhydrolysis pathway with rehybridization of the carbonyl carbon and expulsion of either the amido N bearing the high valent iron center, which should render it a decent leaving group, or the electrons of the C—C bond with imine formation and reduction of the metal center, or may proceed via the more elaborate Dakin oxidation pathway shown in Figs. 19 and 20. In the five membered hydrogen bond stabilized cyclopentane envelope-like conformation **C**, the C—C bond between the formerly carbonyl and dimethyl methylene carbons is aligned antiperiplanar to the O—O bond as shown in Newmann projection **C**. A similar relationship exists between the C—C bond between the formerly carbonyl and carbonyl carbons and the **G** O—O bond as shown in Newmann projection $\mathbf{G_2}$. This alignment is ideal for migration of the C—C bond electrons and either the geminal dimethyl carbon of **1** or the acyl unit of **2** into the extra atomic lobe of the O—O σ* orbital with heterolysis of the O—O bond and rehybridization of the formerly carbonyl oxygen and carbon to give the ester **D** and anhydride **H** shown, respectively. Both processes would be intramolecular, in agreement with the **2** assumption $k_{i\gamma} \gg k_{i\beta}[OH^-][H_2O_2]$ since intramolecular processes generally outpace intermolecular ones. In both cases the pendant high valent iron atom would activate the carbonyl carbons of **D** and **H** towards hydrolysis processes similar to the H_2O_2 attack pathway proposed which would yield mono-or dicarbamates. These forms could demetalate due to loss of macrocycle effect imposed stability before or after elimination of CO_2 or oxidation of one substrate

molecule. Discerning between these two possibilities, perhydrolysis and Dakin oxidation, is likely best done through DFT calculations of the energy profiles of each as isolation of the catalyst degradation products is not possible due to the ultra low concentrations of catalyst employed and the significant number of substrate turnovers leading to a much higher concentration of substrate degradation products in solution.

Fifth, the H_2O_2 independent inactivation mechanism data are consistent with general base catalyzed and metal ion promoted amide hydrolysis that would compromise functioning catalysis. The first order dependence of the **1** $k_{i\alpha}$ pathway on [OH^-], identical to those of the **1** $k_{i\gamma}$ pathway, is consistent with that expected to result from a reversible attack of H_2O (like that of the **1** H_2O_2) in which OH^- acts as a general base. The linear dependence of the **2** $k_{i\alpha}$ pathway on [OH^-], like that of the $k_{i\beta}$ pathway, is also consistent with that expected to result from hydrolysis via a general base mechanism. The $k_{i\alpha}/k_{II}$ proportionality represented by the eq 24 slope of 0.7 ± 0.3 obtained by treating **2a** as an outlier shown in Fig. 22 below is evidence of Lewis acid catalysis of the $k_{i\alpha}$ pathway by the Ac high-valent iron atom. I am currently trying to determine the mechanistic origin of the linear relationship which holds for both **1** and **2**. I believe the similarity of the 1 and 2 $k_{i\alpha}$ values and the linear trend to derive from the high concentration of H_2O and the inability of the H_2O-Ac adduct to undergo a migration like that of the Dakin oxidation. The outlying behavior of **2a** may reflect additional peroxide independent inactivation pathways arising from its radical cation nature or contributions from hydrolytic instability of the **2a** Rc.

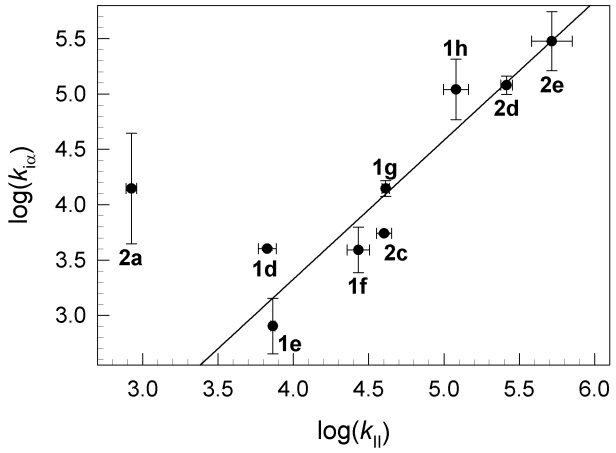

Figure 22. LFER between $k_{i\alpha}$ and log(k_{II}) Equation 24 is the analytical form of the line shown.

$$\log(k_{i\alpha}) = (0.7 \pm 0.3)\log(k_{II}) - (1 \pm 1) \quad (24)$$

Overall, these results agree with the assignment of the $k_{i\alpha}$ pathway as hydrolysis via a general base mechanism, the H_2O analog of that proposed to operate in the H_2O_2 dependent inactivation pathway. Under ambient conditions, amide hydrolysis is commonly regarded as slow with pseudo first order rate constants of 10^{-8}–10^{-12} s^{-1} giving half-lives of hundreds to hundreds of thousands of years.[34-36] Basic hydrolysis at pH 7 and 25 °C proceeds with second order rate constants of 10^{-6}-10^{-1} M^{-1} s^{-1}.[34,35] For these reasons amides are commonly regarded as stable to hydrolysis. Consequently amide hydrolysis and perhydrolysis were not considered to contribute to TAML catalyst inactivation.

The stability of the amide does not derive from resonance of the lone pairs of the amido nitrogen as is commonly taught. Instead it derives from the instability of the resulting amide leaving group as amides are known to undergo ready exchange of the amido oxygen atom.[34] Never the less, the rate of amide hydrolysis has been observed to

be enhanced by lowering the barrier to the substitution through the use of Lewis acidic metal-ion catalysts which form complexes with the amido oxygen and another substrate atom to form a chelate. This metal-ion Lewis acid catalysis of carboxylic acid derivative hydrolysis acting via the direct polarization mechanism has been found to increase hydrolysis rates by $\geq 10^4$ M^{-1} s^{-1} [34] which pales in comparison to that of urease which has been observed to increase urea hydrolysis by a factor of 10^{15}.[36]

Provided the neutral pH hydrolysis rates of the resting **1** TAML catalyst are similar to those of typical amides and the $k_{i\alpha}$ process is base-catalyzed hydrolysis by water, rate constants of ca. 10^{-6} would be expected for the Rc giving a factor of 10^9-10^{11} rate enhancement by Ac, comfortably within the range of Lewis acid catalysis and that of urease. While drastic, this rate enhancement is reasonable given the covalent attachment of a high valent Fe atom to the amide or amides, Since the pendant high valent TAML iron atom is bound to the amido nitrogen atom this same Lewis acidity would also be expected to stabilize the amide leaving group. If this assertion is correct, to my admittedly limited knowledge, the peroxide independent inactivation of Ac would represent the first example of amide hydrolysis catalysis via a Lewis acid bonded to a deprotonated amido nitrogen atom. This effect would have to be very large as esters are observed to undergo base catalyzed hydrolysis at pH 7 and 25 °C with k_b values of ca. 10^{-1}–10^3 M^{-1} s^{-1} [34,35], which approaches the range of observed **1** $k_{i\alpha}$.

Dependence of the k_i of 1d on pH

Since [OH^-] has been shown to greatly influence k_i in the TAML catalyzed oxidation of Orange II by H_2O_2 over the relatively narrow pH range of 6.5–7.5, the

impacts of pH on inactivation of **1d**, the **1** prototype, over the much broader range of 6–13 were investigated. In order to perform these experiments, the extinction coefficients of Orange II and the values of k_I and k_{II} were obtained at each pH and eq 8 and incomplete bleaching traces were used to calculate k_i. The k_I data is shown in Fig. 4 of Chapter 2 and displays the bell shaped pH dependence typical of TAML catalysis. The k_{II} data was expected to mirror the trend shown in Fig. 23 below which gives the pH dependence of the Orange II extinction coefficient. Fitting of these data to eq. 11 from Chapter 2 with $[\text{Orange II}]_{tot}$ substituted for $[Fe^{III}]_{tot}$, $\varepsilon_{HA} = 18{,}870$, $\varepsilon_{A^-} = 9{,}696$ gives $K_a = (1.01 \pm 0.06) \times 10^{-11}$ M and pKa = (11±0.7) indicating that both protonated and deprotonated forms of Orange II exist over this pH range. The k_{II} data were expected to reflect the relative ease with which the more electron-rich deprotonated form is oxidized by Ac.

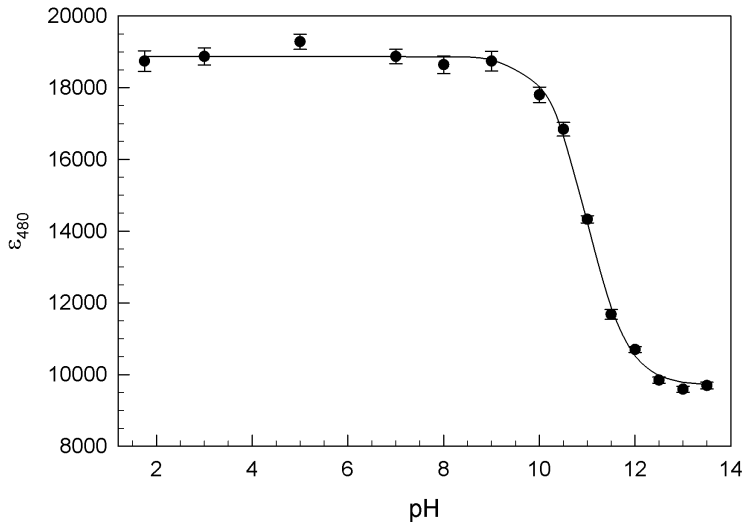

Figure 23. Variations of the Orange II extinction coefficient with pH. The line of best fit was generated using eq 11 from Chapter 2 with the substitution and parameters discussed in the text.

However, the k_{II} data display the more complex trend shown in Fig. 24 below. A similar profile has been observed in **1d** and **1h** catalysis of ferricyanide oxidation by H_2O_2 and attributed to the speciation of four TAML Fe^{IV} complexes formed upon one electron reduction of Ac.[2] The trend was interpreted as an indication that the second reduction of Fe^{IV} is the rate-determining step in the oxidation of ferricyanide. Observation of a similar trend here suggests that the speciation of Ac has a greater effect on k_{II} than does that of Orange II. These data reflect are consistent with the speciation of the one electron reduced Fe^{IV} form though the cause of the increase in the two highest pH data points remains to be rationalized.

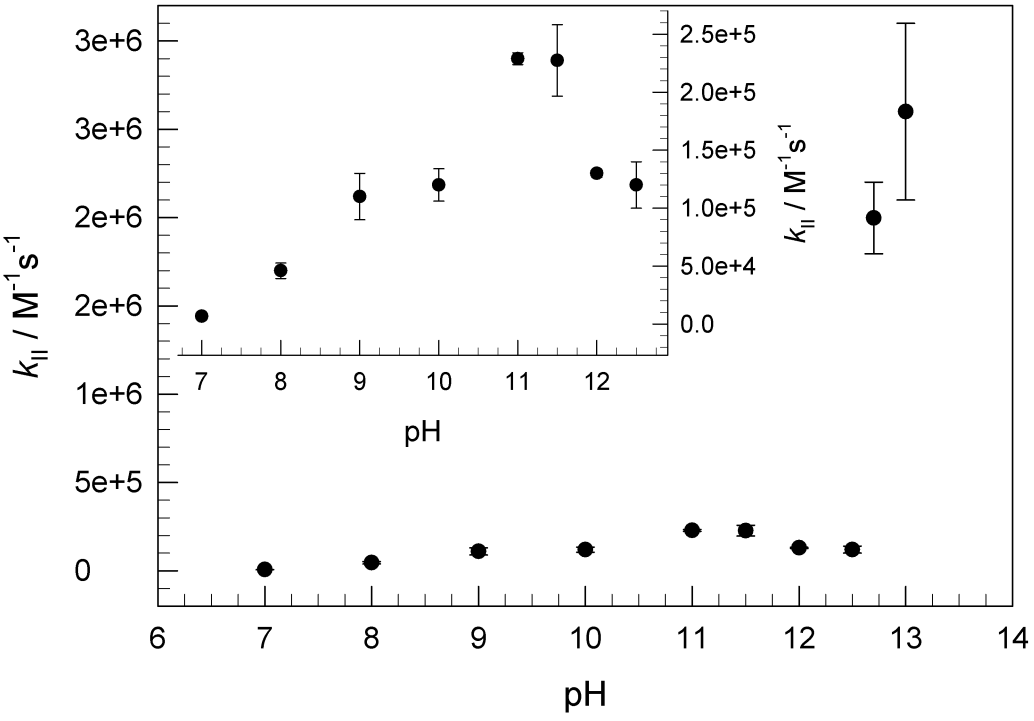

Figure 24. Dependence for **1d** of k_{II} on pH, [**1d**] = 1×10^{-7} M in 0.01 M Phosphate buffer at 25 °C. The inset shows the trends in the data below pH 12.7.

With the dependences of k_I and k_{II} on pH having been determined, and the trends for the former manifesting as expected, the dependence of k_i on pH was investigated and found to be as shown in Fig. 25. There is no sigmoidal trend with an inflection point at ~11.6 signifying the involvement of HOO^-. Another expected but not found result was that k_i would follow the same pattern as k_{II} in the low and high pH regions where the reactivity of H_2O_2 and HOO- would be expected to dominate. However, this was not found either. While the high pH data appear to follow a sigmoidal trend that may have an inflection point at 14 indicating involvement of OH^-, there are subtle trends in the lower pH data visible in the inset. These trends also appear to reflect the Fe^{IV} speciation. However, the k_i trend does not simply parallel that of k_{II}. Instead at pH 11 and 11.5 the k_i values are among the lowest found while maximum k_{II} values below pH 12.5 are found here.

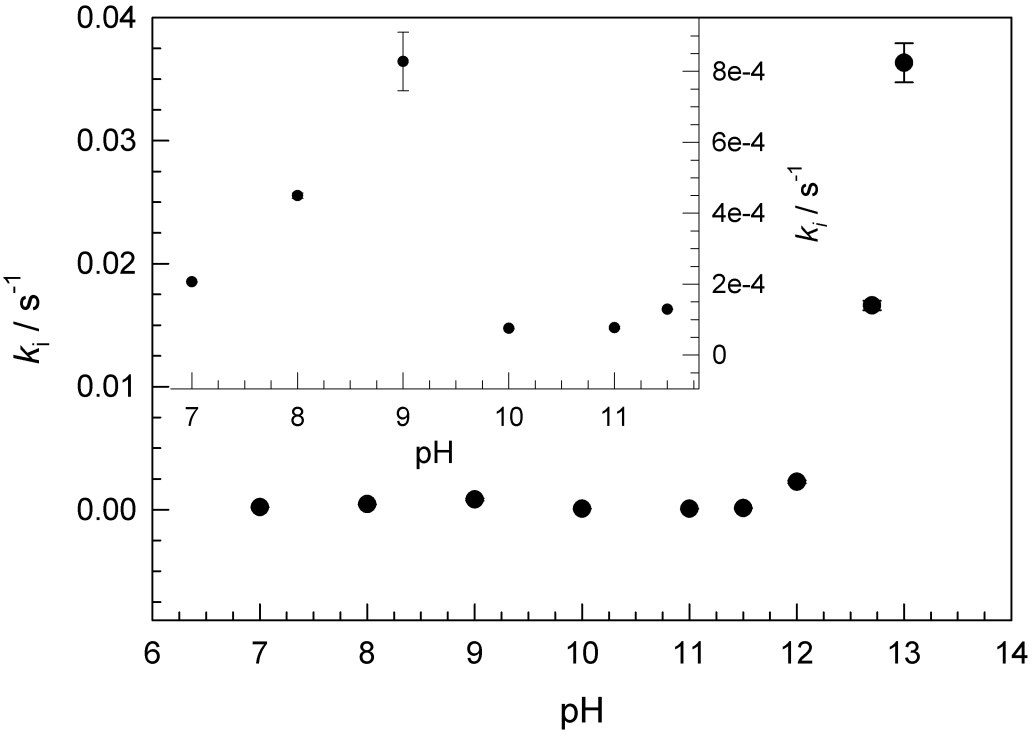

Figure 25. Dependence of the **1d** k_i on pH at $[H_2O_2]+[HOO^-] = 2.5 \times 10^{-2}$ M and [**1d**] = 2×10^{-9} M in 0.01 M Phosphate buffer at 25 °C. The inset shows the trends in the data below pH 12.

Since LFERs were helpful in guiding understanding of the relationships between the rate constants k_I, k_{II}, and k_i for many different catalysts at pH 7, k_I/k_i, k_{II}/k_i and k_I/k_{II} LFERs were constructed for this **1d** data collected at many different pH levels, as shown in Figs 26 and 27. Several observations can be made based on the data in these LFERs.

First, the relationship between the k_I values of **1d** on k_i at the different pH levels is very complex as shown in Fig. 26A. This is expected as the pH distribution of k_I relies upon the speciation of Rc and H_2O_2. That of k_i shown in Fig. 26B is also complex indicating that k_i is dependent upon k_{II}, which in turn depends on the speciation of Ac and the substrate. The result indicates that the correlations observed in Figs. 9 and 10 for data collected at pH 7 represent cases where linear relationships are observable because (*i*) the

speciation of Rc of all of the activators employed is dominated by one Rc species dubbed H_2A in Chapter 2, (*ii*) the speciation of Ac is dominated by one form for all activators at pH 7, and (*iii*) the speciation of Orange II is dominated by the phenol form at pH 7.

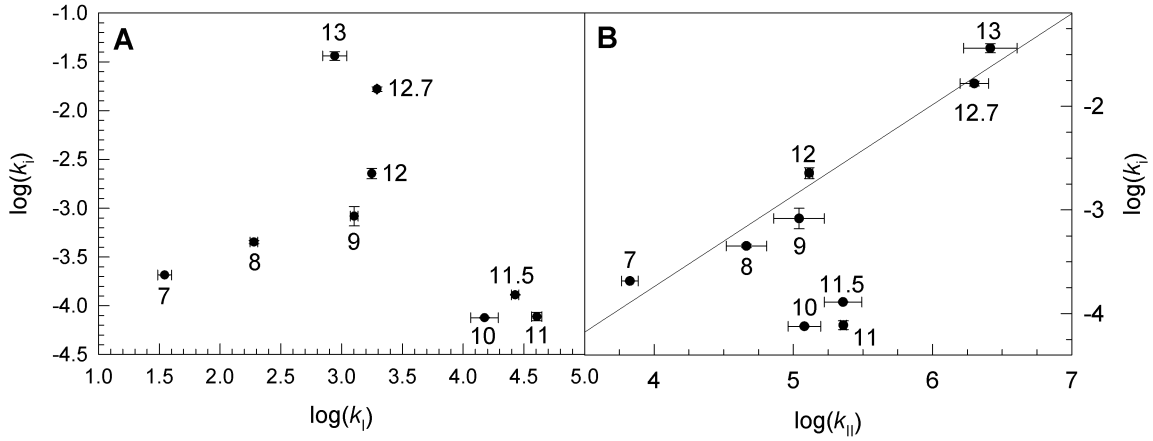

Figure 26. LFERs between (**A**) k_I and k_i, (**B**) k_{II} and k_i. The numbers indicate the pH at which measurements were made. Equation 25 is the analytical form of the line of best fit to the data in (**B**) treating the pH 10, 11, and 11.5 data as outliers.

$$\log(k_i) = (0.9 \pm 0.1)\log(k_{II}) - (7.3 \pm 0.5) \quad (25)$$

Second, under most conditions the k_i values track k_{II} closely as was observed at pH 7. A k_i/k_{II} correlation is observed over most of the tested pH range as is visible in Fig. 26B. Excluding that collected at pH 10–11.5, the slope the line of best fit to the data, eq. 25, of (0.9±0.1) indicates that a similar k_i/k_{II} correlation observed across activators at pH 7 also holds for the behavior of one activator across most of the pH range.

Third, [OH^-] is likely involved in the inactivation mechanism at all of the pH levels on the line in Fig. 26B. The y-intercept of the line of best fit to the data given by

eq. 25 is approximately -7 as was the intercept of the line in eq 16. It follows that the approximation $k_i \sim k_i[OH^-]$ may apply at these pH levels as well. The previous argument about a competition between OH^- and Orange II for Ac may also hold.

Fourth, a k_I/k_{II} correlation holds for most of the pH range observed as shown in Fig. 27 having a line of best fit given by the analytical form eq 26. Deviations observed for pH 12.7 and 13 data may result from the disproportionately low k_I values due to less efficient catalyst activation by HOO^-. The data in Fig. 26B reinforce this by indicating that the observed k_{II} values are not disproportionately high due to an increase in the population of the phenolate form of the Orange II substrate since they conform to the k_i/k_{II} proportionality.

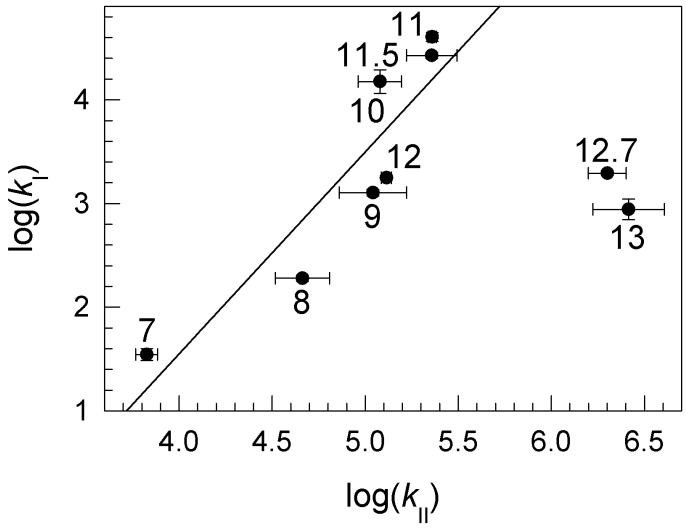

Figure 27. LFER between k_{II} and k_I. The numbers indicate the pH at which measurements were made. Equation 26 is the analytical form of the line of best fit to the data treating the pH 12.7 and 13 data as outliers.

$$\log(k_{\mathrm{I}}) = (1.9 \pm 0.4)\log(k_{\mathrm{II}}) - (6 \pm 2) \quad (26)$$

Fifth, the optimum pH range for **1d** operation is approximately 10-11.5. The pH 10, 11, and 11.5 $k_{\mathrm{I}}/k_{\mathrm{i}}$ data deviate significantly from the rest of the set as shown in Fig. 26A to give the maximum k_{I} values and minimum k_{i} values indicating that when catalyst activation is rate determining, the greatest amount of catalyst turnovers will be achieved here. The $k_{\mathrm{II}}/k_{\mathrm{i}}$ data at these pH levels also deviate significantly from the rest of the set as shown in Fig. 26B to give a $k_{\mathrm{II}}/k_{\mathrm{i}}$ ratio more than one order of magnitude larger than predicted by the line of best fit indicating that when substrate oxidation is rate determining the greatest amount of turnovers will be observed here as well. Thus the pH range encompassing 10–11.5 constitutes a 'sweet spot' in **1d** catalysis at which a region of enhanced stability relative to reactivity is found.

The TAML literature and admittedly limited data allow speculation as to the origin of this region of enhanced stability to guide future experimentation. The [OH^-] dependence of k_{i} in the pH range of 7-13 displays three distinct trends as shown in Figs. 28 and 29.

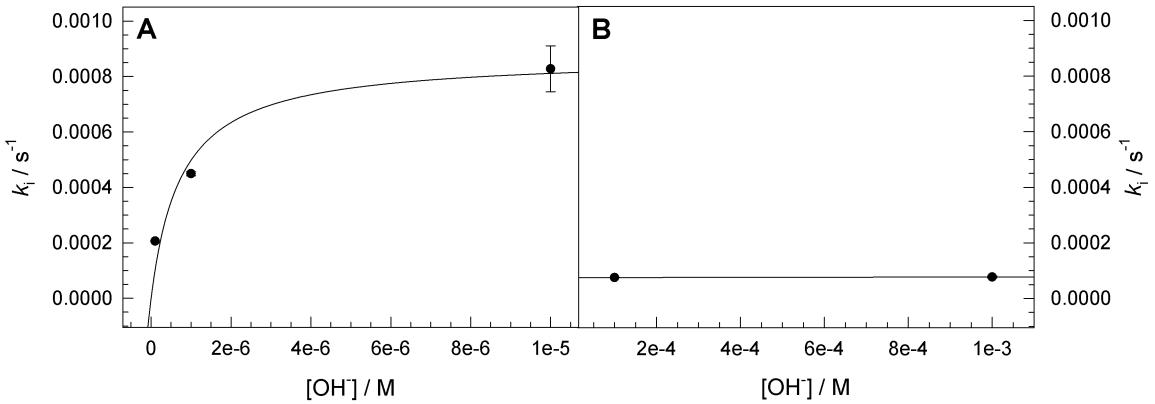

Figure 28. Trends in $[OH]^-$ dependence of k_i at $[OH]^-$ values of (**A**) $(0.01\text{-}1)\times10^{-5}$ M OH^- and (**B**) $(0.1\text{-}1)\times10^{-3}$ M. Equations 27and 28 are the analytical forms of a simple hyperbola fit to the **A** data and the line of best fit to the **B** data, respectively.

Reasonable fits of analytical forms of schemes accounting for the $[OH]^-$ dependence of k_i of a single catalyst species to the data in Fig. 28A could not be obtained. This can be interpreted as evidence that more than one Ac species undergoes inactivation over the pH range 7–9. The form for a simple hyperbola could be fit to the data and is given as Eq. 27. Importantly, in the pH 7 region where $[OH^-] = 1\times10^{-7}$ M, k_i can be considered to be a linear function of $[OH^-]$ in agreement with that found for **1f**.

$$k_{\mathrm{i}} = \frac{(9\pm2)\times10^{-4}[\mathrm{OH}^-]}{(8\pm5)\times10^{-7}+[\mathrm{OH}^-]} \qquad (27)$$

The linear dependence of k_i on $[OH^-]$ shown in Fig. 28B is clear and the line of best fit to the data is given by Eq. 28. This can be interpreted as evidence that the inactivation of the Ac species that predominates over this pH range is only weakly

dependent on [OH^-] and [H_2O_2] / [HOO^-] since this range spans a significant concentration difference in all of these.

$$k_i = 2.2 \times 10^{-3}[OH^-] + 7.5\times10^{-5} \quad (28)$$

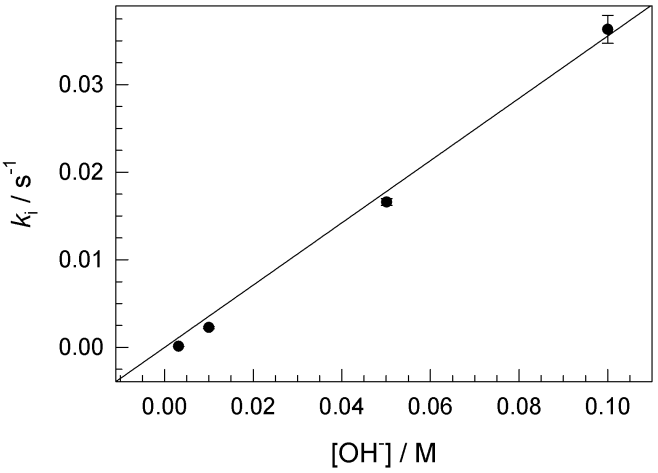

Figure 29. Trend in [$OH]^-$ dependence of k_i over the range (0.032-1)×10^{-1} M OH^-. Equation 20 is the analytical form of the line of best fit shown.

As shown in Table 4, the pH dependence of Ac inactivation is likely linked to the speciation of the formally Fe^V or Fe^{IV} Ac. The pKa_{1Ac}, pKa_{2Ac}, and pKa_{3Ac} values are ~1.5 units lower, ~0.3 units higher, and ~1 unit higher than pKa_{1Rc}, respectively. The 'sweet spot' lies ~0.5 units above pKa_{2Ac} and below pKa_{3Ac} as shown in Table 4. This enhanced stability could be a consequence of dispersion of **C** or its formally Fe^V counterpart's negative charge over the ligand structure including the carbonyl carbons resulting in decreased electrophilicity or a different solvation sphere that interferes with approach of the OH^- critical to both H_2O_2 dependent and independent inactivation pathways. It is also possible that the solvation spheres of **A**, **B**, and **D** (Scheme 2) host an OH^- which

performs the inactivation chemistry on the Ac itself while **C** (Scheme 2) does not. The result suggests the best pH range for maximizing the performance of each individual activator. If the inactivation of **C** is found to obey a k_i/k_{II} proportionality across a set of activators, future work could provide a method for selecting the activator capable of achieving the highest turnover number at the application desired pH. Counterintuitively, it also suggests that neutral pH catalyst inactivation may be slowed if pKa$_{1Rc}$ can be decreased to ~7.5 through increases in the Lewis acidity at iron. Whether this trend holds for **2** remains to be proven. If it does **2e** is the closest to this value of any activator to date.

In this case, the TsAML ligand structures may yield activators capable of attaining this stability region at neutral pH as the amido N—H atoms of sulfonamides are known be significantly easier to deprotonate than those of carbon amides indicating that the sulfonamido N atoms would be expected to be significantly less electron donating than the organic amido N atoms of TAML activators. The TsAML analogue of **2e** having the malonamide organic amides replaced by sulfonamides is of particular interest for studying this behavior as it should possess the requisite qualities for a maximum k_{II} and minimum pK_{a1} as are **1** having all organic amides replaced by sulfonamides.

Table 5. Rate constants ($k_{I\alpha}$ units are $M^{-1}s^{-1}$, $k_{i\beta}$ units are $M^{-2}s^{-1}$) for the neutral pH Fe^{III}-TAML catalyzed bleaching of Orange II by H_2O_2 at 25 °C in 0.01 M phosphate buffer.

Rc	$X_1/X_2/R$	pK_{a1Rc}	pK_{a1Ac}	pK_{a2Ac}	pK_{a3Ac}	Best pH
1d	H/H/Me	10.1[2]	8.3±0.3[2]	10.4±0.7[2]	11.0±0.4[2]	10-11.5
1h	Cl/Cl/F	9.4[2]	7.8±0.3[2]	9.7±0.3[2]	10.4±0.2[2]	9-10.5[a]
2e	NO_2/H/Me	8.43±0.15	7[a]	8.7[a]	9.5[a]	8.5-10.0[a]

[a] estimated using rationale in text.

Experimental

Instrumentation

Spectrophotometric measurements were carried out on a Hewlett Packard Diode Array spectrophotometer (model 8452A) equipped with an automated and thermostatted 8-cell positioner. ^{1}H NMR data were collected at 300 K with a Bruker Avance 300 operating at 300 MHz in the indicated solvent. Chemical shifts were referenced to the previously reported residual proton solvent peak.[37] Solution pH was determined using a Corning 220 pH meter.

Materials

Iron TAML complexes were synthesized at Carnegie Mellon University by published methods.[8-10,18,38]

Kinetic Measurements of TAML-Catalyzed Oxidation of Orange II by H_2O_2

Stock solutions of catalysts **1, 2,** and **4** of ca. $(0.5–5)\times10^{-5}$ M were prepared in HPLC grade methanol. Stock solutions of Orange II were prepared in HPLC grade water. Solutions of H_2O_2 (0.01–0.001 M) were made in pH 7 0.01 M phosphate buffer (using a Corning 220 pH meter) and standardized daily by measuring the absorbance in water at 230 nm (ε = 72.8 M^{-1} cm^{-1}).[39] In a polymethylmethacrylate UV-vis cuvette, the stock solution of Orange II was added to an appropriate amount of 0.01 M, pH 7 phosphate buffer at 25 °C to give a $(5–50)\times10^{-6}$ M solution followed by the addition of 20 μL of a catalyst stock solution of appropriate concentration to achieve the desired catalyst concentration in the range of $(0.1–1)\times10^{-6}$ M. For experiments in which catalyst

concentration was varied the appropriate amount of catalyst stock solution was added followed by an appropriate amount of methanol to bring the total volume of methanol added to 20 μL. The appropriate volume of the stock solution of H_2O_2 was added to initiate the reaction. Initial rates of Orange II oxidation were calculated as the average of at least three measurements using an extinction coefficient of 18,100 M^{-1} cm^{-1} at 485 nm. All calculations were made using the Sigma Plot package (versions 12.0 and 12.5).

Kinetic Evaluation of 1 and 2

The catalytic activity of **1d** and **2c** evaluated using H_2O_2 as an oxidant and Orange II as a substrate. At pH 7 the catalysis was probed in the oxidant concentration range of $(0.05–2.0)\times10^{-3}$ M due to noticeably lower activity of **4** compared to TAMLs **1** and **2**.

Determination of k_i. The effective values of k_i for activators **1**, **2**, and **4** were calculated using eq 8 which, as it has been recently demonstrated[7], holds under all conditions provided H_2O_2 is present in a large excess relative to substrate. To ensure incomplete bleaching, minimal catalyst concentrations of ca. 10^{-9}–10^{-7} M for were employed. Measurements for **4** were made at higher concentrations of ca. 10^{-5} M. It was previously proven for **1** under basic conditions (pH 11) that effective values of k_i are essentially independent of TAML concentration.[1] The same was confirmed in this work. Effective values of k_i were observed to be weakly dependent on catalyst concentration in a 10-fold range around the concentrations identified above.

Summary

In total these results suggest that nucleophilic attack of TAML amido carbonyl carbons by H_2O and H_2O_2 are best modeled as general base catalyzed processes. Although the observed H_2O_2 dependent inactivation process adds oxygen to Ac, the initiating step is nucleophilic rather than oxidative. This is a testament to the oxidative robustness that has been iteratively designed into TAML systems. It also requires that future TAML activators be made free of functionalities susceptible to deleterious nucleophilic substitution in order to obviate this inactivation pathway. This leads one to the conclusion that ligands of catalysts intended to operate in the presence of nucleophiles, especially those which support very electrophilic catalytic intermediates, must incorporate functionalities known to be extremely resistant to deleterious nucleophilic substitution, even more so than that of amides, and perhaps to the extent of being inert to it as a design rule. This is not explicitly stated in the design rules advanced by Dr. Collins likely because most of the cited experiments were not performed in water. To this end Dr. Collins and I have designed next-generation sulfonamide containing catalysts known as TsAMLs in which any or all of the amides are replaced by nucleophile resistant sulfonamides the synthesis and evaluation of which will be covered in Genoa Warner's thesis. Of particular interest for advancing catalysis and studying this behavior are **1** TsAML analogs having all or just the most electrophilic carbon amides replaced by sulfonamides.

References

(1) Chanda, A.; Ryabov, A. D.; Mondal, S.; Alexandrova, L.; Ghosh, A.; Hangun-Balkir, Y.; Horwitz, C. P.; Collins, T. J. *Chemistry – A European Journal* **2006**, *12*, 9336.

(2) Kundu, S.; Annavajhala, M.; Kurnikov, I. V.; Ryabov, A. D.; Collins, T. J. *Chemistry – A European Journal* **2012**, *18*, 10244.

(3) Crabtree, R. H. *Chemical Reviews* **2015**, *115*, 127.

(4) Mills, M. R.; Arias-Salazar, K.; Baynes, A.; Shen, L. Q.; Churchley, J.; Beresford, N.; Gayathri, C.; Gil, R. R.; Kanda, R.; Jobling, S.; Collins, T. J. *Scientific Reports* **2015**, *5*, 10511.

(5) Collins, T. J. *Accounts of Chemical Research* **1994**, *27*, 279.

(6) Collins, T. J. *Accounts of Chemical Research* **2002**, *35*, 782.

(7) Emelianenko, M.; Torrejon, D.; DeNardo, M.; Socolofsky, A.; Ryabov, A.; Collins, T. *J Math Chem* **2014**, *52*, 1460.

(8) Ellis, W. C.; Tran, C. T.; Denardo, M. A.; Fischer, A.; Ryabov, A. D.; Collins, T. J. *Journal of the American Chemical Society* **2009**, *131*, 18052.

(9) Ellis, W. C.; Tran, C. T.; Roy, R.; Rusten, M.; Fischer, A.; Ryabov, A. D.; Blumberg, B.; Collins, T. J. *Journal of the American Chemical Society* **2010**, *132*, 9774.

(10) Sullivan, S. Z.; Ghosh, A.; Biris, A. S.; Pulla, S.; Brezden, A. M.; Collom, S. L.; Woods, R. M.; Munshi, P.; Schnackenberg, L.; Pierce, B. S.; Kannarpady, G. K. *Chemical Physics Letters* **2010**, *498*, 359.

(11) Warner, G. R.; Mills, M. R.; Enslin, C.; Pattanayak, S.; Panda, C.; Panda, T. K.; Gupta, S. S.; Ryabov, A. D.; Collins, T. J. *Chemistry – A European Journal* **2015**, *21*, 6226.

(12) Denardo, M. A.; Mills, M. R.; Ryabov, A. D.; Collins, T. J. *Journal of the American Chemical Society* **2016**, Accepted.

(13) Hammett, L. P. *Journal of the American Chemical Society* **1937**, *59*, 96.

(14) Ghosh, A.; Mitchell, D. A.; Chanda, A.; Ryabov, A. D.; Popescu, D. L.; Upham, E. C.; Collins, G. J.; Collins, T. J. *Journal of the American Chemical Society* **2008**, *130*, 15116.

(15) Chahbane, N.; Popescu, D.-L.; Mitchell, D. A.; Chanda, A.; Lenoir, D.; Ryabov, A. D.; Schramm, K.-W.; Collins, T. J. *Green Chemistry* **2007**, *9*, 49.

(16) Polshin, V.; Popescu, D.-L.; Fischer, A.; Chanda, A.; Horner, D. C.; Beach, E. S.; Henry, J.; Qian, Y.-L.; Horwitz, C. P.; Lente, G.; Fabian, I.; Münck, E.; Bominaar, E. L.; Ryabov, A. D.; Collins, T. J. *Journal of the American Chemical Society* **2008**, *130*, 4497.

(17) Schreck, J. O. *Journal of Chemical Education* **1971**, *48*, 103.

(18) DeNardo, M. A.; Mills, M. R.; Ryabov, A. D.; Collins, T. J. *Journal of the American Chemical Society* **2016**.

(19) Horwitz, C. P.; Fooksman, D. R.; Vuocolo, L. D.; Gordon-Wylie, S. W.; Cox, N. J.; Collins, T. J. *Journal of the American Chemical Society* **1998**, *120*, 4867.

(20) Tang, L. L.; Denardo, M. A.; Gayathri, C.; Gil, R. R.; Kanda, R.; Collins, T. J. *Environmental Science & Technology* **2016**, *Submitted*.

(21) Ghosh, A.; Ryabov, A. D.; Mayer, S. M.; Horner, D. C.; Prasuhn, D. E.; Sen Gupta, S.; Vuocolo, L.; Culver, C.; Hendrich, M. P.; Rickard, C. E. F.; Norman, R. E.; Horwitz, C. P.; Collins, T. J. *Journal of the American Chemical Society* **2003**, *125*, 12378.
(22) Fedor, L. R.; Bruice, T. C. *Journal of the American Chemical Society* **1965**, *87*, 4138.
(23) Ellis, W. C., Carnegie Mellon University.
(24) Hammond, G. S. *Journal of the American Chemical Society* **1955**, *77*, 334.
(25) Wang, Q.; Bennet, A. J.; Brown, R. S.; Santarsiero, B. D. *Canadian Journal of Chemistry* **1990**, *68*, 1732.
(26) Wang, Q. P.; Bennet, A. J.; Brown, R. S.; Santarsiero, B. D. *Journal of the American Chemical Society* **1991**, *113*, 5757.
(27) Blumberger, J.; Klein, M. L. *Chemical Physics Letters* **2006**, *422*, 210.
(28) Blumberger, J.; Ensing, B.; Klein, M. L. *Angewandte Chemie International Edition* **2006**, *45*, 2893.
(29) da Silva, P. L.; Guimarães, L.; Pliego, J. R. *The Journal of Physical Chemistry B* **2013**, *117*, 6487.
(30) Jencks, W. P.; Carriuolo, J. *Journal of the American Chemical Society* **1961**, *83*, 1743.
(31) Guthrie, J. P.; Cullimore, P. A. *Canadian Journal of Chemistry* **1980**, *58*, 1281.
(32) Sultana, N.; Fabian, M. F. *Beilstein J. Org. Chem.* **2013**, *9*, 594.
(33) Venkatasubban, K. S.; Davis, K. R.; Hogg, J. L. *Journal of the American Chemical Society* **1978**, *100*, 6125.
(34) Larson, R. A.; Weber, E. J. *Reaction Mechanisms in Environmental Organic Chemistry*; Lewis Publishers: Boca Raton, Florida, 1994.
(35) Mabey, W.; Mill, T. *Journal of Physical and Chemical Reference Data* **1978**, *7*, 383.
(36) Callahan, B. P.; Yuan, Y.; Wolfenden, R. *Journal of the American Chemical Society* **2005**, *127*, 10828.
(37) Gottlieb, H. E.; Kotlyar, V.; Nudelman, A. *The Journal of Organic Chemistry* **1997**, *62*, 7512.
(38) Horwitz, C. P.; Ghosh, A.; USPTO, Ed.; Carnegie Mellon University: United States, 2004.
(39) George, P. *Biochem J* **1953**, *54*, 267.